Finite Element Analysis of Thermoviscoplastic Deformations of an Impact-Loaded Prenotched Plate

Naim A. Jaber

Dissertation submitted to the Faculty of the
Virginia Polytechnic Institute and State University
in partial fulfillment of the requirements for the degree of

Doctor of Philosophy
in
Engineering Mechanics

Romesh C. Batra, Chair
Ali H. Nayfeh
Michael W. Hyer
Saad A. Ragab
Martin Klaus

December 13, 2000
Blacksburg, Virginia

Keywords: Finite Element Analysis, Failure Mode Transition, Impact Loading,
Thermoviscoplastic Deformations

Finite Element Analysis of Thermoviscoplastic Deformations of an Impact-Loaded Prenotched Plate

Naim A. Jaber

(ABSTRACT)

Four different thermoviscoplastic relations, namely, the Litonski-Batra, the Johnson-Cook, the Bodner-Partom and the power law are used to model the thermoviscoplastic response of a material. Each one of these relations accounts for strain hardening, strain-rate hardening and thermal softening of the material. The material parameters in these relations are found by solving an initial-boundary-value problem corresponding to simple shearing deformations so that the computed effective stress vs. the effective plastic strain curves match closely with the experimental data of Marchand and Duffy who tested thin-walled HY-100 steel tubes in torsion.

These four viscoplastic relations are used to analyze dynamic thermomechanical deformations of a prenotched plate impacted on the notched side by a cylindrical projectile made of the same material as the plate. The impact loading on the contact surface is simulated by prescribing the time history of the normal component of velocity and null tangential tractions. A plane strain state of deformation is assumed to prevail in the plate and its deformations are studied for different values of the impact speed. The in-house developed finite element code employs constant strain triangular elements, one point integration rule, and a lumped mass matrix. The Lagrangian description of motion is used to describe deformations of the plate. The coupled nonlinear partial differential equations are first reduced to coupled nonlinear ordinary differential equations (ODEs) by using the Galerkin approximation. The ODEs are

integrated by using the stiff solver, LSODE, which adaptively adjusts the time step size and computes the solution within the prescribed accuracy.

Results computed with the four constitutive relations are found to be qualitatively similar to each other and the general trends agree with the experimental observations in the sense that at low speed of impact, a brittle failure ensues at a point on the upper surface of the notch tip. However, at high impact speeds, a ductile failure in the form of a shear band initiates first from a point on the lower surface of the notch tip. The predicted speed at which the failure mode transitions from brittle to ductile is different for the four viscoplastic relations.

Results have been computed using the Bodner-Partom law to study the effects of the notch tip radius and the presence of a circular hole ahead of the notch-tip. For sharp elliptic notch tips, it is found that there is no failure transition speed and the ductile failure always preceeded the brittle failure for the range of the impact speeds studied. For the hole located on the axis of the circular notch tip, the brittle failure always preceeded the ductile failure and it initiated at a point on the lower surface of the circular hole.

Dedication

To my parents, for their dedication and inspiration

To my brothers and sisters, for their belief in me

To my wife, for her love and patience

Acknowledgments

I would like to express my gratitude and appreciation to my advisor Dr. Romesh Batra for his invaluable guidance and advice throughout my Ph.D. studies. I would like also to thank my committee members Dr. Ali Nayfeh, Dr. Michael Hyer, Dr. Saad Ragab, and Dr. Martin Klaus for their support and encouragement. It is an honor to have worked and learned from them. I am deeply indebted to Dr. Ali Nayfeh for his thoughtfulness, brilliance and unlimited support.

I would like to thank all the people and friends I have met as part of our group. In particular, I would like to thank Mr. Dean Rattazzi for being the nicest person to deal with, Dr. Axinte Ionita for his encouragement and Mr. Hsu-Kuang Ching for his friendship. I am also indebted to Mrs. Loretta Tickle for her help in administrative matters. Special thanks are due to my buddy Dr. Haider Arafat for the enjoyable time we shared together playing basketball and reviewing parts of this dissertation. Also I would like to thank Dr. Osama Ashour and Dr. Eihab Abdel-Rahman for their companionship and heated discussions. My deepest appreciation goes to my ex-roommates Dr. Ahmad Harb, Dr. Raid Awadallah and Mr. Zaker Alazzeh for the wonderful time we spent together. I would like to express my warmest thanks to Dr. Mohammad Hajj for his continued encouragement and support.

I would like to thank the Office of Naval Research for the partial support for this work through grant N00014-98-0300 to Virginia Polytechnic Institute and State University with Dr. Y. D. S. Rajapakse as the program manager. I also would like to thank Dr. Edmund Henneke and Dr. Don Morris for the financial support I had during my studies as a teaching

assistant from the Department of Engineering Science and Mechanics.

Most importantly, I would like to express my deep gratitude and sincere appreciation to my family; my parents for their dedication and inspiration that enabled me to reach this milestone in my life; my brothers and sisters, especially my brother Dr. Yaseen and my sister Fatima, for their continued support and belief in me. I am also deeply indebted to my wonderful wife for her love, patience and kindness. It is her continued support and encouragement which kept my belief that there will be an end someday for this work.

Contents

List of Figures

Chapter 1

Introduction

The study of dynamic material behavior under high impact velocity has received the attention of many researchers. This attention is driven by the wide range of civilian and military applications. In such cases, understanding the dynamic material behavior is necessary in order to characterize and model the failure and damage phenomena. These applications include high speed machining, ballistic impact, explosive welding, metal forming, and structural integrity in vehicle crash-worthiness. Fig. 1.1 shows a schematic representation of the contributing sciences and principal applications of dynamic processes in materials [74].

The dynamic material behavior is complex. The complexity arises from the many parameters that should be taken into consideration. These include modelling inertia forces, material rate behavior, and reflected stress waves. Earlier researchers heavily depended upon experimental results to understand the dynamic material behavior phenomenon and how it leads to failure. With the increase of computing power, modelling and simulation of such behavior is promising and more research is needed to fully simulate failure and damage in real materials.

It is observed that, with the increase of strain rate, the damage in ferrous metals, nonferrous metals, and polymers is accompanied by the formation of narrow bands of intense plastic deformations. Such bands are few micrometers in width and are known as *adiabatic shear*

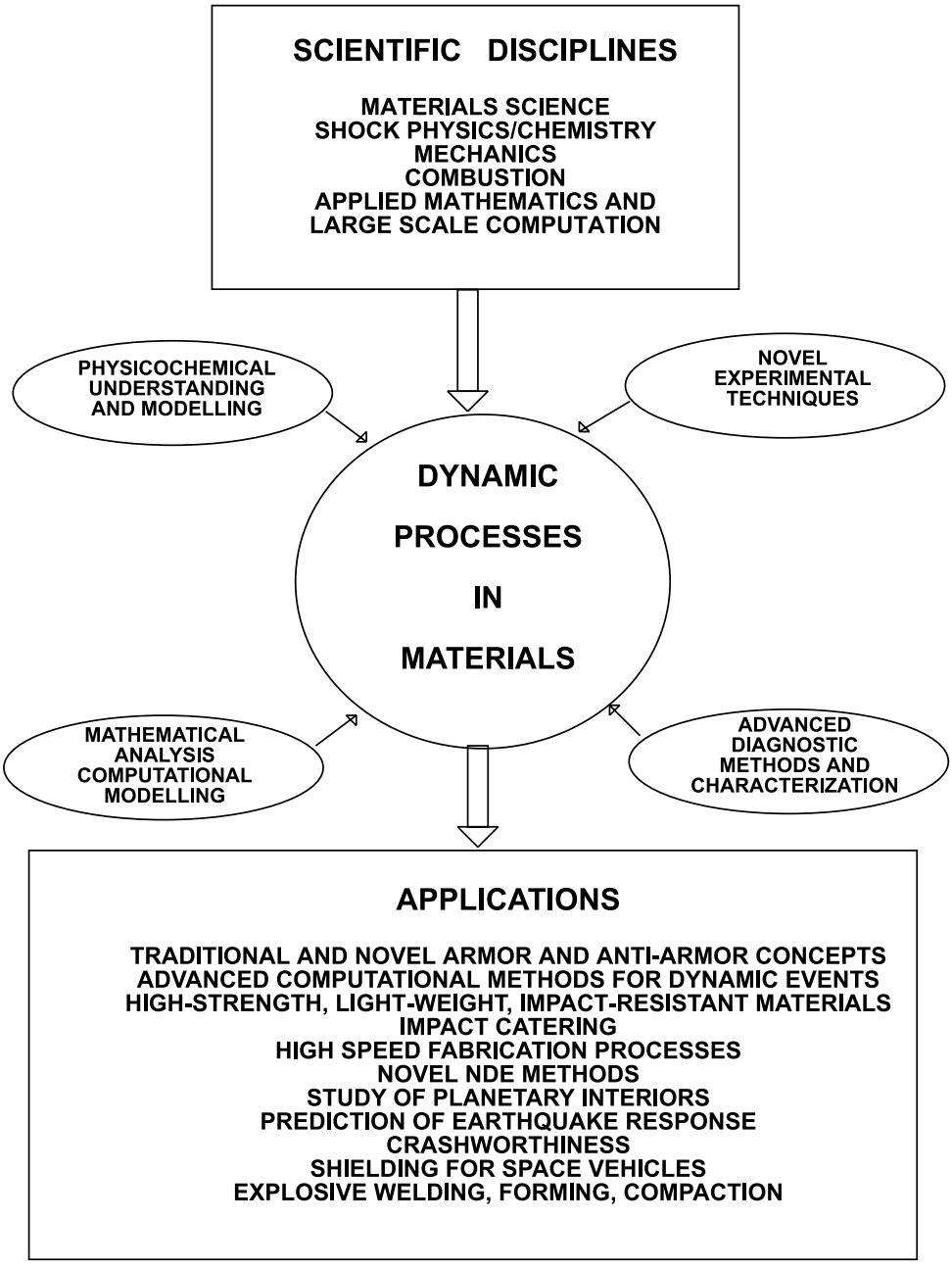

Figure 1.1: Contributing sciences and applications of dynamic processes.

bands. It is generally noticed that shear bands occur during dynamic shearing or compression. These bands are a precursor to failure on the microscopic level and hence can lead to premature failure in structures. There are numerous mechanisms of failure, but most fractures are classified as ductile or brittle fracture. Brittle fracture requires little or no plasticity to initiate and propagate, while ductile fracture requires an extensive plasticity to initiate and develop. The failure associated with shear bands is usually a ductile fracture. In the numerical modelling of shear bands, difficulty arises from the modelling of the failure mechanism in a manner that agrees with experimental findings.

1.1 Literature Review

We briefly review the relevant literature in the following areas:

1. Metallurgical observations.
2. Constitutive modeling.
3. Instability analysis.
4. Numerical simulation.
5. Recent work.

1.1.1 Metallurgical Observations

Johnson [53] reported that the first pioneering works on shear bands were of Tresca in 1878 and Massey in 1921. Tresca observed hot lines in the shape of an X in a bar of metal after subjecting it to a blow with a steam hammer. He estimated the amount of plastic work converted to heat to be 73.1% in iron and 94.2% in copper. Massey independently reported that, during hot forging, heat lines were visible in the test piece. Fifty years after Tresca,

Taylor and Quinney [98] estimated that more than 90% of the plastic work converted to heat under high strain rates. Zener and Hollomon [111] were the first to use the terminology adiabatic shear bands. They observed a shear band during punching of a hole in a low carbon steel plate. They proposed that, at the onset of the shear band, the material becomes unstable when the thermal softening becomes greater than the strain hardening.

Metallurgical observations of shear bands revealed that there are two types: deformed and transformed shear bands. The deformed shear bands are bands of high strain without phase transformation as shown in Fig. 1.2, while the transformed shear bands are bands in which a phase change in the crystal of the material occurs as shown in Fig. 1.3. The transformed shear bands in steels go through a martensitic transformation. A martensitic transformation in steels involves sudden reorientation of carbon (C) and iron (Fe) atoms from the face center cubic (fcc) crystal structure (austenite) to a body centered tetragonal (bct) crystal structure (martensite). The region that has the martensite structure is highly brittle and susceptible to cracking [86]. The martensite after itching looks like a white band. In their experiment, Zener and Hollomon [111] reported that a white band of metal adjoining the punched surface in the plate is of martensite.

Backman and Finnegan [4] experimentally investigated ballistic impacts and explosive loadings of hollow cylinders made of SAE 4130 steel, SAE 1020 steel, and 2024 aluminum alloy. They reported that, for impact tests on four microstructures of SAE 4130 steel, either a deformed or a transformed band was present in a specific microstructure. For the lamellar pearlite and ferrite, a deformed band existed, while, for the tempered martensite and lower bainite, a transformed band existed. In the impact testing of aluminum, the pattern of cracks followed the pattern of the shear bands in the specimen. The microscopic examination of fragments of SAE 1020 steel showed that shear bands initiated at flaws, pits, scratches, and inhomogeneities in the material. The shear band width was found to be 3-10 μm, depending on the material and loading conditions. Shocky et al. [87] explained the effect of different microstructural features that play a significant role in the dynamic fracture process. These features include flaws, voids, inclusions, grain boundaries, subgrain structures, and impu-

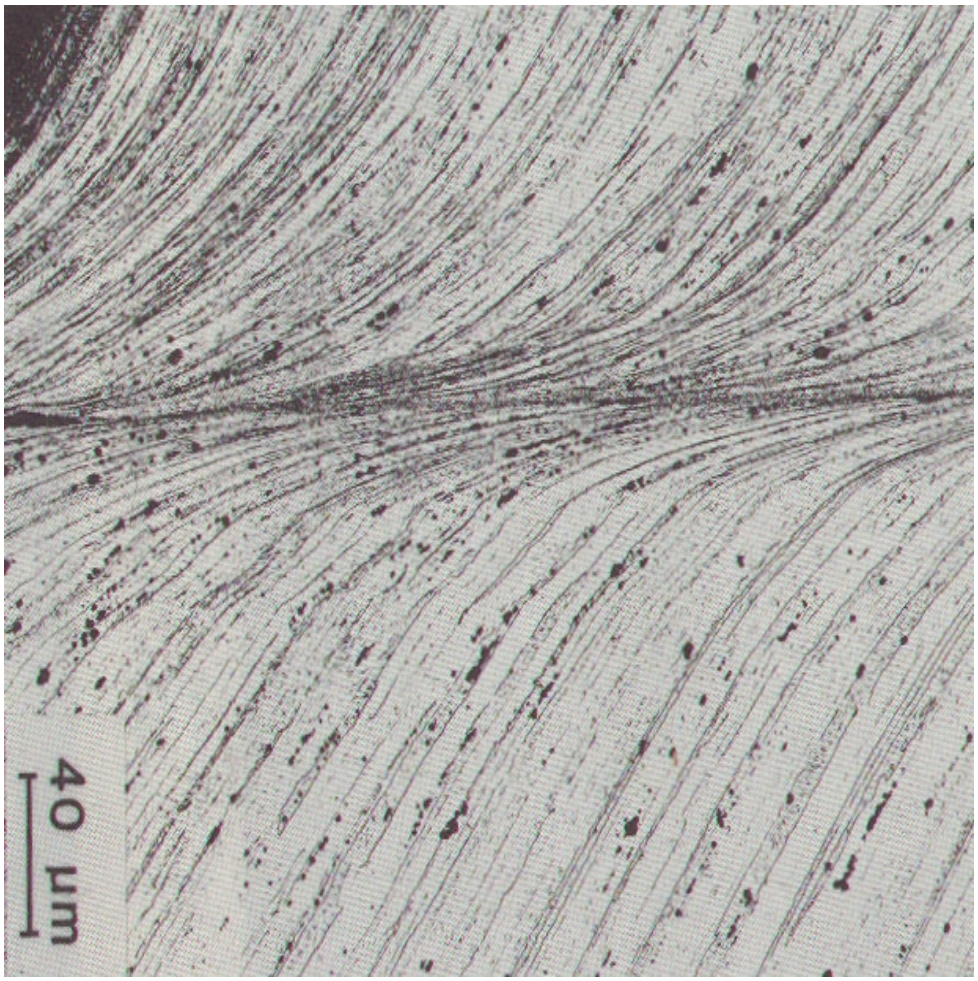

Figure 1.2: Deformed shear band [64].

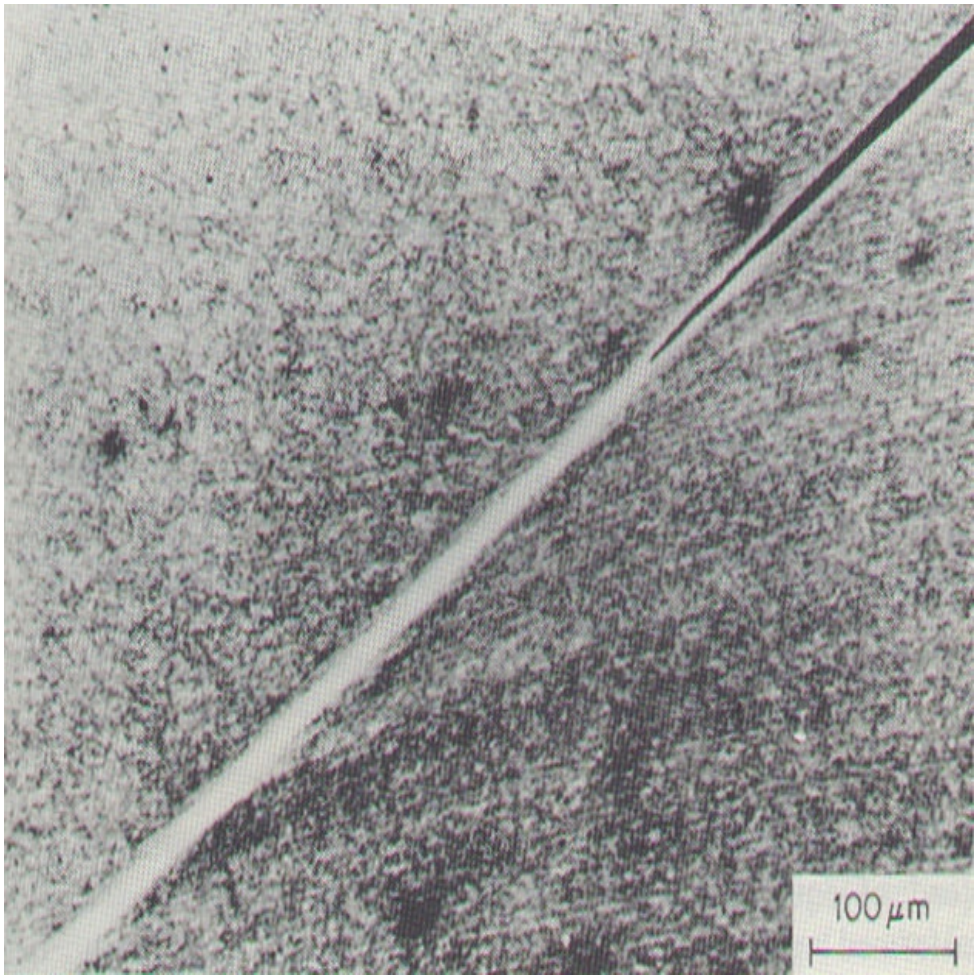

Figure 1.3: Transformed shear band [38].

rities. They reported that the impact velocity necessary to produce the incipient cracking in Armco steel was found to be nearly 50% higher than that required to produce the same amount of fracture damage in a similar 99.99% pure iron specimen.

Winter [99] studied the adiabatic shear bands in titanium and polymethylmethacrylate (PMMA). Flat ended steel cylindrical rods (diam. = 4 *mm*, L = 20 *mm*) were accelerated using a gas gun to speeds up to 330 *m/s*. The targets were aluminium rods (Diam. = 16 *mm*, L = 25 *mm*) and PMMA blocks (L = 40 *mm*, W = 60 *mm*, H = 2.54 *mm*). For the titanium, a shear band in the shape of a V was present. Micro scans showed the presence of spherical cavities in the band. Shear bands were also observed in the PMMA with cavities and small cracks. Micro scans were obtained by using a transmission electron microscope (TEM). TEM is similar to the conventional microscope in design but it uses an electron source instead of a light source and uses solenoid coils to produce a magnetic lens in place of the glass lens in the optical microscope. Practical magnifications of hundred thousands can be obtained by using the TEM compared to two thousands using the optical microscope. Winter [100] experimented with a 1 *mm* wall hollow brass cylinder partially filled with rubber. A small gas gun projected a short nylon rod into the cylinder with speeds up to 630 *m/s*. Observation of the fracture process suggested that shear rather than tensile forces in the cylinder control the failure mechanism. This is evident as all the longitudinal cracks propagated at 45^o.

Rogers [85] used cylindrical steel projectiles (diam. = 0.6 *in* , L = 4 *in*) to impact plates whose thickness ranges from 1/4 to 5/16 *in*. The plates were made of AISI 1040 steel, AISI 1018 steel, and AISI 1075 steel. Mircohardness profiles transverse to the shear bands show that the central zone of the shear band has the highest hardness. Micro scans revealed that the deformed band preceded the transformed band. Woodward's [105] ballistic impacting of 9.5 *mm* thick 7039-T6 aluminium and 6 *mm* thick titanium plates clearly showed that both materials fail by plugging by shear bands. Bourne [30] used explosively hollow cylinders (diam = 40, L = 70 *mm*, thickness = 1.8 *mm*) to obtain optical and scanning electron microscopies of iron, copper, aluminium, and steel. His experiments revealed that, under

high strain loading, three phenomena were observed in the formed fragments. They are twinning, recrystallization, and shear bands. Twinning happens at normal rates of strain by a dislocation movement mechanism and occurs at low temperatures. Recrystallization occurs if the deformation is sufficiently large and rapid to heat the fragments above their recrystallization temperature. Recrystallization leads to grain sizes smaller than those in the original material. Shear bands occur when the heat generated by the plastic deformations does not have sufficient time to dissipate.

Affourad et al. [1] studied four martensitic steel cylinder specimens (diam. = 6 *mm*, L = 6 *mm*). The four steels are 20CND8, Z50CDV, 35 NCDV16, and 4340. The cylinders were tested using the standard compression split Hopkinson bar. They found that fracture always occurs on shear surfaces inclined at about 45^o. The microscopic observations showed that fracture is associated with the development of shear bands which lead to the formation of cracks. Timothy and Hutchinson's [91] ballistic experiments on titanium Ti-6%Al-4%V showed that the microstructure of the shear bands etched white in comparison to the surrounding material. This is an indication of transformed bands in that region. They performed microhardness tests and showed that, as the width of the shear bands decreases, their hardness increases. Also, round shape cavities were sometimes found within the shear bands. Grebe et al. [43] experimented on 12.5 *mm* thick plates. They considered commercial purity titanium and Ti-6%Al4%V alloy and used stepped front portion steel cylinder projectiles. Fractography showed the presence of shear bands that have voids within them. The cavities were spherical until their diameter reached the thickness of the shear band. Meyers and Manwarings [73] used the split Hopkinson pressure bar to test a hat specimen made of a low alloy steel and titanium alloy. The fractography indicated the presence of shear bands in the sheared region of the specimen.

The summary by Shockey et al. [88] of a series of experiments showed that, under dynamic tensile loading, a material fails by nucleation, growth, and coalescence of voids. Contrary to what was believed then, the metallographic observations of contained exploding cylinders showed that microstructural features are not important to shear bands. They reported that,

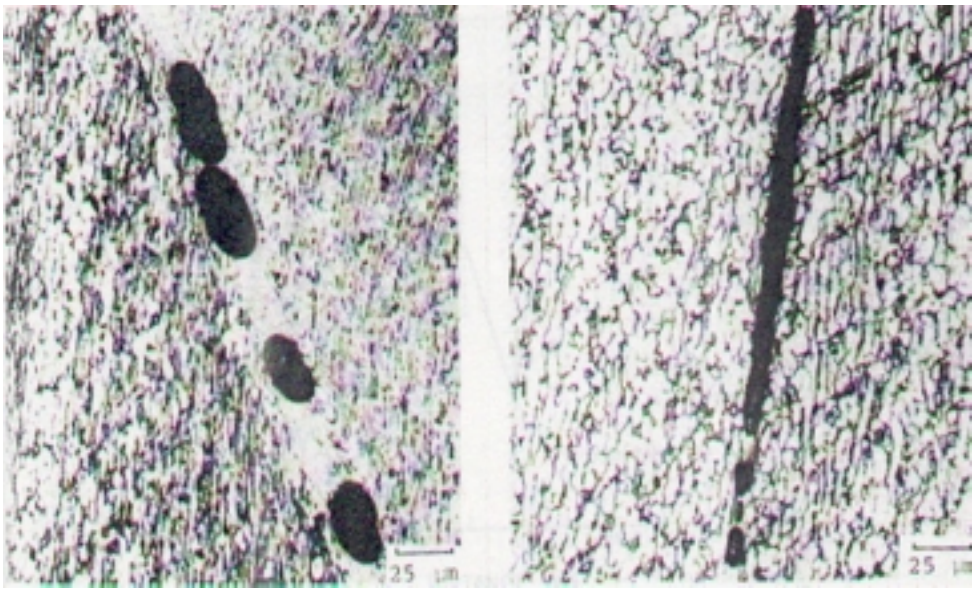

Figure 1.4: Shear band with voids [45].

in 4340 steels and for different melt practices (airmelt, vacuum induction melt), shear band initiation is apparently unaffected by microstructural features. This is because the shear band paths did not seem to deviate from the surfaces of maximum shear strain even when inclusions existed close by. Giovanola [44, 45] experimented on hollow 4340 steel cylinders and used the Hopkinson torsion bar. He reported that three features were clear in the shear band fracture surfaces. These are smeared material, pattern of microvoid, and smeared knobby material as shown in Fig. 1.4.

1.1.2 Constitutive Modelling

Under high strain loadings, many factors influence the macroscopic response of the material. These factors include strain, strain rate, temperature, and microstructure of the material. In general, the effect of increasing the strain rate on the stress-strain curve is to move the curve to a higher level. Meanwhile, increasing the testing temperature has the opposite effect, it tends to move the stress-strain curve to a lower level. This is evident by the work of many researchers.

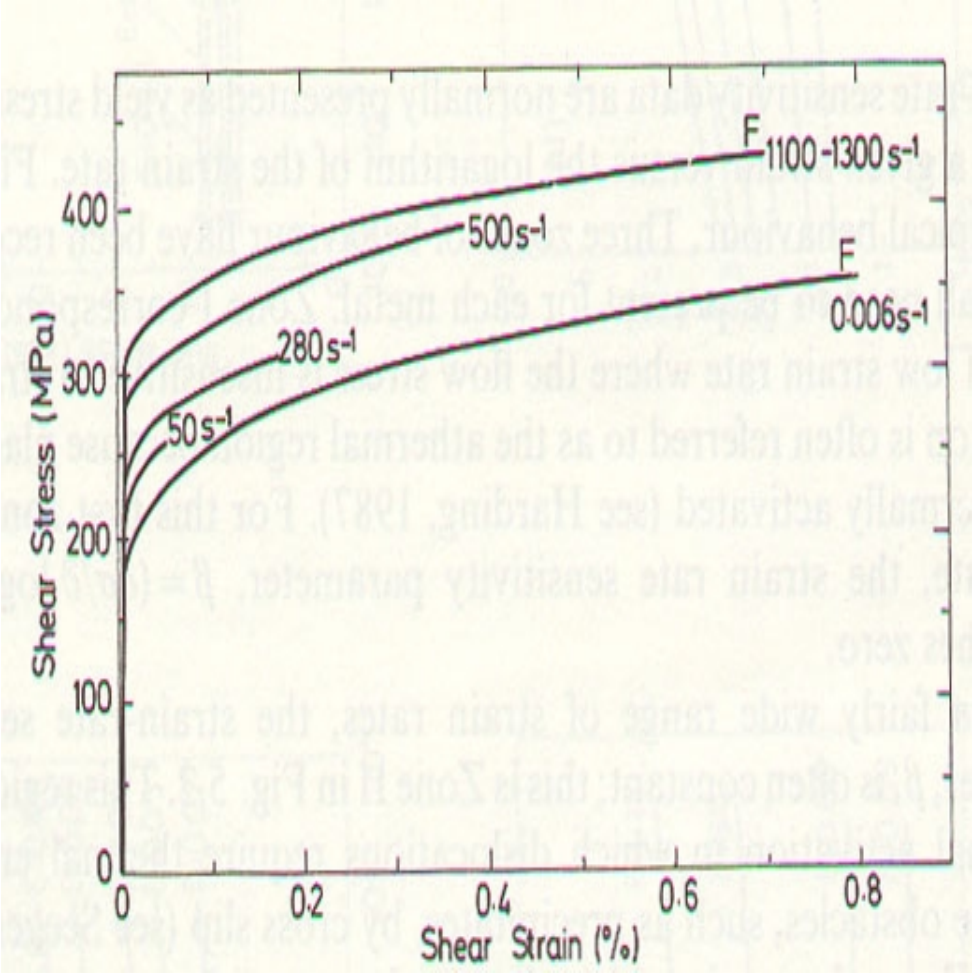

Figure 1.5: Effect of strain rate on the stress strain curve [41].

The experimental work of Tsao and Campbell [92] and Eleiche and Campbell [41] on commercial purity aluminium and titanium clearly showed that the effect of strain rate is to raise the stress-strain curve to a higher level as shown in Fig. 1.5. Hockett [51] experimentally observed that the effect of temperature increase is to move the stress-strain curve to a lower level as shown in Fig. 1.6. In Harding's [49] experimental results on quenched tempered alloy steel and annealed Ti6%Al4%V alloy, it is noticed that, with continued deformation, a drop in the stress-strain curve occurs.

From the aforementioned experimental observations, the constitutive equation should model the above different factors in order to be admissible to all possible combinations of strains,

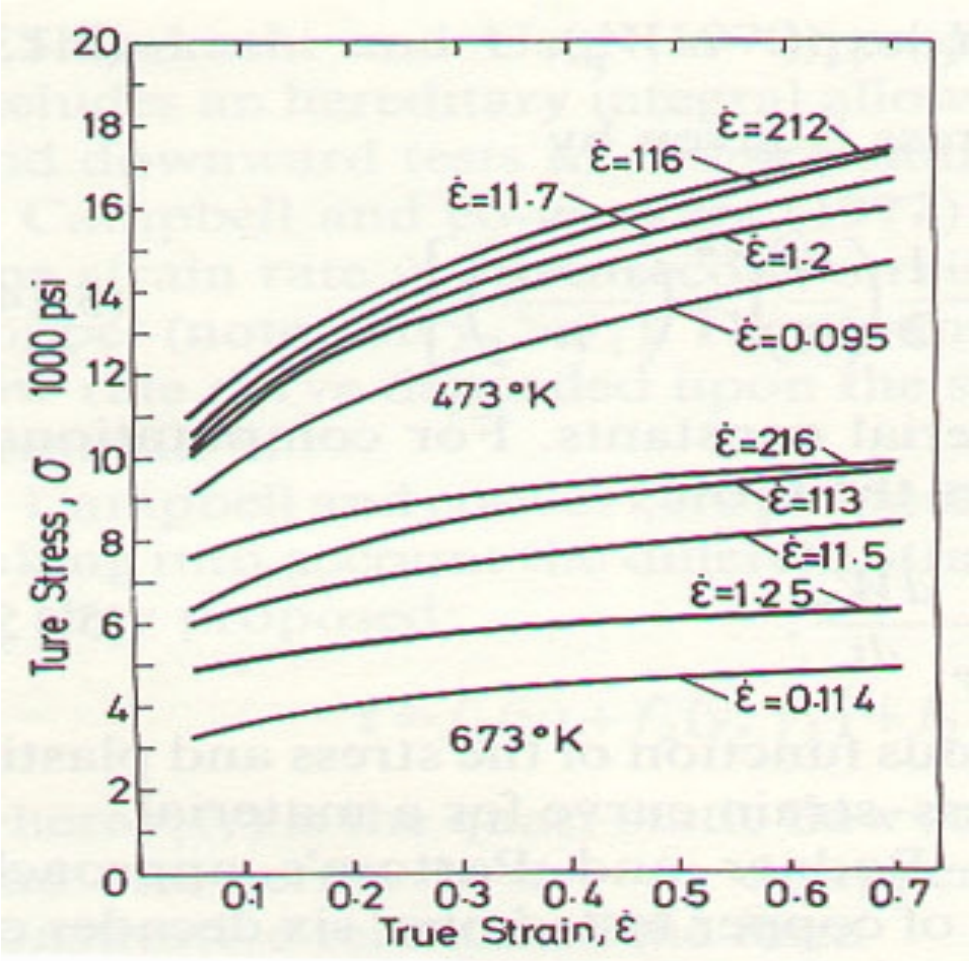

Figure 1.6: Effect of temperature on the stress strain curve [51].

strain rates, and temperatures. The constitutive model should be able to capture all of the above features. Many constitutive models have been proposed, those constitutive models take into consideration the history, strain rate and temperature effects. Moreover some of the constitutive models consider other effects in their modeling. The Zerilli-Armstrong model [107] considers the dislocation mechanism and distinguishes between bcc and fcc materials. Chaboche's [32] model considers the cyclic loading and time recovery effects. Other models include Perzyna [81], Litonski-Batra [8], power law [58], Bodner-Partom [29] and Johnson-Cook [52].

Batra and Kim [19] used the last four thermoviscoplastic relations to study the initiation and development of shear bands in a viscoplastic block made of a HY-100 steel and deformed in simple shear. They simulated the dynamic torsional tests of Marchand and Duffy [69] on thin-walled HY-100 steel tubes as a simple shearing problem, determined the values of material parameters by solving an initial-boundary-value problem and adjusted the values of material parameters till the computed shear stress-shear strain curve closely matched with the experimental curve of Marchand and Duffy. Herein, we used material parameters obtained by Batra and Kim [19] for the those models, and list below these four models.

Litonski-Batra Law

This constitutive equation was proposed by Batra [8] and is a generalization of a model suggested previously by Litonski [68]. It can be written as

$$\sigma_e = \sigma_0 \left(1 + b\dot{\varepsilon}^p\right)^m \left(1 + \frac{\varepsilon^p}{\varepsilon_y}\right)^n (1 - \nu_s\theta) \tag{1.1}$$

where σ_e is the effective stress; σ_0 is the yield stress of the material in a quasistatic test; b and m characterize the strain rate hardening; ε_y and n characterize the strain hardening, θ is the temperature, ε^p is the effective plastic strain, $\dot{\varepsilon}^p$ is the effective plastic strain rate and

ν_s characterizes the thermal softening of the material.

Power Law

Klopp et al. [58] and Hartley et al. [48] described the dynamic stress-strain curve for steels in simple shearing as a power law. Many researchers, e.g. Needleman and Tvergaard [77], have used the following 3-dimensional model by replacing the shear stress by the effective stress and the shear strain by the effective plastic strain

$$\sigma_e = \sigma_0 \left(\frac{\dot{\varepsilon}^p}{\dot{\varepsilon}_o}\right)^m \left(\frac{\varepsilon^p}{\varepsilon_y}\right)^n \left(\frac{\theta}{\theta_0}\right)^\tau \tag{1.2}$$

where $\dot{\varepsilon}_o$ and m characterize the strain rate hardening; ε_y and n characterize the strain hardening, and τ characterizes the thermal softening of the material.

Bodner-Partom Law

This constitutive relation was proposed by Bodner and Partom [29]. It can be written as

$$\dot{\varepsilon}^p = D_0 \exp\left[-\frac{1}{2}\left(\frac{K^2}{3\sigma_e^2}\right)^n\right] \tag{1.3}$$

where σ_e is the effective stress, D_0 is the limiting value of the effective plastic strain rate and, K and n are given by:

$$K = K_1 - (K_1 - K_0)\exp\left(-mW_p\right), \quad n = \frac{a}{\theta} + b. \tag{1.4}$$

In equation (1.4) K_1, K_0, m, a, and b characterize the material and W_p denotes the plastic work done.

Johnson- Cook Law

This was proposed by Johnson and Cook [52]. It can be written as

$$\sigma_e = [A + B\ (\varepsilon^p)^n] \left[1 + c \ln \left(\frac{\dot{\varepsilon}^p}{\dot{\varepsilon}_0}\right)\right] (1 - T^m) \tag{1.5}$$

where c and $\dot{\varepsilon}_0$ characterize the strain rate hardening; A, B, and n characterize the strain hardening; T and m characterize the thermal softening of the material, and T is given by

$$T = \frac{\theta - \theta_0}{\theta_m - \theta_0} \tag{1.6}$$

where θ_0 is the ambient temperature and θ_m is the melting temperature.

1.1.3 Material Instability

Many experimental observations have shown that material instability corresponds to a drop in the stress-strain curve. As mentioned by Bai and Dodd [5], this is in agreement with Drucker's hypothesis [39] concerning stable and unstable deformations in plasticity theory. As shown in Fig. 1.7c, the unstable deformation corresponds to an increase in the plastic strain while the stress decreases beyond a stress maximum at the same moment. Recht [83] postulated that catastrophic shear will occur at a plastically deforming location when the slope of the true-stress true-strain function becomes zero. Recht also ranked seven materials in order of their susceptibility to catastrophic shear as a function of the strain rate and compared them to titanium RC-70, the material most susceptible to shear banding. In his ranking, the titanium is 1400 times susceptible to catastrophic shear than mild steel SAE

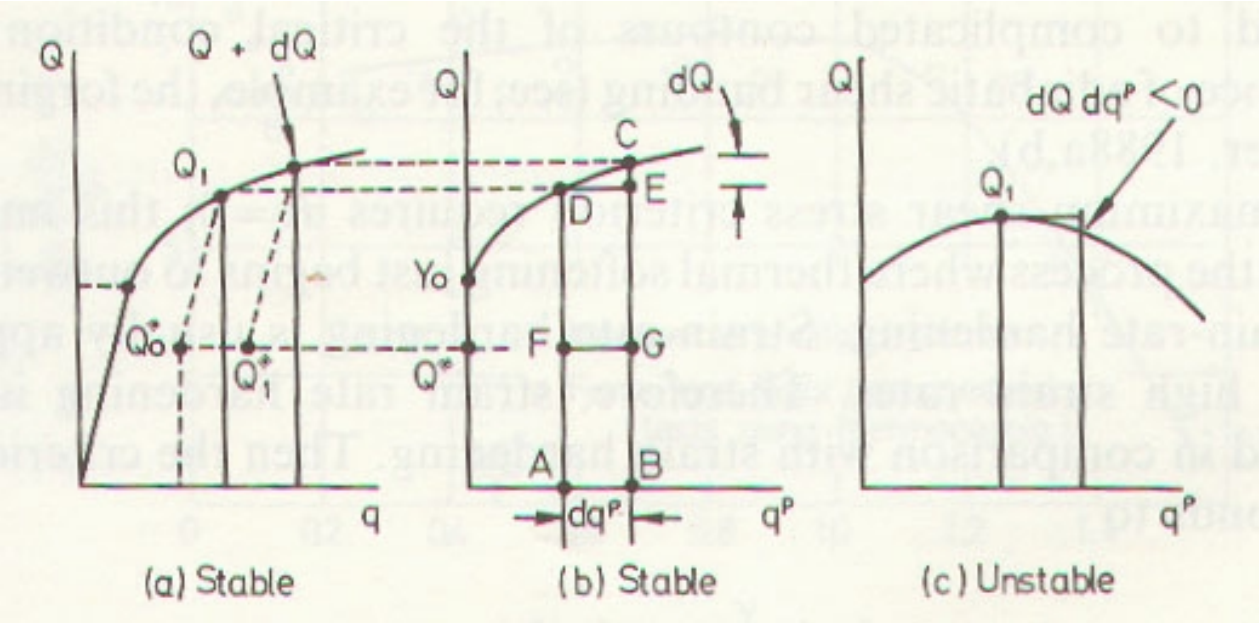

Figure 1.7: Drucker's hypothesis concerning stable and unstable deformation [5].

1020.

The experimental work of Culver [37] on thermal instability of annealed mild steel, 6061-T6 aluminium and commercially pure titanium deformed at strain rates between 74 to 320 s^{-1} showed that strain localization occurs at a strain near the static fracture strain. Culver also conducted theoretical investigations based on Recht's hypothesis and calculated the instability strain in close agreement with his experimental results. Staker [89] experimentally and theoretically investigated explosively expanded hollow 4340 steel cylinders and obtained analytical strain predictions that are in agreement with his experimental results. Lindholm [67] also used a procedure similar to the procedures of Culver [37] and Staker [89]. He obtained good agreement between experimental critical strain results and theoretical critical strain predictions. The formulation used in these three analyses was based on taking the derivative of the shear stress with respect to the shear strain and equating it to zero. Lindholm used the Johnson-Cook model to calculate the critical strain. In mathematical form, this is expressed by

$$\frac{d\tau}{d\gamma} = \left(\frac{\partial\tau}{\partial\gamma}\right)_T + \left(\frac{\partial\tau}{\partial T}\right)\frac{\partial T}{\partial\gamma} + \left(\frac{\partial\tau}{\partial\dot{\gamma}}\right)\frac{\partial\dot{\gamma}/\partial t}{\partial\gamma/\partial t} = 0 \tag{1.7}$$

where τ is the shear stress; γ is the shear strain; $\dot{\gamma}$ is the shear strain rate; T is the temperature and t is the time.

The experiments of Marchand and Duffy [69] on HY-100 steel tubes using the torsional split Hopkinson bar revealed that three stages of deformation can be identified as shown in Fig. 1.8. The first stage is a homogeneous deformation for a nominal strain less than 35%. The second stage is an inhomogeneous deformation for a nominal strain of 35% to 50%. The third stage corresponds to a nominal strain greater than 50% and is characterized by a sudden drop in the load-carrying capacity. They used infrared antimonide cells to measure the temperature and an optical system to monitor the deformation with time. They reported a temperature rise of 410-590 ^{0}C, a shear band width of 20 μm, and a shear band speed of 510 m/s. The work of Marchand and Duffy [69] was the first comprehensive experimental investigation to monitor the stress, strain, and temperature during the deformation process. Duffy and Chi [40] extended the work of Marchand and Duffy [69] by measuring the strain and temperature during the testing of four different steel materials using thin-walled tubular specimens. The steels tested were AISI 1080 cold-rolled steel, low alloy HY-100 steel, and two AISI 4340 VAR steels with tempered hardnesses H_{RC} 44 and 55. A geometric defect was calculated based on the measurements of the departure from the ideal thickness dimension. Results showed that the critical plastic strain at which localization is initiated depends upon the magnitude of the geometric defect in the specimen, in accordance with theoretical results obtained by Molinari and Clifton [75].

By using a setup similar to that of Marchand and Duffy [69], Liao and Marchand [66] investigated the process of initiation and formation of shear bands in a Ti-6Al-4V alloy. They measured the geometric defect in the wall thickness. The results of the critical localization

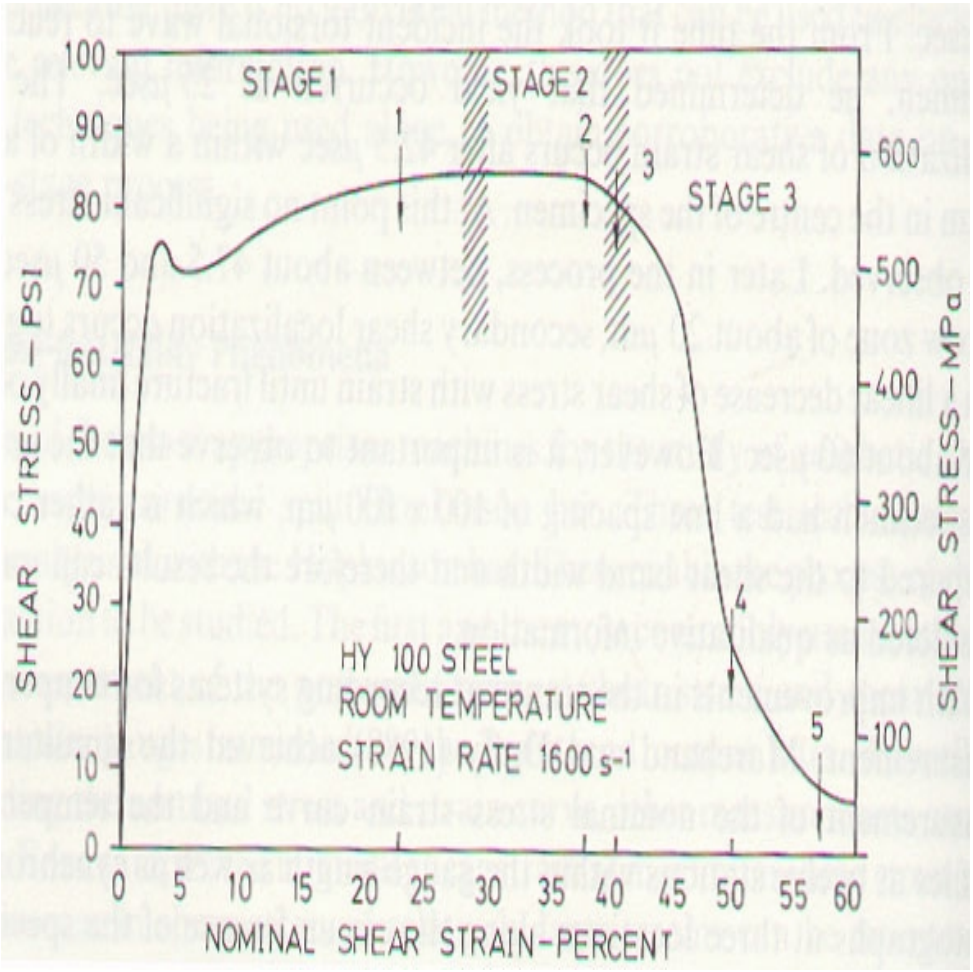

Figure 1.8: Shear stress vs. shear strain from Marchand and Duffy's experiment [69].

strain versus the geometric defect parameter showed a large scatter in the data, which prevented any definite conclusion on the effect of the geometric defect on critical strain, in contrast to results of Duffy and Chi [40]. The dynamic stress-strain curve showed a linear elastic rise, followed by a plateau of constant stress with further straining, and then a sudden drop in load preceding failure. In all of the tested specimens, a crack appeared within the shear bands. The width of the shear bands in Ti-6Al-4V alloy ranged from 12 to 55 μm and the temperature rise 440 to 550 ^{0}C.

The above experimental observations indicate that the initiation of shear bands corresponds to a sudden drop in the stress. Other theoretical formulations attempted to explain the shear band instability. Bai [6] used a perturbation analysis and concluded that the thermal softening accelerates the growth of inhomogeneities while the strain hardening and strain-rate hardening retarded the growth. Merzner [72] examined the localization behavior due to a narrow initial geometrical imperfection. He concluded that the band width is independent of the initial size. Chen and Batra [33] used the Johnson-Cook model to study a strain instability criterion and ranked eight materials in order of their susceptibility to shear banding.

1.1.4 Numerical Simulation

Dynamic modelling studies involve many problems that can not be solved analytically. Some of the inherent modelling characteristics of the dynamic events include non-linearity and coupling effects in the constitutive equations. Further problems arise from the complicated geometrical configuration of disturbances and imperfections. Therefore, analytical analyses are limited to a few problems and, hence, many researchers utilize numerical simulations as a powerful tool to tackle more complex problems and verify the existing experimental results and theoretical predictions.

The numerical simulations carried out utilize finite difference or finite element formulations. In the early stages of dynamic modelling, one-dimensional simulations were used. Recently,

two-dimensional and three-dimensional simulations are more frequently used, sometimes utilizing adaptive mesh refinement techniques. Generally, the simulations can be classified into the following categories, depending upon the main point of study:

1. Effect of the disturbance or imperfection.
2. Effect of different constitutive laws.
3. Effect of mesh refinement.
4. Effect of three-dimensional simulations.
5. Failure criteria and post-failure simulation.

Effect of the disturbance or imperfection

Litonski [68] conducted finite difference simulations on a geometrically inhomogeneous tube and showed that, when the torque reaches a maximum, the strain rate increases in the weak part and vanishes in the strong part. Wright and Batra [101, 102, 103] described the results of computations that simulate a single shear band from a local temperature inhomogeneity in simple and dipolar materials. Their computations show increasing inhomogeneity at an accelerating rate in the strain, strain rate, and temperature fields at a point very near to the center of the band. Batra [7] investigated the problem of simple shearing of a finite slab. He assumed an initial perturbation in the temperature and found that the existence of a peak in the shear stress acts as the necessary condition for localization. Furthermore, a sensitivity analysis of increasing the strain rate and strain sensitivity parameters resulted in delaying the deformation localization. Needleman [76] studied the plane strain compression of a rectangular block and modelled the initial inhomogeneity as a local reduction in the flow strength. His findings indicate that the inhomogeneity plays the critical role in triggering the onset of the shear localization. Needleman and Tveergard's [78, 79] numerical simulations to analyze the dynamic crack growth were based on the failure predictions of a porous plastic

material model that represents ductile fracture by nucleation and subsequent growth and coalescence of voids.

Batra and Jin [20] studied the initiation and growth of shear bands in a porous thermally softening viscoplastic block under plane strain tension. They modeled the porosity by the Gurson model [46] in order to account for the microscopic observations of the failure process in several metals. A temperature perturbation was introduced at the center of the block. They found that the shear bands form at a lower value of nominal strain when the initial porosity is increased.

Batra and Peng [24] studied the plane strain deformation of depleted uranium and tungsten at a nominal strain rate of 5000 s^{-1}. They modeled the defects as a weaker material; the flow stress for the weaker material in a quasistatic simple compression test is taken to be 5% lower than the original material. Their results indicate that the compressive force required to deform the body drops sharply for the uranium block when the shear band is initiated. However, for the tungsten block, the compressive force drops gradually.

Effect of different constitutive laws

Batra and Kim [14] modeled the torsional tests of Marchand and Duffy [69] by analyzing the deformation of a viscoplastic block undergoing simple shearing deformation. They modeled the geometric imperfection in the specimen by a temperature perturbation and used four different constitutive models. These models were Litonski-Batra, Power law, Bodner-Patrom, and Johnson-Cook. They obtained the different constitutive model constants so that the stress-strain curves obtained by these laws approximately match the experimental stress-strain curve in the torsional tests of Marchand and Duffy [69]. The objective was to compare predictions of those constitutive models with the experimental findings. The predictions from the dipolar Litonski-Batra and Bodner-Partom laws were in good agreement with the experimental findings, predicting the gradual drop in the stress-strain curve

and the gradual increase of the temperature. Batra and Adam [10] investigated the axisymmetric deformations of a thick viscoplastic target impacted by a fast-moving long rigid cylindrical penetrator. They used two constitutive relations, Litonski-Batra flow rule and Bodner-Partom flow rule. The results for both flow rules were in agreement qualitatively, but not quantitatively. Batra and Jayachandran [21] studied the axisymmetric deformations of a thick target being penetrated by a rigid cylinder. They used three different constitutive relations, namely, the Litonski-Batra flow rule, the Bodner-Partom flow rule, and the Brown-Kim-Anand flow rule. They found that the three relations gave nearly the same value of macroscopic measures of deformations such as the temperature and the plastic strain.

Effect of mesh refinement

Batra and Ko [17, 18] studied the plane strain deformations of a block in compression and the axisymmetric compression of a cylinder by using an adaptively refined mesh. Their numerical simulations showed that the solution obtained with an adaptively refined mesh has less error. Batra and Hwang [13] studied the plane strain deformation of a block in compression. They used a fixed number of quadrilateral elements and refined the mesh such that the area of the element is inversely proportional to the value of the deformation measure at the centroid. Batra and Jin [20] in their study, mentioned earlier, utilized the technique developed by Batra and Ko [17] to refine the mesh.

Effect of three-dimensional simulations

Batra and Zhang [27] and Batra and Rattazzi [25] studied the effect of three-dimensional simulations. Batra and Zhang [27] simulated the study of Marchand and Duffy [69] numerically. They modeled the material defect by assuming that a small region near the center of the tubular surface is made from a material weaker than that of the rest of the tube. They found that the shear band initiates at the site of the weak region. At a nominal strain rate of $1000/s$, they estimated the shear band speed varies from 40 to $260m/s$. Batra and Rattazzi

[25] studied the initiation of shear bands in a thick-walled 4340 steel tube with a V-notch in the middle. Torsional and axial pressure loading were considered. Under torsional loading, a shear band initiated in the element below a notch tip and propagated radially inward.

Failure criteria and post-failure simulation

The study of failure criteria and post-failure simulation can be classified into two categories. The first category concerns the criterion on the initiation of failure and the second with modelling the failure process. In the first category a number of different descriptions are used by many researchers. Those are summarized by Zukas [112] and can be classified into three descriptions as follow:

1. Instantaneous criteria: Those are based on the attainment of critical value of pressure, stress, strain, plastic work, internal energy or some combination of these.
2. Cumulative criteria: Those are based on the history of stress or strain.
3. Micromechanical criteria: Those are based on the nucleation and growth of voids, cracks and shear bands.

The techniques used to model failure can be classified as:

1. Moving mesh method: a mesh that moves with the crack tip is used. Examples utilizing this method include the works of Atluri and Nishioka [3], Koh et al. [61] and Thesken and Gudmundson [90].
2. Node split technique: the location of the crack tip is moved from one node to another along the crack path. Crack simulation using the node split technique is found in the works of Aoki et al. [2], Yagawa et al. [106] and Kobayashi et al. [60].

3. Element extinction technique or the element vanish technique: this is utilized by neglecting the failed element's contribution to the finite element solution. Examples of the element extinction technique are found in the works of Tvergaard [97] and Beissel et al. [28].

1.1.5 Recent Work

Kalthoff [54] and Kalthoff and Winkler [55] experimented with a steel plate having two parallel edge notches. They impacted the plate with a projectile of diameter equal to the distance between the two edge cracks and found that two types of behavior are possible, depending upon the impact velocity and notch radius. For a specific notch radius, if the impact velocity is below a limiting value, the crack propagates at an angle about 70^o degrees with respect to the notch axis. The metallographic micrographs of the fracture surface show a typical indications of roughness and shear lips at the edge of the surface. This is an indication that this fracture is controlled by a tensile fracture process. On the other hand, if the impact velocity is higher than the limiting value, the damage propagates at a small angle with respect to the notch axis and in the direction opposite to the crack observed when the impact velocity is below the limiting value. The metallographic micrographs of the fracture surface show a heavily sheared localized band and large smeared surfaces that have mirror-like appearances and without shear lips. This is an indication of a shear band failure which was observed to extend over a limited length and coming to arrest in most cases. A schematic outline of Kalthoff's work is presented in Fig. 1.9.

Mason et al. [70] used the optical interferometric method of coherent gradient sensing (CGS) to study the deformation field for C-300 steel around the crack tip. They used a single notch specimen and modelled the shear band formation with mode II Dugdale strip yield model. For an impact velocity of 40 m/s, a shear band initiated from the crack tip parallel to the notch axis. Nearly 40 μs after the impact the shear band arrested and a different mode of failure initiated at a large positive angle to the shear band direction. They found that

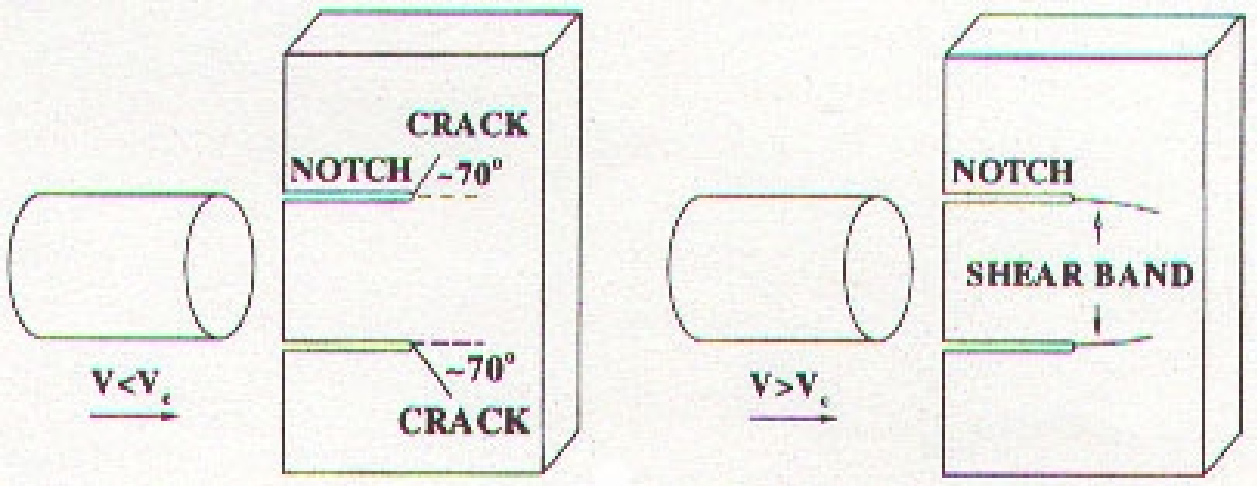

Figure 1.9: Schematic sketch of Kalthoff's experiments [108].

shear band initiated when the stress intensity factor K_{II}^{d} =140 $MPa\sqrt{m}$. Furthermore, they reported a shear band width of 200-400μm propagating at a speed of 320 m/s.

Zhou et al. [108] also experimented with a single notch specimen of C-300 steel and Ti-6Al-4V. They used high-speed photography to study the initiation time and speed of shear band, and their dependence on the impact velocity. Using an array of detectors that are parallel and perpendicular to the shear band propagation direction, they measured the temperature inside the shear band. The C-300 steel results showed that, for an impact velocity less than 20 m/s, no failure was observed. However, for intermediate impact velocities between 20 to 29.6 m/s, a shear band initiated from the notch tip and arrested inside the specimen. In addition a tensile crack is observed to initiate from the arrested shear band. This contradicts Kalthoff's experiments described earlier. For higher impact velocities, the shear band propagated through the whole C-300 steel specimen. The Ti-6AL-4V results showed that there is no transition of failure modes and only shear failure occurred. Zhou et al. [108] attributed this difference in behavior to the fact that these two materials exhibit distinct resistance to failure under the conditions described. They measured a peak temperature of 1400 ^{o}C in C-300 steel and 450 ^{o}C in Ti-6AL-4V inside the propagating shear bands. They reported a shear band width of 200-300 μm propagating at speeds up to 1200 m/s at an impact velocity

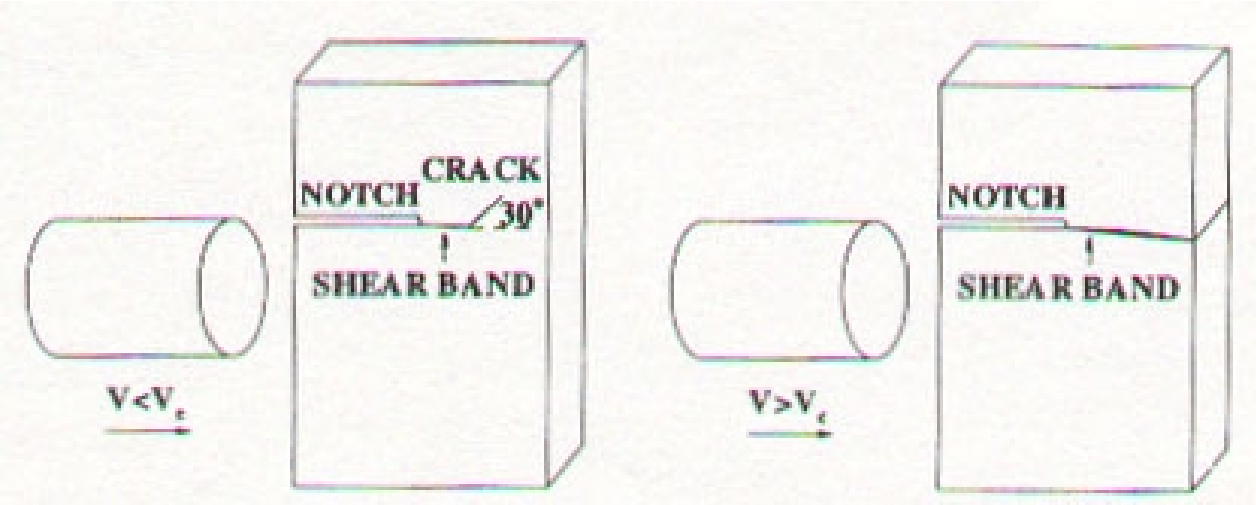

Figure 1.10: Schematic sketch of Zhou's experiments [108].

of 30 *m/s*. They also found a strong dependence of shear band speed on the impact velocity. A schematic outline of Zhou's work is presented in Fig. 1.10.

As shown, there is a discrepancy in the results obtained by Kalthoff [54] and Kalthoff and Winkler [55] on one side and the results obtained by Mason et al. [70] and Zhou et al. [108] on the other side. In Kalthoff's results, the two forms of failure do not occur simultaneously in a specimen at any particular impact velocity, but the results of later showed that for intermediate impact velocities, both forms were present at the same time. In order to reconcile the difference in these results, Zhou et al. [110] experimented with C-300 steel double and single notch specimens, this is to account for double notch specimen used by Kalthoff and the single notch specimen used in the other experiments. The results showed that the difference in specimen geometry is not the reason for the differing behaviors. Mason et al. [71] experimented with 300 maraging steel hardened differently. The states used, following a heat treatment, were under-aged, peak-aged and over-aged. The size of the specimens used was half of the size of the specimens used by of Kalthoff and Winkler [54], [55], Mason et al. [70] and Zhou et al. [108]. The results showed that the critical impact velocity at which shear bands initiate equals 33 to 35 *m/s* and is independent of the aging condition. However, shear band propagation velocity depends upon the aging condition; shear bands

in under-aged material propagated at 300 *m/s* and in peak-aged material propagated at 1000 *m/s*. Furthermore, a transition from Mode II to mixed-mode crack propagation was consistently seen in the under-aged specimens and sometimes in the over-aged specimens.

Numerical finite element simulations of Kalthoff's [54, 55] experiments were conducted by Needleman and Tvergaard [77], Zhou et al. [109], Batra and Nechitalio [23], Batra and Gummalla [12], and Batra and Ravisankar [26]. In all but the last one of the above simulations, a plane strain deformation was assumed and different constitutive relations were used to model the thermoviscoplastic response of the material. Needleman and Tvergaard [77] analyzed a double edge notch specimen to study the transition behavior from brittle to ductile failure with increasing impact velocity. They modelled the velocity on the impacted boundary as half the velocity of the projectile and concluded that at a higher rate of loading, the softening region grows more rapidly and thermal softening is the dominant factor near the notch. They reported that the mesh in the vicinity of the crack tip became severely distorted. Zhou et al. [109] studied a single notch C-300 steel and assumed the velocity on the impacted boundary equal to the projectile velocity. They assumed that the ductile failure occurs when the equivalent plastic strain reaches a critical value depending on the strain rate, while the tensile failure occurs when the maximum tensile stress exceeds three times the yield stress. They found good agreement with their [108] experimental results.

Batra and Nechitalio [23] modelled both the projectile and the plate in Kalthoff's [54], [55] experiments. The results from the evolution of stress and plastic strain suggested that, with an increase in impact velocity and a decrease in notch radius, there is a transition in the failure mode from a tensile crack opening at 70^o from the notch axis to a shear band propagating at -5^o to -10^o from the notch axis. Batra and Gummalla [12] used a single notch model similar to the model of Zhou et al. [109] and studied the effect of material and geometric parameters on the deformations near the notch tip. They assumed that the brittle fracture occurs when the maximum tensile stress equals twice the yield stress of the material in a quasistaic tension test and a shear band initiates when the effective plastic strain at a point equals 0.5. They found that for high strength steels, a shear band initiates from

the bottom of the deformed notch and propagates in the direction of the impact velocity at an angle of about -10^o from the axis of the notch. However, for moderate strength steels, two shear bands, one at -10^o and the other at -128^o to the notch axis, propagate into the plate material. Batra and Ravisankar [26] used DYNA3D to study the three-dimensional thermomechanical deformations of Kalthoff's experiment. Their simulations showed that the maximum speed imparted to points on the plate's impact surface equals 90% of the projectile speed. Moreover, the three-dimensional deformations are quite different from the two-dimensional deformations, in that, the later predicted earlier initiation of the shear band.

Chapter 2

Failure Mode Transition Speeds *

2.1 Introduction

During impact loading of pre-notched plates, Kalthoff [54] and Kalthoff and Winkler [55] observed that with an increase in the impact speed, the failure mode changed from brittle failure at a point on the upper surface of the notch tip to ductile failure in the form of a shear band initiating from a point on the lower surface of the notch tip; the lower surface of the notch is adjacent to the impacted edge of the plate. However, in the Charpy V-notch test, ductile failure ensues at low loading rates or at high temperatures and brittle failure at high loading rates or at low temperatures. Tvergaard and Needleman [95, 96] and Needleman and Tvergaard [77] have numerically analyzed thermomechanical deformations of these two configurations by using Gurson's [46] flow potential and a power law type thermoviscoplastic relation. They showed that predictions from the same set of governing equations are in qualitative agreement with the seemingly contradictory observations in the two tests. Needleman and Tvergaard [77], Zhou et al. [109], Batra and Nechitailo [23], Batra and Gummalla [12] and Batra and Ravisankar [26] have numerically studied the Kalthoff

*The material in this chapter is from the paper " Failure Mode Transition Speeds in an Impact Loaded Prenotched Plate with Four Thermoviscoplastic Relations" by R. C. Batra and N. A. Jaber which has been accepted for publication in the Int. J. Fracture.

problem. Whereas Needleman and Tvergaard and Zhou et al. employed a power law type relation to model the strain hardening and strain-rate hardening of the material, Batra et al. used the Johnson-Cook [52] relation. None of these studies computed the impact speed at which the failure mode transition occurs. Also, it will be interesting to compare the thermomechanical response predicted by different thermoviscoplastic relations after they have been calibrated with the same set of test data. Batra and Kim [19] conducted such studies for the initiation and development of an adiabatic shear band in a thermoviscoplastic body deformed in simple shear, and Batra and Jayachandran [21] and Batra and Adam [10] used different relations to analyze the steady state penetration of a thermoviscoplastic target by a rigid hemispherical nosed penetrator.

We use four thermoviscoplastic relations, namely, the Litonski-Batra, the Johnson-Cook, the Bodner-Partom and a power law to analyze the plane strain thermomechanical deformations of a prenotched plate used in Kalthoff's experiments. We note that the only mechanical property listed in Kalthoff's paper is the quasistatic yield strength of the material of the plate. We use values of material parameters, modified to the case of three-dimensional deformations, that Batra and Kim [19] found by calibrating the four thermoviscoplastic relations against the experimental data of Marchand and Duffy [69] who tested thin-walled HY100 steel tubes in torsion. Batra and Kim [19] assumed that deformation of the material near the middle of the tube corresponded to that of simple shearing and determined the values of material parameters by solving an initial-boundary-value problem till the computed stress-strain curve at a nominal strain rate of 3300/s matched closely with that obtained from the test data. It is found that the four viscoplastic relations predict different values of the impact speed at which the failure mode in the Kalthoff problem changes from brittle to ductile. However, the qualitative nature of results computed with the four thermoviscoplastic relations is the same. We use the Bodner-Partom relation to ascertain the effect of the notch tip radius and the power law to scrutinize the effect of the quasistatic yield stress of the material on the transition speed.

2.2 Formulation of the Problem

A schematic sketch of the problem studied is depicted in Fig. 2.1. A cylindrical rod of diameter equal to the distance between the two notches in a prenotched plate strikes the side of the plate at normal incidence with speed v_0. The cylindrical rod and the plate are made of the same microporous material and the plate before being impacted rests on a smooth rigid surface.

We assume that a plane strain state of deformation prevails in the plate. The three-dimensional numerical solution of the problem by Batra and Ravisankar [26] reveals that this is a good approximation of the deformations occurring in the central 75% of the thickness of the plate. In rectangular Cartesian coordinates and in the absence of body forces and sources of internal energy, equations governing the deformations of the plate are

$$(\rho J(1-f))^{\cdot} = 0, \tag{2.1}$$

$$\rho_0(1-f_0)\dot{\mathbf{v}} = \mathrm{Div}\,\mathbf{T}, \tag{2.2}$$

$$\mathbf{T}\mathbf{F}^T = \mathbf{F}\mathbf{T}^T, \tag{2.3}$$

$$\rho_0(1-f_0)\dot{e} = -\mathrm{Div}\,\mathbf{Q} + tr(\mathbf{T}\dot{\mathbf{F}}^T). \tag{2.4}$$

Here ρ is the present mass density, f the porosity, v the velocity of a material point $\mathbf{X}$ presently occupying the place $\mathbf{x}$, $\mathbf{F} = \partial\mathbf{x}/\partial\mathbf{X}$, $J = det\,\mathbf{F}$, $\mathbf{T}$ the first Piola-Kirchhoff stress tensor, e the specific internal energy, $\mathbf{Q}$ the heat flux per unit area in the reference configuration, Div the divergence operator with respect to coordinates in the reference configuration, a superimposed dot indicates the material time derivative, tr is the trace operator and $\mathbf{F}^T$ equals the transpose of $\mathbf{F}$. A subscript 0 on a quantity indicates its value in the reference configuration.

We assume that the plate material is homogeneous and isotropic and use the following

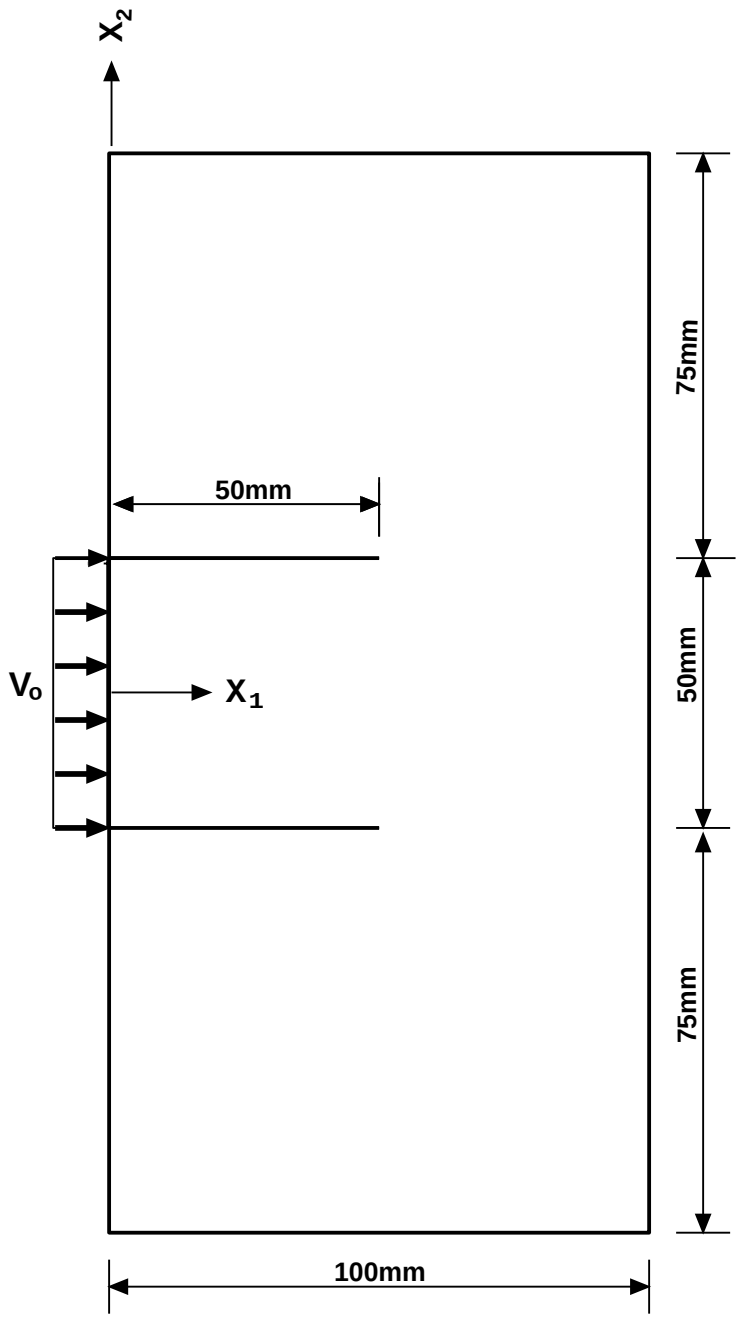

Figure 2.1: A schematic sketch of the problem studied

constitutive relations to model its thermoviscoplastic response.

$$\dot{\boldsymbol{\sigma}} - \boldsymbol{\Omega}\boldsymbol{\sigma} + \boldsymbol{\sigma}\boldsymbol{\Omega} = \frac{E(1-f)}{(1+\nu)}\mathbf{D}^e + \frac{\nu E(1-f)}{(1+\nu)(1-2\nu)}(tr\,\mathbf{D}^e)\mathbf{1}, \tag{2.5}$$

$$\mathbf{D}^e = \mathbf{D} - \mathbf{D}^p - \alpha\dot{\theta}\mathbf{1},\ 2\mathbf{D} = \operatorname{grad}\mathbf{v} + (\operatorname{grad}\mathbf{v})^T,\ 2\boldsymbol{\Omega} = \operatorname{grad}\mathbf{v} - (\operatorname{grad}\mathbf{v})^T, \tag{2.6}$$

$$\mathbf{D}^p = \frac{(1-f)\sigma_e\dot{\varepsilon}^p}{tr(\boldsymbol{\sigma}\mathbf{N}^T)}\mathbf{N},\ \mathbf{N} = \frac{\partial\Phi}{\partial\boldsymbol{\sigma}}, \tag{2.7}$$

$$\Phi \equiv \frac{3}{2}\frac{tr(\mathbf{s}\mathbf{s}^T)}{\sigma_e^2} + 2f^*q_1\cosh\left(\frac{q_2 tr\boldsymbol{\sigma}}{2\sigma_e}\right) - 1 - q_1^2 f^{*2} = 0, \tag{2.8}$$

$$\mathbf{s} = \boldsymbol{\sigma} - \frac{1}{3}(tr\,\boldsymbol{\sigma})\mathbf{1}, \tag{2.9}$$

$$\dot{\varepsilon}^p = g(\sigma_e,\ \epsilon^p,\ \theta), \tag{2.10}$$

$$f^* = \begin{cases} f \text{ if } f \le f_c, \\ f_c + \left(\dfrac{f_u - f_c}{f_f - f_c}\right)(f - f_c) \text{ otherwise,} \end{cases} \tag{2.11}$$

$$\dot{f} = (1-f)tr\,\mathbf{D}^p + \frac{f_2\dot{\varepsilon}^p}{s_2\sqrt{2\pi}}\exp\left(-\frac{1}{2}\left(\frac{\varepsilon^p - e_N}{s_2}\right)^2\right), \tag{2.12}$$

$$\mathbf{q} = -\kappa\left(1 - \frac{3}{2}f\right)\operatorname{grad}\theta, \tag{2.13}$$

$$\dot{e} = c\dot{\theta} + tr(\boldsymbol{\sigma}\mathbf{D}^e + \alpha\dot{\theta}\boldsymbol{\sigma}), \tag{2.14}$$

$$\mathbf{T} = J\boldsymbol{\sigma}(\mathbf{F}^{-1})^T,\ \mathbf{Q} = J(\mathbf{F}^{-1})\mathbf{q}. \tag{2.15}$$

Here $\boldsymbol{\sigma}$ is the Cauchy stress tensor that is related to the first Piola-Kirchhoff stress tensor by eqn. $(2.15)_1$, $\boldsymbol{\Omega}$ the spin tensor, E Young's modulus, ν Poisson's ratio, α the coefficient of thermal expansion, $\mathbf{D}$ the strain-rate tensor, $\dot{\varepsilon}^p$ the effective plastic strain-rate, $\mathbf{q}$ the heat flux per unit area in the current configuration, κ the thermal conductivity, and c the specific heat. Other parameters characterizing the material are $q_1,\ q_2,\ f_2,\ s_2,\ e_N,\ f_c$ and

f_u. Equation (2.5) is the constitutive relation for a hypoelastic material and its left-hand side represents the Jaumann derivative of $\boldsymbol{\sigma}$.

The frame-indifference of $\boldsymbol{\sigma}$ implies that $\mathbf{N}$ and $\mathbf{D}^p$ are frame-indifferent (cf. eqn. (2.7)) and hence $\mathbf{D}^e$ is frame-indifferent. Therefore eqn. (2.5) is frame-indifferent. The factor $(1-f)$ on the right-hand side of eqn. (2.5) accounts for the degradation of the material strength due to the evolution of the porosity; this was also considered by Passman and Batra [80] and Kobayashi and Dodd [59]. Budiansky [31], amongst others, has given the dependence of the material properties upon f for a macroscopically isotropic composite consisting of a random dispersion of approximately spherical voids in a matrix material. These relations are more involved than the simple reduction of Young's modulus and the bulk modulus by $(1-f)$. Equation (2.8) is the yield function proposed by Gurson [46] and subsequently modified by Tvergaard [93]. Equations $(2.7)_2$ and $(2.7)_1$ follow from the assumptions that $\mathbf{D}^p$ is along the outward normal $\mathbf{N}$ to the yield surface $\Phi = 0$, and the plastic working $tr(\boldsymbol{\sigma}\mathbf{D}^p)$ equals $(1-f)\sigma_e\dot{\bar{\varepsilon}}^p$. The thermoviscoplastic relations described by equation (2.10) will be discussed below. The expression (2.11) for f^* was proposed by Tvergaard and Needleman [94] so that the computed results matched well with the test findings for the cup-cone fracture in a round tensile bar. They suggested the values $f_c \simeq 0.15$ and $f_f \simeq 0.25$.

The first term on the right-hand side of eqn. (2.12) gives the growth of voids due to plastic dilatation, and the second term, proposed by Chu and Needleman [35] equals the plastic strain controlled nucleation of voids. In eqn. (2.12), s_2 is the standard deviation of the normal distribution, f_2 the volume fraction of voids that would be nucleated if the deformation continued indefinitely, and e_N the plastic strain at which the void nucleation rate is maximum. Experimental studies of LeRoy [65] and Fisher [42] on spheroidized carbon steel reveal that a void perfusion strain exists at which the nucleation rate of voids is maximum; this strain can be taken as e_N. Perzyna [82] has employed a different evolution equation for f. Equation (2.13) is the Fourier law of heat conduction. Budiansky [31] proposed that the thermal conductivity of a porous material equals $(1-(3/2)f)$ of that for the matrix. Nearly all of the thermophysical material parameters may depend upon the temperature. However,

such dependencies have been ignored for the sake of simplicity.

For the initial conditions we take

$$\boldsymbol{\sigma}(\mathbf{x},\ 0) = \mathbf{0},\ f(\mathbf{x},\ 0) = f_0,\ \rho(\mathbf{x},\ 0) = \rho_0,\ \mathbf{v}(\mathbf{x},\ 0) = \mathbf{0},\ \theta(\mathbf{x},\ 0) = \theta_0. \tag{2.16}$$

That is, the plate is initially stress free and is at a uniform temperature θ_0. All bounding surfaces of the plate including the surfaces of the two notches are assumed to be traction free and thermally insulated. The surface of the plate impacted by the cylindrical rod is taken to be smooth and the normal velocity, v_1, on it is given by

$$v_1 = \begin{cases} 0.3v_0 t, & 0 \le t \le 2\mu s, \\ v_0(0.525 + 0.0375t), & 2 \le t \le 10\mu s, \\ 0.9v_0, & 10\mu s \le t < t_s, \\ 0, & t \ge t_s, \end{cases} \tag{2.17}$$

where v_0 is the speed of the projectile, and t_s equals the time when the projectile separates from the plate. The expression (2.17) for v_1 is obtained by fitting straight lines to the data of Batra and Ravisankar [26] who conducted three-dimensional numerical simulations of the problem studied herein with DYNA3D that models the thermoviscoplastic response of the material by the Johnson-Cook relation. Their simulations with a different constitutive relation and also for a steel with a higher value of the yield stress in a quasistatic simple compression test resulted in expression (2.17) for the normal velocity imparted to the plate particles.

We assume that the plate is made of a HY100 steel and that the material exhibits strain hardening, strain-rate hardening and thermal softening and model these effects by the following four thermoviscoplastic relations.

2.2.1 Litonski-Batra Relation

Batra [8] generalized the one-dimensional relation of Litonski [68] to equation (18) appropriate for three dimensional deformations.

$$\dot{\varepsilon}^p = \max\left\{0, \frac{1}{b}\left[\left(\frac{\sigma_e}{\sigma_0\left(1+\dfrac{\varepsilon^p}{\varepsilon_y}\right)^n(1-\nu_s\theta)}\right)^{1/m} - 1.0\right]\right\}. \tag{2.18}$$

Here σ_0 is the yield stress of the material in a quasistatic simple tension or compression test, parameters b and m characterize the strain-rate hardening of the material, ε_y and n its strain hardening and ν_s its thermal softening. It is evident from eqn. (2.18) that a material point deforms plastically only when $\sigma_e > \sigma_0\left(1+\dfrac{\varepsilon^p}{\varepsilon_y}\right)^n(1-\nu_s\theta)$ there.

2.2.2 Power law

Klopp et al. [58] and Hartley et al. [48] described the experimental shear stress-shear strain curve during torsional deformations of a steel tube at different strain rates by a power law. Several investigators, e.g. see Needleman and Tvergaard [77], have used its three-dimensional version (2.19) obtained by replacing the shear stress and the shear strain by the effective stress and the effective plastic strain respectively.

$$\dot{\varepsilon}^p = \begin{cases} \dot{\varepsilon}_0\left(\dfrac{\sigma_e}{\sigma_0}\right)^{1/m}\left(\dfrac{\varepsilon^p}{\varepsilon_y}\right)^{-n/m}\left(\dfrac{\theta}{\theta_0}\right)^{-\gamma/m} & \text{if } \sigma_e \geq \sigma_0, \\ 0 & \text{if } \sigma_e \leq \sigma_0. \end{cases} \tag{2.19}$$

Here $\dot{\varepsilon}_0$ is a reference strain-rate and the temperature is measured in Kelvin. The viscoplastic response is characterized by material parameters $m,\ n,\ \gamma,\ \sigma_0,\ \theta_0,\ \varepsilon_y$ and $\dot{\varepsilon}_0$; θ_0 is usually taken as the room temperature in Kelvin and ε_y the plastic strain at the onset of plastic deformations in a simple tension or compression test.

2.2.3 Bodner-Partom Relation

Plastic deformations are assumed to occur for all values of the effective stress, and the effective plastic strain-rate is given by (e.g. see Bodner and Partom [29])

$$\dot{\varepsilon}^p = D_0 \exp\left[-\frac{1}{2}\left(\frac{K^2}{3\sigma_e^2}\right)^n\right], \tag{2.20}$$

where

$$K = K_1 - (K_1 - K_0)\exp(-mW_p),\ n = \frac{a}{\theta} + b, \tag{2.21}$$

$$W_p = \int_0^t tr(\boldsymbol{\sigma}\mathbf{D}^p)dt. \tag{2.22}$$

Parameters K_1, K_0, D_0, m, a and b determine the thermoviscoplastic response of the material, and the temperature θ in equation $(2.21)_2$ is measured in Kelvin.

2.2.4 Johnson-Cook Relation

Based on the test data at moderate values of the strain-rate and at different temperatures, Johnson and Cook [52] proposed that

$$\dot{\varepsilon}^p = \dot{\varepsilon}_0 \max\left\{\exp\left[\frac{1}{C}\left(\frac{\sigma_e}{(A + B(\varepsilon^p)^n)\left(1 - \left(\frac{\theta - \theta_0}{\theta_m - \theta_0}\right)^m\right)} - 1\right)\right], 0\right\}. \tag{2.23}$$

The reference strain-rate, $\dot{\varepsilon}_0$, is usually taken as $1/s$ and θ_m equals the melting temperature of the material. When $\theta = \theta_m$, the material behaves as a perfect fluid.

2.3 Numerical Solution of the Governing Equations

Because of the relation $(2.15)_1$ between $\mathbf{T}$ and $\boldsymbol{\sigma}$ and the constitutive relation $(2.15)_1$, the balance of moment of momentum (2.13) is identically satisfied. The present mass density, ρ, can be computed from eqn. (2.1) if the deformation and current value of the porosity are known. Thus the independent variables are $\mathbf{X}$ and t, and the dependent variables are $\mathbf{x}$, f and θ. Equations (2.2) and (2.4) are second-order nonlinear hyperbolic and parabolic partial differential equations (PDEs) for $\mathbf{x}$ and θ; the two are coupled through the source term in (2.4) and the dependence of $\mathbf{T}$ upon θ through the thermoviscoplastic relation (2.10). There is no easy way to write eqns. (2.2) and (4) in terms of x and θ since T is given by $(2.15)_1$ and $\boldsymbol{\sigma}$ is a solution of the ordinary differential equation (2.5) which involves $\mathbf{D}^p$ and θ through $(2.6)_1$.

The problem formulated above is numerically solved by the finite element method. The domain of study is divided into constant strain triangular (CST) elements. The Galerkin approximation of equations (2.2) and that obtained by substituting from (2.13), (2.14) and $(2.15)_2$ into (2.4) yields a coupled set of ordinary differential equations for nodal values of the two components of the velocity and the temperature. Equations (2.1), (2.5), (2.10) and (2.12) are integrated at the centroid of an element. The value of σ_e is computed from the yield function (2.8) after $\boldsymbol{\sigma}$ and hence $\mathbf{s}$ have been determined. Thus, for the plane strain problem, the number of unknowns and the number of coupled nonlinear ordinary differential equations (ODEs) to be integrated equal 3 (nodes) + 7 (elements). These ODEs subject to the prescribed initial conditions are integrated with respect to time t by using the subroutine LSODE (Livermore Solver for Ordinary Differential Equations) included in the package ODEPACK. Because of the storage limitations, we used the nonstiff option in LSODE with $MF = 10$, $ATOL = RTOL = 10^{-6}$. The ODEs are integrated by the Adams method; the order of the method and the time step size are adaptively adjusted to solve the ODEs within the prescribed tolerance. In LSODE, the value of the parameter MF selects the method, and the values of ATOL and RTOL equal respectively the absolute and the

relative tolerances on the solution variables.

We modified the computer code developed by Batra and Jin [20] for the analysis of plane strain thermomechanical deformations of a viscoplastic body with the Litonski-Batra relation. The modifications include the incorporation of the Bodner-Partom and the Johnson-Cook relations and the power law. Batra and Jin [20] also multiplied equations (2.1), (2.5), (2.10) and (2.12) by a test function, integrated the resulting equations over the domain of study and obtained ODEs for nodal values of the mass density, porosity and four components of the stress tensor. Here these equations are integrated at the centroids of elements thereby reducing the total number of unknowns. Recall that for a CST element, the deformation gradient and the strain-rate etc. are constants over the element. For the Johnson-Cook thermoviscoplastic relation results computed with the current code were found to be quite close to those obtained with DYNA2D until the time the deformations localized into a narrow band in the prenotched plate. Whereas our code accounts for heat conduction, thermal expansion and the evolution of the porosity, these are ignored in DYNA2D. The DYNA2D employs the 4-node quadrilateral element with one-point integration rule, an hour-glass control, a lumped mass matrix, and the explicit central-difference method to integrate the ODEs and is computationally very efficient. In our code, the lumped mass matrix for the CST elements is obtained by the row sum technique.

Results computed with DYNA2D for the prenotched plate with the Jaumann and the Green-Naghdi stress rates on the left-hand side of eqn. (2.5) were found to be identical with each other. It is primarily because the plastic strain-rates at points near the notch tip are significantly larger than the elastic strain-rates and the latter appear in the left-hand side of eqn. (2.5).

2.4 Values of Material Parameters

Batra and Kim [19] used the aforestated four thermoviscoplastic relations to study the initiation and development of shear bands in a viscoplastic block made of a HY-100 steel and deformed in simple shear. They simulated the dynamic torsional tests of Marchand and Duffy [69] on thin-walled HY-100 steel tubes as a simple shearing problem, determined the values of material parameters by solving an initial-boundary-value problem and adjusted the values of material parameters till the computed shear stress-shear strain curve closely matched with the experimental curve of Marchand and Duffy. During the iterative process of finding the appropriate values of material parameters, the value of the quasistatic yield stress of the material was kept the same as that provided by Marchand and Duffy's tests and that of the strain hardening exponent was kept close to the value Marchand and Duffy found by curve fitting their test data. The values of other material parameters are not uniquely determined since the underlying initial-boundary-value problem need not have a unique solution. Batra and Kim's values of material parameters were suitably modified to account for three-dimensional deformations of the viscoplastic body.

Values assigned to material parameters in the four thermoviscoplastic relations are listed below.

(a) Litonski-Batra

$\nu_s = 0.00185/^\circ C$, $\varepsilon_y = 0.007$, $n = 0.107$, $m = 0.0117$, $b = 17320s$.

(b) Power law

$\dot{\varepsilon}_o = 5.77 \times 10^{-5}/s$, $\varepsilon_y = 0.007$, $\theta_0 = 300K$, $m = 0.0117$, $n = 0.107$, $\gamma = -0.27$.

(c) Bodner-Partom

$a = 1200K$, $b = 0$, $K_1 = 2950MPa$, $K_0 = 2937MPa$, $m = 3510MPa$, $D_0 = 1.732 \times 10^8/s$.

(d) Johnson-Cook

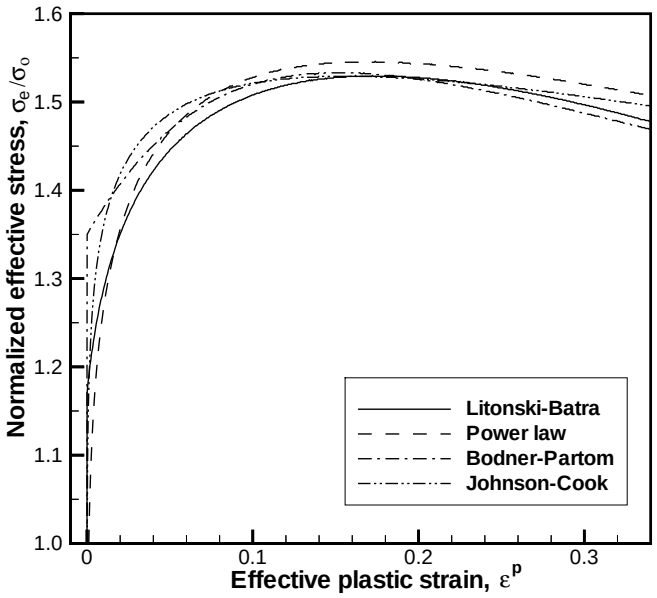

Figure 2.2: Effective stress vs. effective plastic strain curves for homogeneous deformations of a block deformed at an average strain-rate of 3300/s.

$$A = 316MPa,\ B = 1067MPa,\ n = 0.107,\ \theta_m = 1500K,\ \theta_0 = 300K,\ m = 0.7,$$
$$C = 0.0277,\ \dot{\varepsilon}_0 = 3300/s.$$

Values of other material parameters used to compute results are:

$$\begin{aligned}
&\sigma_0 = 702\,\text{MPa},\ \rho_0 = 7860\,\text{kg/m}^3,\ c = 473J/kg\ ^\circ C,\ K = 49.73W/m^2\,^\circ C,\\
&\alpha = 11.5\times 10^{-6}/^\circ C,\ E = 208\,\text{GPa},\ \nu = 0.3,\ f_2 = 0.04,\ e_N = 0.3,\\
&s_2 = 0.1,\ q_1 = 1.5,\ q_2 = 1.0,\ f_c = 0.15,\ f_f = 0.25,\ f_u = 0.667,\ f_0 = 0.0\ .
\end{aligned} \tag{2.24}$$

Values of $e_N,\ s_2,\ q_1,\ q_2,\ f_c,\ f_f,\ f_u$ etc. are for a typical steel. Fig. 2.2 depicts the computed effective stress versus the effective plastic strain curves for homogeneous deformations of a block deformed at a nominal strain-rate of $3300/s$. It is clear that the four curves are quite close to each other. Note that the expanded scale along the vertical axis magnifies the small differences among the four curves.

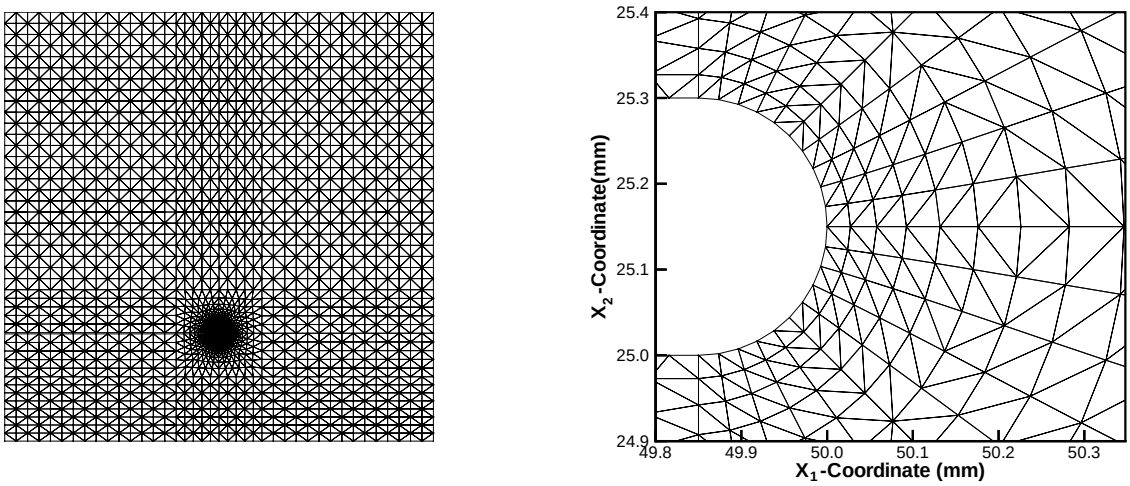

(a) (b)

Figure 2.3: (a) Finite element discretization of the problem domain, (b) Details of the finite element mesh in the region surrounding the notch tip.

2.5 Computation and Discussion of Results

Due to the symmetry of the plate and the applied initial and boundary conditions about the x_1-x_3 plane passing through the centroid of the plate, deformations of only the upper half of the plate are analyzed. For a notch tip radius of 0.15 mm, Fig. 2.3a exhibits the discretization of the domain into three-noded triangular elements, and Fig. 2.3b shows the details of the mesh around the notch tip. There are 40 elements around the notch tip surface and the element size increases gradually as one moves away from this surface. The qualitative and quantitative nature of results computed with a finer mesh was essentially unchanged at points close to the notch tip surface. Results presented below are with a fixed mesh. Computations were stopped when one of the elements abutting the notch tip surface got severely distorted.

For each one of the four thermoviscoplastic relations and for the notch tip radius r_0 =

0.15mm, impact speed $v_0 = 20m/s$ and time $t = 25\mu s$, Figs. 2.4, 2.5 and 2.6 evince respectively the fringe plots of the effective plastic strain, the normalized maximum principal stress σ_p/σ_0 and the normalized maximum shear stress in a small region around the notch tip. The results are qualitatively similar for the four thermoviscoplastic relations. In each case, the maximum effective plastic strain occurs at a point on the lower surface of the notch tip and its value equals at least 0.30. The intensely deformed region is nearly of the same size and is likewise oriented. Small kinks in the lower part of the bounding surface of the notch tip are due to the severe distortions of the elements in that region. These plots suggest that the ductile failure will initiate from a point on the lower part of the notch tip surface. A comparison of the bounding surface of the undeformed notch shown in Fig. 2.3b with that of the deformed one in Fig. 2.4 reveals that the notch surface is not symmetrically deformed about its center-line. This is to be expected since the applied load is asymmetric about the centerline of the notch. Points on the lower traction free surface of the notch move to the right, i.e., in the direction of the prescribed velocity while those on the upper surface remain essentially stationary; e.g. see the velocity plots given in Fig. 4 of Batra and Gummalla [12]. The velocity plots for the results computed herein were similar to that shown in Fig. 4 of Batra and Gummalla, and are therefore omitted. This relative movement of material particles induces stretching and hence tensile stresses in the region adjoining the upper part of the notch tip surface; this is depicted in Fig. 2.5. For each one of the four thermoviscoplastic relations, the maximum principal tensile stress occurs at a point situated approximately 0.09mm above the upper surface of the notch tip and equals almost $2.5\sigma_0$. The principal stress is compressive in the region near the lower surface of the notch tip where the effective plastic strain is high. These observations are consistent with the results of previous investigations of the problem by Needleman and Tvergaard [77], Zhou et al. [109], Batra and Nechitailo [23], Batra and Gummalla [12] and Batra and Ravisankar [26], and suggest that a brittle failure will ensue from a point on the upper surface of the notch tip. Needleman and Tvergaard used a power law type viscoplastic relation, Zhou et al. modeled thermal softening by an exponential function, and the other three investiga-

tions employed the Johnson-Cook relation. Needleman and Tvergaard's results as well as those of the present study suggest that the consideration of the porosity does not change the qualitative and the quantitative nature of results. The maximum value of the porosity computed at any point in the plate before an element got severely distorted equalled 2.75%. One reason could be that as soon as the effective plastic strain at a point becomes large enough for the voids to nucleate, the mesh gets severely distorted and computations need to be ceased. Our attempts to adaptively refine the mesh resulted in noticeable oscillations in the evolution of the effective stress at a point and thus were abondened. These oscillations were due to the transfer of the data from the old mesh to the new one. In the plane strain transient thermomechanical deformations of a viscoplastic block studied by Batra and Jin [20] and by Batra and Ko [17], these oscillations were not large enough to significantly affect subsequent computations. However, for the present problem, points on the notch surface moved noticeably and attempts to smoothen the adaptively generated mesh did not improve the situation. Results presented herein are, therefore, with a fixed mesh.

The fringe plots of the normalized maximum shear stress depicted in Fig. 2.6 indicate that for each one of the four viscoplastic relations the maximum shear stress occurs in a region directly ahead of the notch tip. Chen and Batra [34] scrutinized the asymptotic deformation fields around a shear band tip propagating at a uniform velocity in a thermoviscoplastic body undergoing plane strain deformations. They modeled the shear band as a singular surface and observed that the jump in the shear stress across the singular surface acted as a driving force for the propagation of a shear band. Hence in the present problem, a shear band will propagate predominantly along the axis of the notch and a secondary band may propagate in a direction making an angle of about 130° clockwise from the axis of the notch. The existence of a secondary shear band is evidenced by the two lobes of high effective plastic strain in Fig. 2.4. Experimental observations of Kalthoff et al. [54], Mason et al. [70] and Zhou et al. [108] indicate that a shear band propagates nearly along the axis of the notch. Thus the direction of propagation of a shear band predicted by each one of the four thermoviscoplastic relations is close to that observed experimentally.

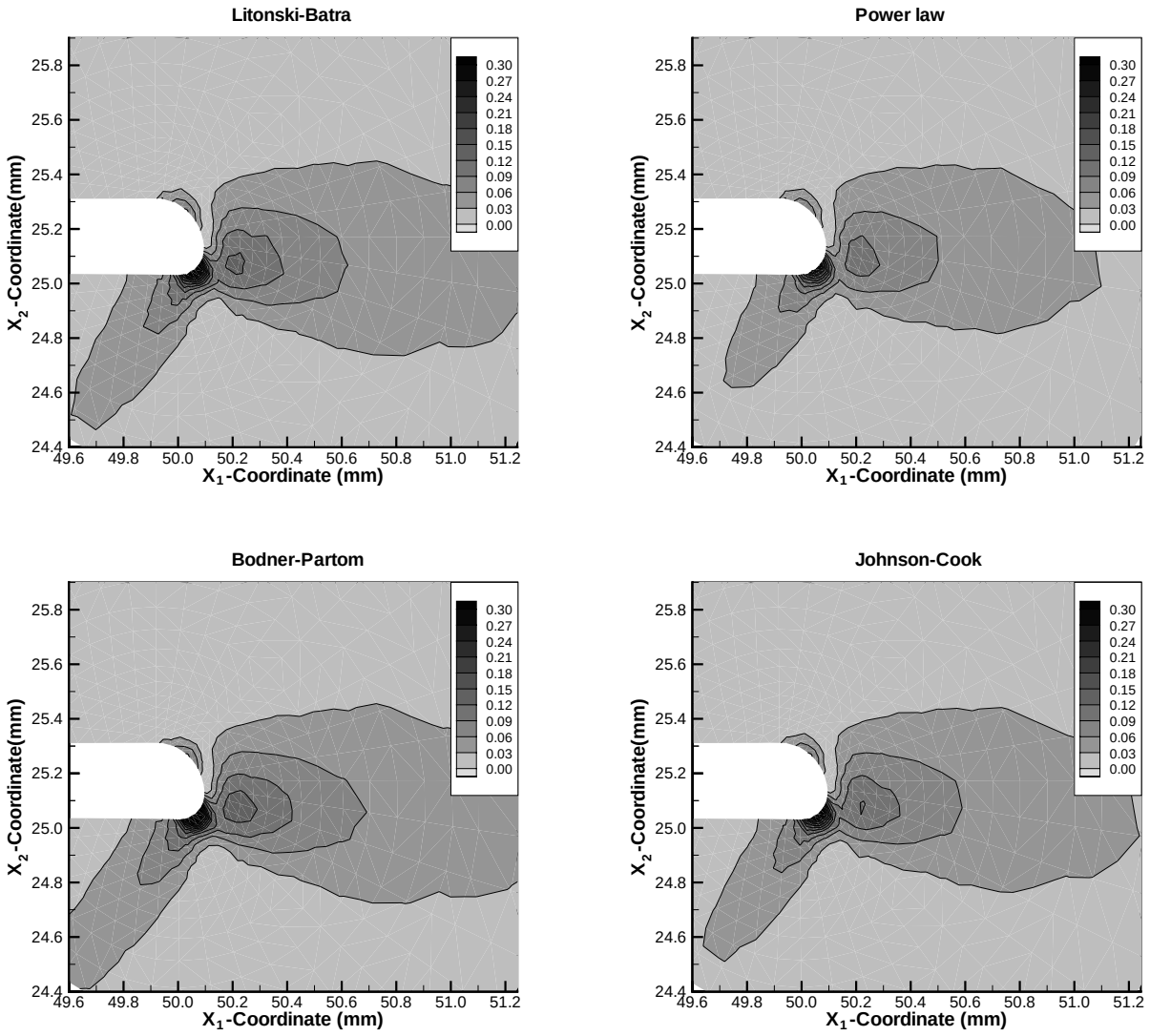

Figure 2.4: For the four thermoviscoplastic relations, fringe plots in a small region surrounding the surface of the notch tip, of the effective plastic strain.

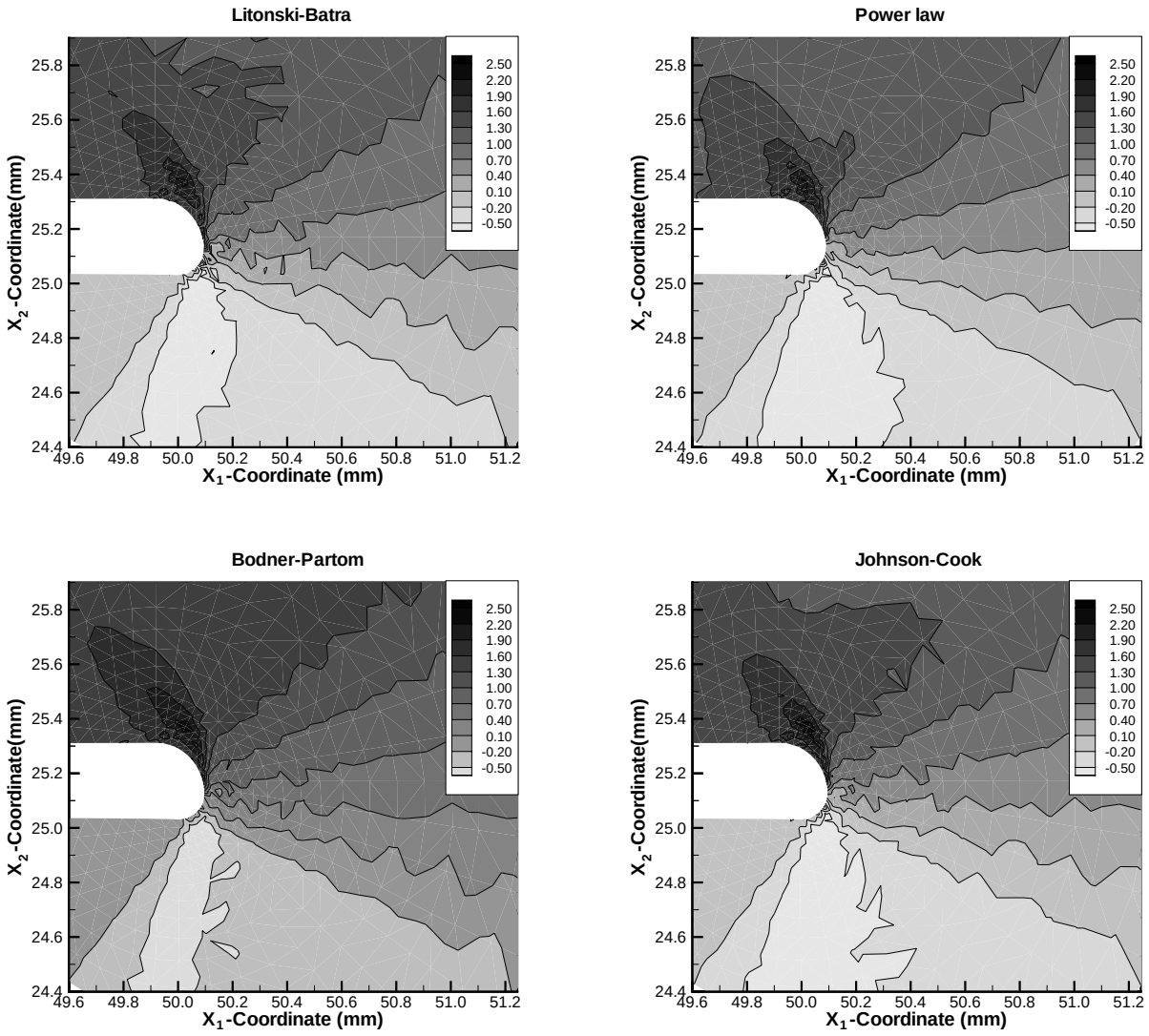

Figure 2.5: For the four thermoviscoplastic relations, fringe plots in a small region surrounding the surface of the notch tip, of the normalized maximum principal stress.

In an attempt to quantitatively delineate the differences, if any, in the results predicted by the four thermoviscoplastic relations we have plotted in Figs. 2.7 and 2.8 the time histories of the normalized effective stress, the effective plastic strain, the normalized maximum principal stress and the temperature at points P and Q. Points P and Q are at the centroids of elements abutting the notch tip surface, and lines OP and OQ are inclined respectively at 45° clockwise and 45° counterclockwise to the axis of the notch. Point O coincides with the centroid of the notch tip. For the values of material parameters used herein, the dilatational wave speed equals about 5.8 mm/μs. The effective stress begins to grow at points around the notch tip soon after the loading wave arrives there at $t \simeq 8\mu s$, and the 200mm long striker rod separates from the prenotched plate at $t_s \simeq 32\mu s$. Once the effective stress at a point exceeds σ_0, the material point starts deforming plastically. The initial effective plastic strain-rate at point P or Q computed with each one of the four thermoviscoplastic relations is virtually the same even though the effective stress is a little different. At $t \simeq 14\mu s$, the effective plastic strain-rate computed at point Q with the four constitutive relations begins to differ; the power law gives the lowest value and the Bodner-Partom relation the highest value. Each one of the four constitutive relations gives an effective plastic strain-rate at point P of the order of $10^4/s$. Results computed at point Q with the four thermoviscoplastic relations are closer to each other than those at point P. During the time interval $0 \leq t \leq 30\mu s$, the maximum effective plastic strain induced at point Q is less than half of that at point P. However, the magnitude of the maximum tensile principal stress at point Q is nearly three times that of the maximum compressive principal stress at point P. The temperature rise at point P is approximately three times as large as that at point Q. Note that the maximum principal tensile stress occurs in an element away from the notch surface. The computed temperature is highest for the Bodner-Partom relation and least for the power law.

Fig. 2.9 exhibits at $t = 25\mu s$ the angular variation of the normalized maximum principal stress, the effective plastic strain, the temperature and the porosity at the centroids of elements abutting the notch tip surface; positive angles are measured counterclockwise from the axis of the notch. Only a small region of the material adjacent to the notch tip surface and

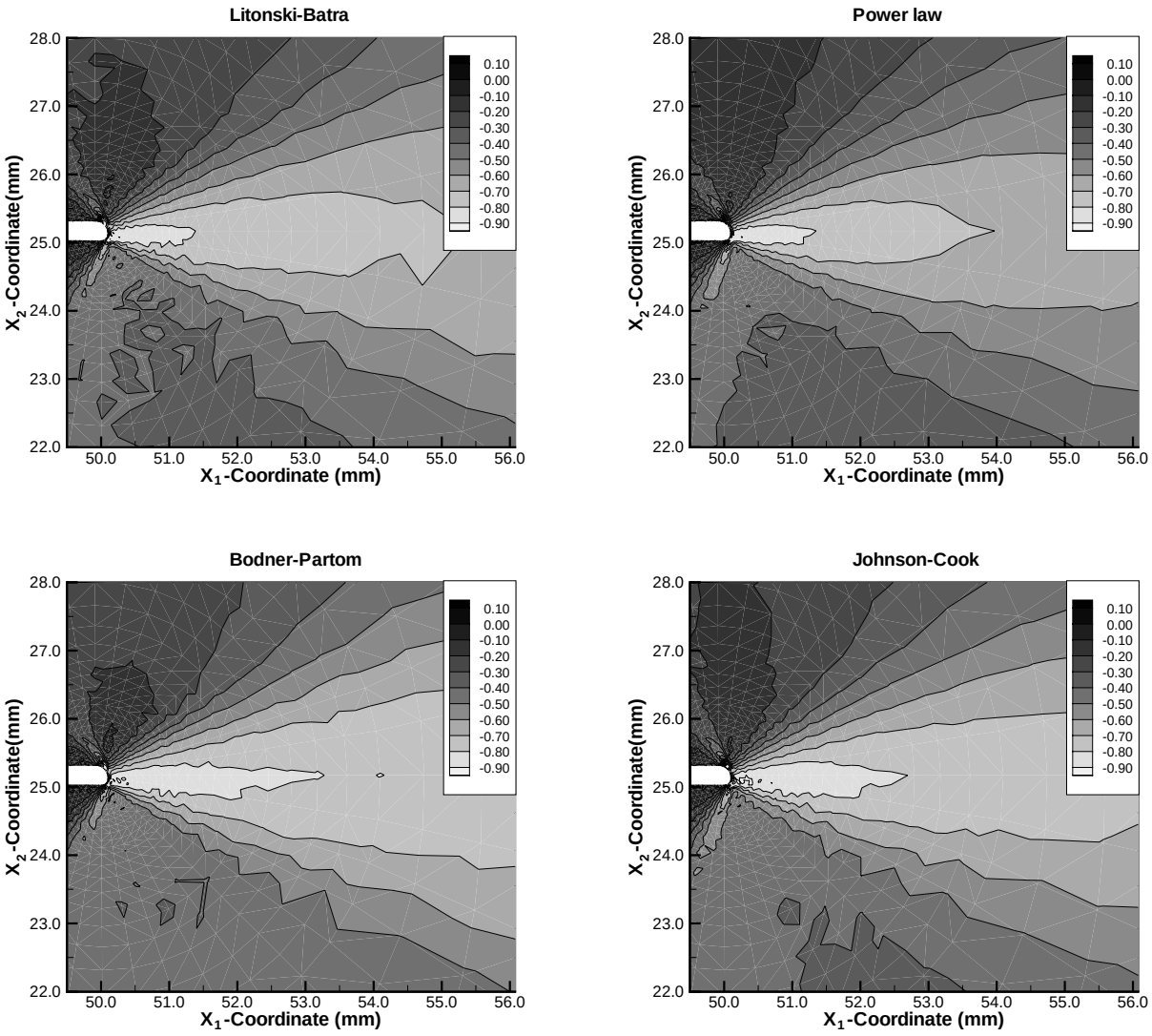

Figure 2.6: For the four thermoviscoplastic relations, fringe plots in a small region surrounding the surface of the notch tip, of the normalized maximum shear stress.

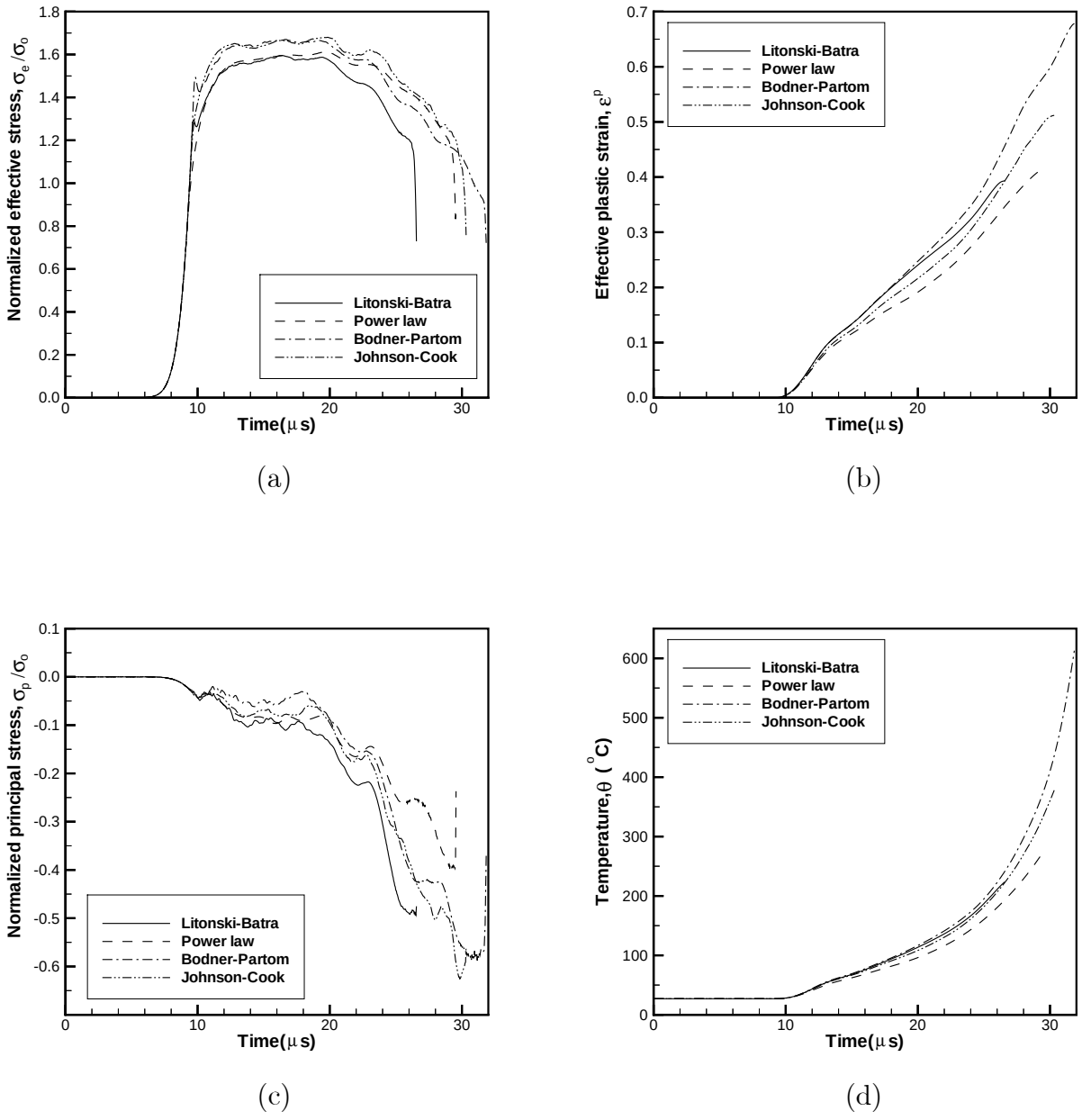

Figure 2.7: For the four thermoviscoplastic relations, time histories at the point P on the notch surface that is located at 45° clockwise from the axis of the notch of (a) the normalized effective stress, (b) the effective plastic strain, (c) the normalized maximum principal stress, and (d) the temperature.

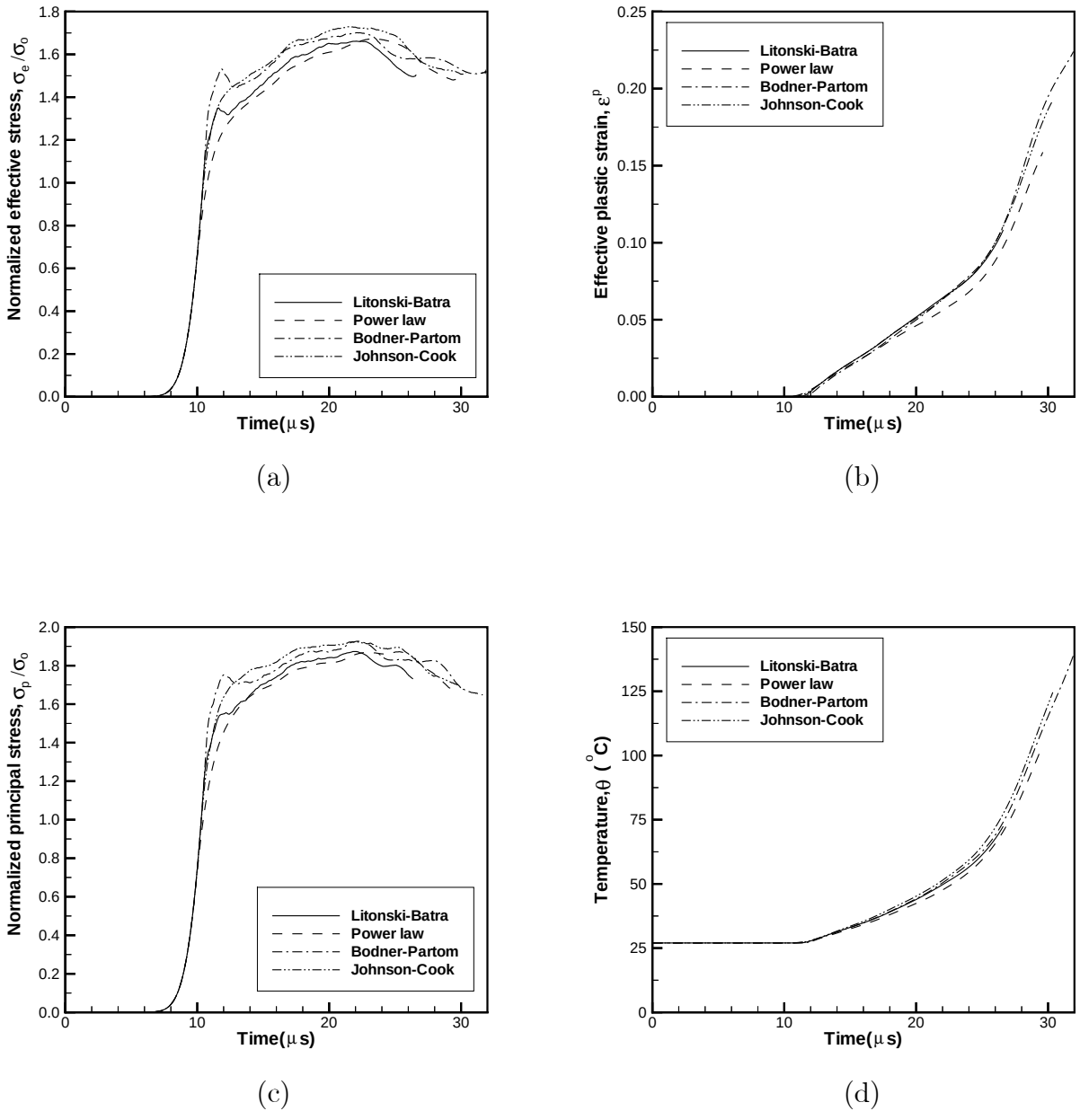

Figure 2.8: For the four thermoviscoplastic relations, time histories at the point P on the notch surface that is located at 45° counterclockwise from the axis of the notch of (a) the normalized effective stress, (b) the effective plastic strain, (c) the normalized maximum principal stress, and (d) the temperature.

lying in the reference configuration within the angular region $-70^\circ \leq \phi \leq -40^\circ$ is intensely deformed. The location and the size of the intensely deformed region is the same for each one of the four constitutive relations but the maximum effective plastic strain induced and the porosity evolved are different.

We note that the deformations of material points close to the surface of the notch tip do not correspond to that of simple shearing. The analytical work of Lee and Freund [63] based on the assumptions of plane strain deformations and linear elasticity shows that the mode mixity equals -0.25 till waves reflected from the unloaded edge of the plate arrive at the notch tip. This suggests that both mode-I and mode-II deformations occur at points near the notch tip. Batra and Ravisankar's [26] numerical simulation of the three-dimensional problem reveals that there is also a noticeable K_{III} component of deformation at points on the front or back surface of the plate that are close to the notch tip surface. Our computed results for the prenotched plate indicate that the four thermoviscoplastic relations studied herein predict different results for mixed mode deformations even though they were calibrated to give very close effective stress vs. effective strain curves in simple shearing. Batra and Chen [11] found that even in simple shearing deformations of a thermoviscoplastic block, these four thermoviscoplastic relations predicted different values of the instability strain, shear band initiation strain, shear band width, and the spacing between adjacent shear bands.

2.6 Failure Mode Transition Speed

In order to determine the speed at which the failure mode changes from brittle to ductile or vice-versa, one needs to define a criterion for the initation of a failure mode. It is generally believed that a brittle failure ensues at a point when the maximum principal tensile stress, σ_p, there attains a critical value. Ritchie et al. [84] have proposed that the brittle failure occurs when $\sigma_p/\sigma_0 = 3.0$ over a certain length which is characteristic of the microstructure of the material and typically equals the grain diameter. Since the stresses are constant over

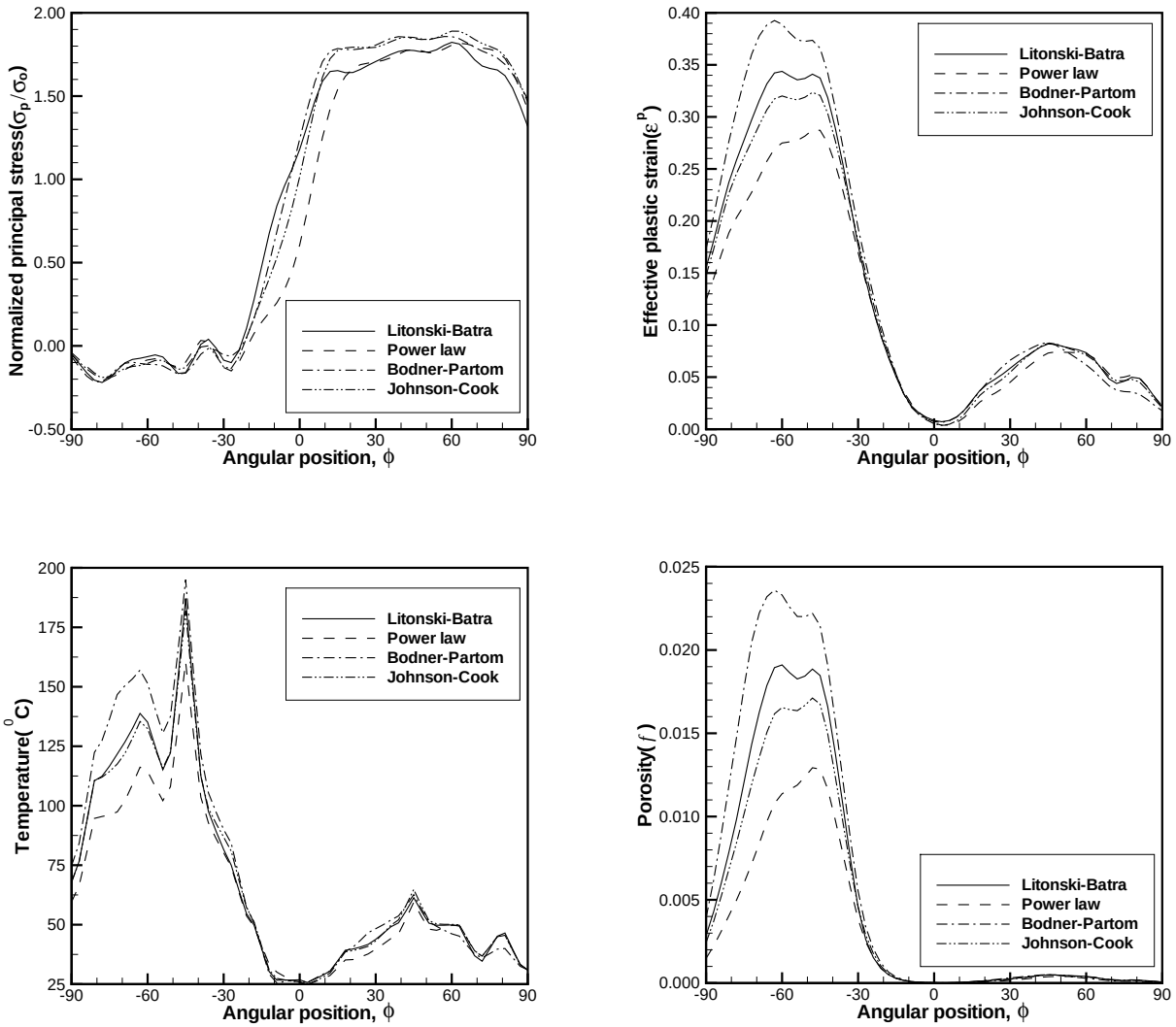

Figure 2.9: At $t = 25\ \mu s$, the angular variation of the normalized maximum principal stress, the effective plastic strain, the temperature and the porosity at the centroids of elements abutting the notch tip surface.

the CST element, the size of the smallest element exceeds $23\mu m$, and the grain diameter is generally less than $23\mu m$, therefore the condition of the principal stress exceeding a critical value over a certain length is easily met. However, tensile experiments of Hendrickson et al. [50] on prenotched steel specimens at nominal stress rates of about 1 to 10^4 MPa/s show that the transition from brittle to ductile failure occurs at $\sigma_p/\sigma_0 \simeq 2.34$; the steel had a yield strength of 705 MPa. This value of σ_p/σ_0 was found to be essentially independent of the temperature and the rate of loading. In their numerical simulation of the Kalthoff experiment, Zhou et al. [109], Batra and Gummalla [12] and Batra and Ravisankar [26] presumed that the brittle failure initiates when $\sigma_p/\sigma_0 = 3.0,\ 2.0$ and 2.0 respectively. For the configurations and impact speeds numerically simulated by Batra and Ravisankar and Zhou et al., no brittle failure initiated at any point in the prenotched plate. Here, based on the test data of Hendrickson et al. [50] we assume that the brittle failure initiates at a material point when $\sigma_p/\sigma_0 = 2.34$ there.

Batra and Kim [15] have numerically studied the initiation and development of shear bands in twelve materials deformed in simple shear. A material defect was modeled by assuming that the thickness of the block varied sinusoidally with the smallest thickness occurring at the block's center. Based on their numerical experiments, Batra and Kim [15] proposed that a shear band initiates at a point when the shear stress there has dropped to 90% of its maximum value and the material point is deforming plastically; this and other works have been summarized by Batra [9]. We recall that in their torsional tests on thin-walled HY-100 steel tubes, Marchand and Duffy [69] regarded the initiation of a shear band as synonymous with the sudden drop in the torque required to twist the tube. They reported the maximum shear strain of 20 within a shear band. Mason et al. [70] measured an effective plastic strain of 1.0 in a shear band formed in a C-300 maraging steel, and Zhou et al. [108] measured the time histories of the temperature at a point on the front surface of a prenotched C-300 maraging steel plate and located about 6-mm ahead of the notch tip. In their numerical simulations of the Kalthoff experiment, Zhou et al. [109] and Batra and Gummalla [12] assumed that a shear band initiates when the effective plastic strain at a point equals a

prespecified value. However, Batra and Ravisankar [26] regarded the shear band to initiate at a point when the effective stress there has dropped to 90% of its maximum value at that point and the material point is deforming plastically. As shown by Batra and Rattazzi [25] the time of initiation of a shear band and the computed shear band speed depend upon the criterion used to characterize the initiation of a shear band. Thus the values of the impact speed given below at which the failure mode transitions from the brittle failure to the ductile failure as signified by the initiation of a shear band depend upon the criteria employed for the initiation of the two failure modes. Our simulations did not include the opening of a crack. Once a crack forms, the domain of study of the problem changes.

For the four thermoviscoplastic relations studied, Fig. 2.10 shows the variation of the time of initiation of the two failure modes with the impact speed. The depicted curves were obtained by the least squares fit of quadratic polynomials to the computed data points. The brittle failure usually initiated at a point situated nearly 0.09 mm from the surface of the notch tip and the line joining it with the center of the notch tip made an angle, in the reference configuration, of about 60° counterclockwise with the axis of the notch. The ductile failure generally originated from a point on the notch surface; the line joining it with the center of the notch tip made an angle, in the reference configuration, of approximately 45° clockwise with the axis of the notch. For a notch tip radius of 0.15 mm, the impact speed, v_0, at which the failure mode transitions from brittle to ductile equals 13.5, 18.5, 19.3 and 22.9 m/s, respectively, for the Litonski-Batra, the power law, the Bodner-Partom and the Johnson-Cook relations. Thus the four thermoviscoplastic relations predict different values of the transition speed.

2.7 Effect of Notch Tip Radius

Having established above that all four thermoviscoplastic relations give qualitatively similar results, we use only the Bodner-Partom relation to investigate the effect of the notch tip

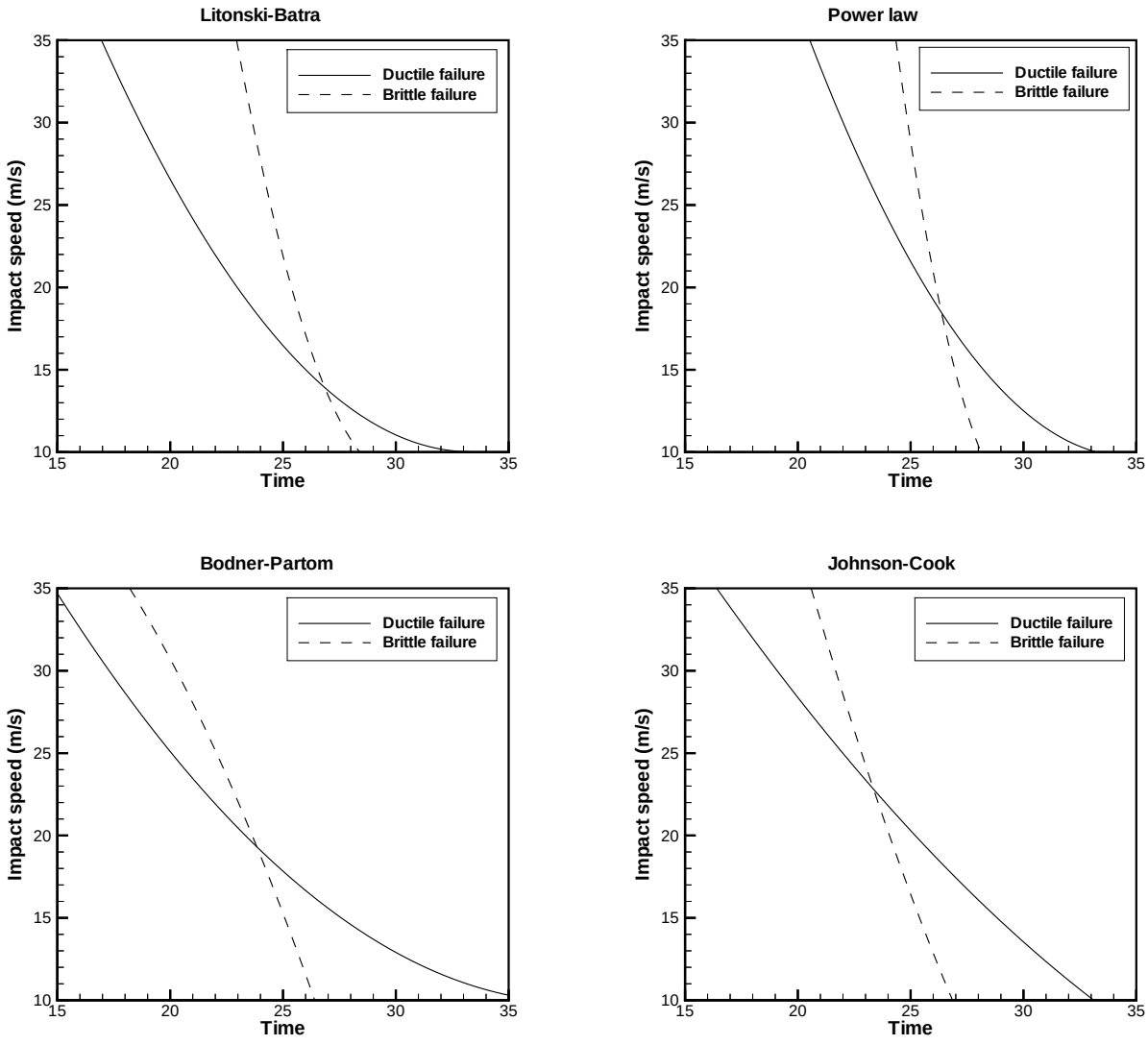

Figure 2.10: For the four thermoviscoplastic relations, the dependence of the times of initiation of the brittle and ductile failures upon the impact speed v_0.

radius on the speed of transition from the brittle failure to the ductile failure. Fig. 2.11 evinces the straight line obtained by the least squares fit to the computed values of $ln\, v_{\rm cr}$ and $ln\, r_0$ for $r_0 = 0.15,\ 0.20$ and $0.25mm$; $v_{\rm cr}$ and r_0 have been normalized by 1 m/s and 1 m respectively. From the values of the slope and the y-intercept, we conclude that for the mild steel being studied

$$v_{\rm cr} = 1179\ r_0^{0.4655}\ \text{m/s}, \tag{2.25}$$

where r_0 is in meters. This compares well with the relation

$$v_{\rm cr} = 1350\ r_0^{0.5}\ \text{m/s}, \tag{2.26}$$

obtained by Kalthoff [56] based on his test findings. We note that Kalthoff tested prenotched plates made of a high strength steel with $r_0 \geq 0.15mm$. For the mild steel plate studied herein and $10 \leq v_0 \leq 35m/s$, no brittle failure was observed for $r_0 = 0.05mm$. Also the computed values of $v_{\rm cr}$ for $r_0 = 0.3mm$ did not satisfy the relation (2.25).

For an impact speed of 25m/s, Fig. 2.12 exhibits the least square fit straight lines to the computed times of initiation of the two failure modes for different values of the notch tip radius, r_0. Results should not be extrapolated outside the range of values of r_0 considered since these curves suggest that for $r_0 = 0.05mm$, brittle failure will ensue but, as stated above, this failure mode did not ensue in our computations. For $0.1 \leq r_0 \leq 0.25mm$, the time of initiation of the two failure modes increases affinely with an increase in the value of r_0, and the ductile failure ensues first. We recall that the opening and consequently propagation of a crack has not been simulated. Once a crack opens due to the initiation of either one of the two failure modes, subsequent deformations of the plate will most likely differ noticeably from those computed here, and the difference in the times of initiation of the two failure modes will not necessarily equal that shown in Fig. 2.12.

For an impact speed of 20 m/s, Figs. 2.13a and 2.13b show the time histories of the effective

stress and the effective plastic strain at a material point located on the notch tip surface and, in the reference configuration, at an angular position of 45° clockwise from the axis of the notch. As expected, the rate of increase of the effective plastic strain is quite high for $r_0 = 0.05$ mm and it decreases with an increase in the value of r_0. For $r_0 = 0.05mm$ the effective stress drops rather precipitously soon after it has reached its peak value; the rate of drop of the effective stress becomes more gradual with an increase in the value of r_0. We assume that $\dot{\varepsilon}^p \; \alpha \; r_0^{\alpha}$ where $\dot{\varepsilon}^p$ is the effective plastic strain rate at the point on the notch tip surface that makes in the reference configuration an angle of 45° clockwise with the axis of the notch. The least squares fit straight lines to the computed values of $ln(\dot{\varepsilon}^p/s^{-1})$ at $t = 10 \; \mu s$ and $ln(r_0/1mm)$ provided $\alpha = -0.93$ for $v_0 = 20m/s$ and $\alpha = -0.812$ for $v_0 = 35m/s$. The order of singularity depends not only upon the impact speed but also on the time when $\dot{\varepsilon}^p$ is measured. For the Johnson-Cook relation, a different steel, and $v_0 \simeq 28m/s$, Batra and Gummalla [12] found from their computed data that $\alpha = -0.31$ and -0.43 at $t = 9$ and $9.5 \; \mu s$ respectively. Batra and Gummalla used a significantly finer mesh consisting of 4-node/rectangular elements than that employed herein; thus their values of $\dot{\varepsilon}^p$ were determined at a point closer to the surface of the notch tip than those found herein. The fringe plots of the effective plastic strain at $t = 25\mu s$ in the region around the notch tip for different values of r_0 are qualitatively similar to each other and are omitted. They reveal that for each value of the notch tip radius, two shear bands emanate from a point on the notch surface - one band is essentially along the axis of the notch and the other is inclined at about 135° clockwise from the notch axis. Figs. 2.13c and 2.13d exhibit at $t = 15\mu s$ the angular variation of the normalized principal stress and the effective plastic strain for the six values of r_0. It is evident that in each case the angular width of the intensely deformed region is approximately the same. Whereas for $r_0 = 0.05$ mm, a shear band initiates at $t = 12.5 \; \mu s$, the time of initiation of a shear band is greater than $15 \; \mu s$ for the other values of r_0. The value of the maximum principal tensile stress at $t = 15 \; \mu s$ is about the same for all values of r_0. Note that the maximum value of the tensile principal stress occurs at a point slightly away from the notch tip surface.

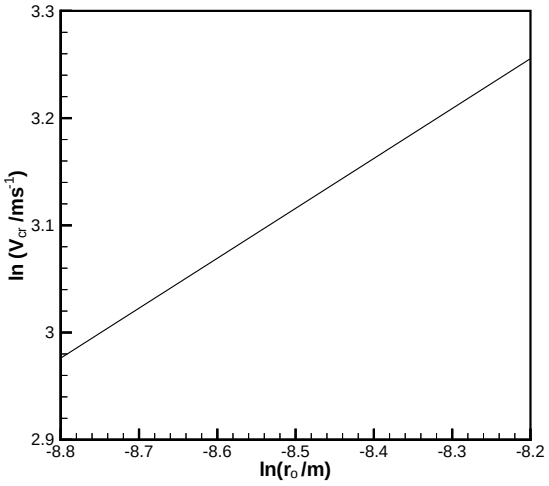

Figure 2.11: Dependence of the transition speed,v_{cr}, upon the notch tip radius, r_0, for a mild steel prenotched plate.

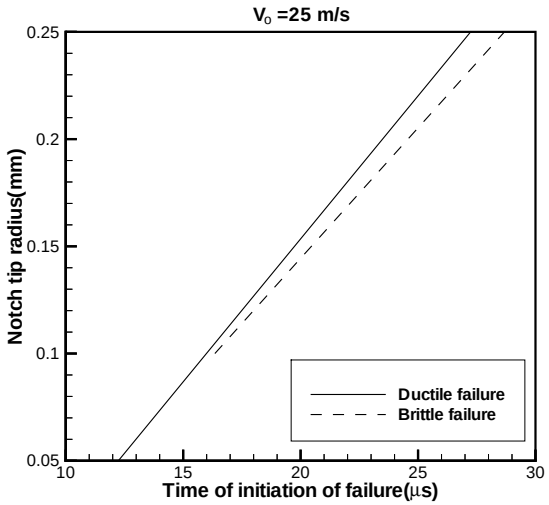

Figure 2.12: Effect of the notch tip radius on the times of initiation of the brittle and the ductile failure.

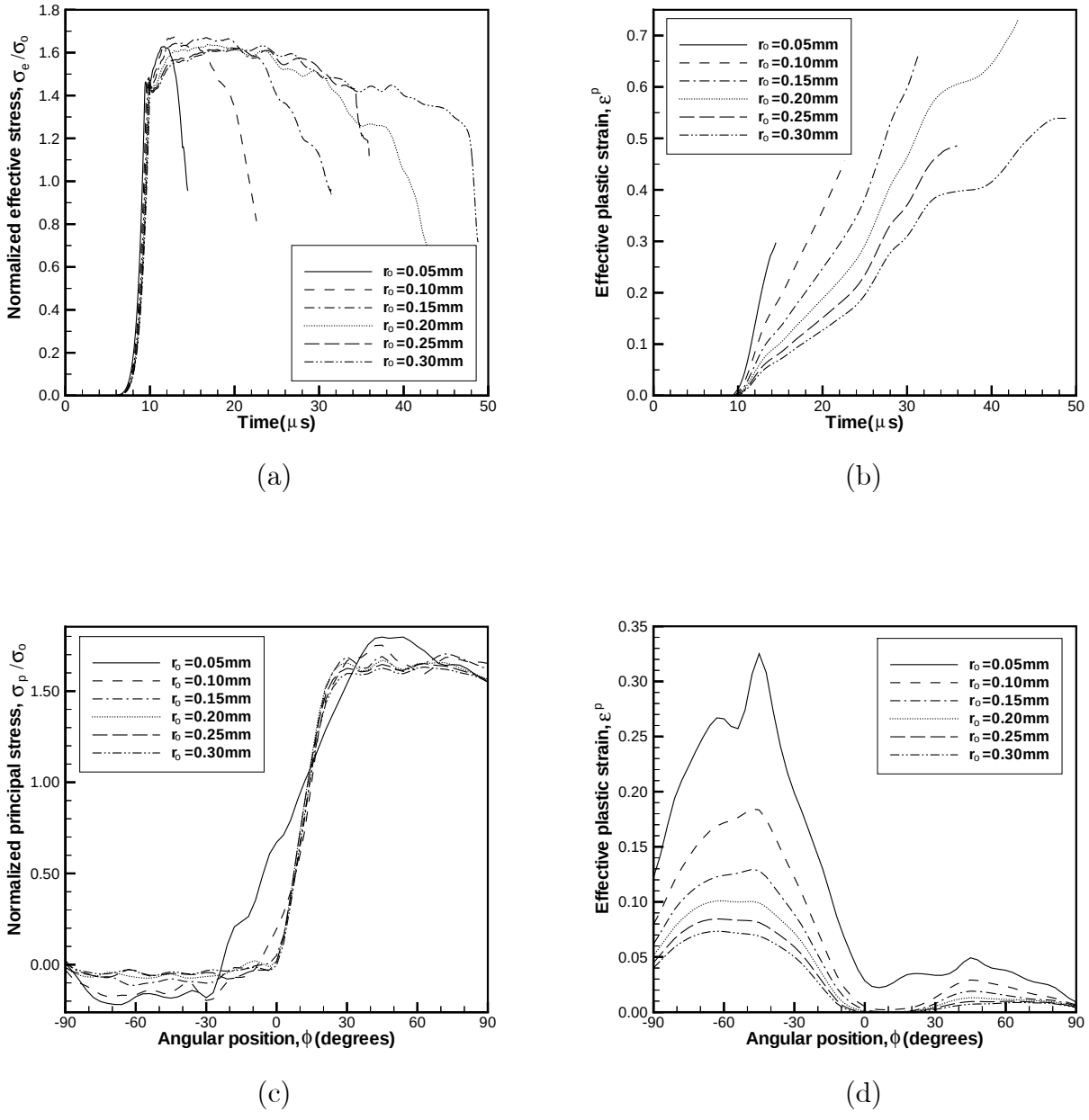

Figure 2.13: For the Bodner-Partom relation, $v_0 = 20m/s$, and for the six values of the notch tip radius, r_0, time histories at the point P of (a) the normalized effective stress, (b) the effective plastic strain, (c) and (d) the angular variation of the normalized maximum principal stress and the effective plastic strain at $t = 15\mu s$.

2.8 Effect of the Material Strength

Shear stress vs. shear strain curves for simple shearing deformations of a homogeneous block plotted in Fig. 3 of Batra and Gummalla's [12] paper clearly indicate that as the quasistatic yield stress, σ_0, of a steel increases the peak in the shear stress occurs at a lower value of the shear strain. This is because in a steel with a higher value of σ_0 more heat is produced for the same value of the effective plastic strain, and the material softens quicker. It suggests that a shear band will form at a lower value of the effective plastic strain as the quasistatic yield stress of the material is increased. This is confirmed by the plot of the time of initiation of a shear band or the ductile failure vs. σ_0 exhibited in Fig. 2.14 for different values of the impact speed; these results are computed with the power law. The reason for switching from the Bonder-Partom relation to the power law is that in the Bodner-Partom relation the dependence of K_1 and K_0 upon σ_0 is not known. We note that for impact speeds in the range of 10 to 20 m/s, the time of initiation of a shear band is essentially unaffected by the value of σ_0, but for a higher impact speed, the time of initiation of a shear band decreases noticeably as σ_0 increases. However, the time of initiation of the brittle failure increases with an increase in the value of σ_0, but the relationship between the two is not monotonic. A similar trend was computed by Batra and Gummalla [12] with the Johnson-Cook relation. Figs. 2.15a and 2.15b depict for $v_0 = 20$ m/s and for different values of σ_0, the time histories of the evolution of the normalized effective stress and the effective plastic strain at the point P. It is evident from these plots that the initial effective plastic strain rate at the point P decreases with an increase in the value of σ_0; results for the material with $\sigma_0 = 0.3\ GPa$ do not follow the pattern of results for other values of σ_0. Batra and Gummalla [12] noticed this too. We have plotted in Figs. 2.15c and 2.15d the angular variation of the normalized principal stress and the effective plastic strain at $t = 25\ \mu s$ computed at the centroids of the elements abutting the surface of the notch tip. Whereas the peak values of the normalized principal stress vary between 1.6 and 1.8, those of the maximum effective plastic strain decrease from 0.29 to 0.14 as σ_0 is increased from 0.5 to 2.1 GPa. The angular position of

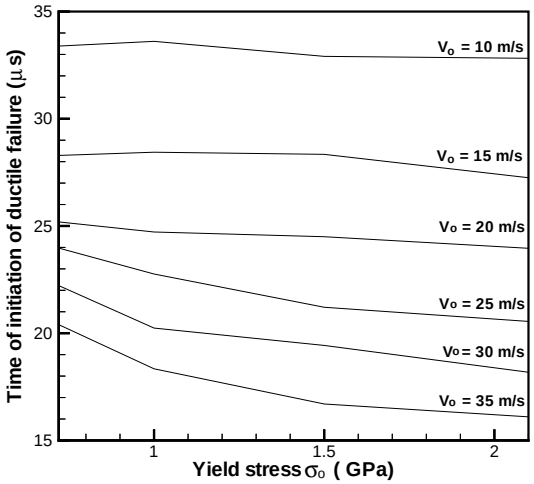

Figure 2.14: For the power law relation, the dependence of the time of initiation of the ductile failure upon the quasistatic yield stress of the material.

the point where these peak values occur is essentially unaffected by the value of σ_0.

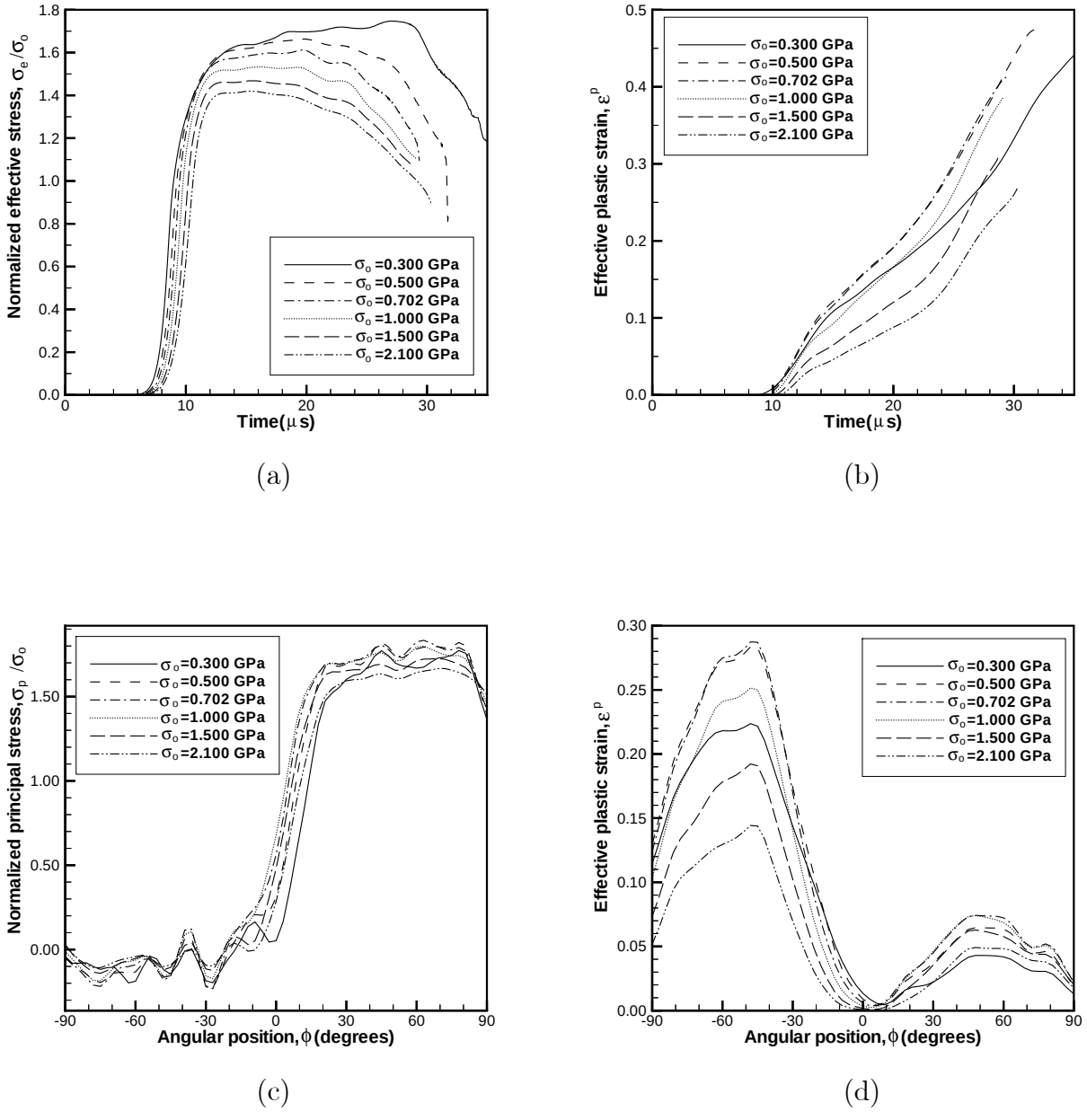

Figure 2.15: For $v_0 = 20\ m/s$, $r_0 = 0.15\ mm$ and different values of σ_0, the time histories of the evolution of (a) the normalized effective stress, and (b) the effective plastic strain at the point P; at $t = 25\mu s$, angular variation of (c) the normalized principal stress, and (d) the effective plastic strain at points abutting the surface of the notch tip.

Chapter 3

Analysis of Failure Modes *

3.1 Introduction

Kalthoff and Winkler [55] and Kalthoff [56] have experimentally studied the transient deformations of a prenotched maraging steel plate with the axes of the two notches parallel to the top and the bottom edges of the plate. The edge between the notches was struck by a cylindrical projectile of diameter equal to the distance between the notches. They found that, with an increase in the impact speed, the failure mode transitioned from a brittle failure in the form of a crack to a ductile failure in the form of an adiabatic shear band. Zhou et al. [108] conducted similar tests and found that only a shear band initiated from the notch-tip, propagated nearly along the axis of the notch and got arrested. They attributed the discrepancy in the observed response of the plate to the difference in the material properties of the two steels. The work described herein shows that the shape of the notch-tip strongly influences the failure mode. For an elliptic notch-tip with the principal axes of lengths $2a$ and $2b$, the failure mode transitions from the brittle to the ductile failure with an increase in the impact speed when $a/b = 0.4$ and 1.0; the principal axis of length $2a$ is along the axis

*The material in this chapter is from the paper " Analysis of Failure Modes in an Impact Loaded Thermoviscoplastic Prenotched Plate" by R. C. Batra, N. A. Jaber and M. E. Malsbury which has been submitted for publication in a refereed journal.

of the notch. However, the ductile failure always precedes the brittle failure for $a/b = 2$ and 10. In the presence of a circular hole of radius r_0 located on the axis of the circular notch-tip of radius r_0 at distances of $3r_0,\ 4r_0,\ 5r_0$ and $6r_0$ from the center of the circular notch-tip, the brittle failure initiated first from a point on the surface of the circular hole. When the horizontal distance between the centers of the hole and the notch tip equalled $4r_0$ and the center of the hole was located either above or below the axis of the notch at distances of r_0 or $3r_0$, both failure modes ensued from points on the surface of the hole in the former case. In the latter configuration, the ductile failure initiated from a point on the notch surface and the brittle failure from a point on the surface of the circular hole.

We note that in the Charpy V-notch test, the ductile failure ensues at low loading rates or at high temperatures and the brittle failure at high loading rates or at low temperatures. Tvergaard and Needleman [95, 96] and Needleman and Tvergaard [77] have numerically analyzed the Charpy and the Kalthoff tests by using Gurson's [46] flow potential and a power law type relation to model the thermoviscoplastic response of a microporous steel. They showed that predictions from the same set of governing equations are in qualitative agreement with the findings of the two tests. The Kalthoff problem has also been numerically studied by Zhou et al. [109], Batra and Nechitailo [23], Batra and Gummalla [12], Batra and Ravisankar [26] and Batra and Jaber [22]. Whereas Batra and Ravisankar [26] analyzed three-dimensional deformations of the prenotched plate and the cylindrical projectile, other investigations studied plane strain deformations of the plate. They employed different constitutive relations but obtained qualitatively similar results. Batra and Jaber [22] used the Johnson-Cook, the Bodner-Partom, the Litonski-Batra and a power law type relation to model the thermoviscoplastic response of the plate. They determined the values of material parameters by solving initial-boundary-value problems simulating the same simple shear test and used these to study thermomechanical deformations of the plate. They showed that results for the Kalthoff problem computed with the four constitutive relations agreed qualitatively but the failure mode transition speed depended upon the constitutive relation employed. Here we use the Bondner-Partom [29] relation to model the thermoviscoplastic

response of the plate.

3.2 Formulation of the Problem

A schematic sketch of the problem studied is shown in Figs. 3.1 and 3.2 . We neglect the effect of body forces and the sources, if any, of the internal energy. We use rectangular Cartesian coordinates to study transient thermomechanical deformations of the prenotched plate. These deformations are governed by the following balance laws of mass, linear momentum, moment of momentum and internal energy written in the referential description of motion.

$$(\rho J(1-f))^{\cdot} = 0, \tag{3.1}$$

$$\rho_0(1-f_0)\dot{\mathbf{v}}_i = T_{i\alpha,\alpha}, \tag{3.2}$$

$$T_{i\alpha}x_{i,\beta} = T_{i\beta}x_{i,\alpha}, \tag{3.3}$$

$$\rho_0(1-f_0)\dot{e} = -Q_{\alpha,\alpha} + T_{i\alpha}\dot{x}_{i,\alpha}. \tag{3.4}$$

Here ρ is the present mass density of a material point whose mass density in the reference configuration is ρ_0, f the present porosity, a superimposed dot indicates the material time derivative, $\mathbf{v}$ the velocity, $\mathbf{T}$ the first Piola-Kirchhoff stress tensor, $\mathbf{x}$ the present position of the material particle that occupied the place $\mathbf{X}$ in the reference configuration, $x_{i,\beta} \equiv \partial x_i/\partial X_\beta$, $J = det[x_{i,\alpha}]$, a repeated index implies summation over the range of the index, e is the specific internal energy, and $\mathbf{Q}$ the heat flux per unit reference area.

The plate is assumed to be made of a homogeneous and isotropic material, and its thermo-

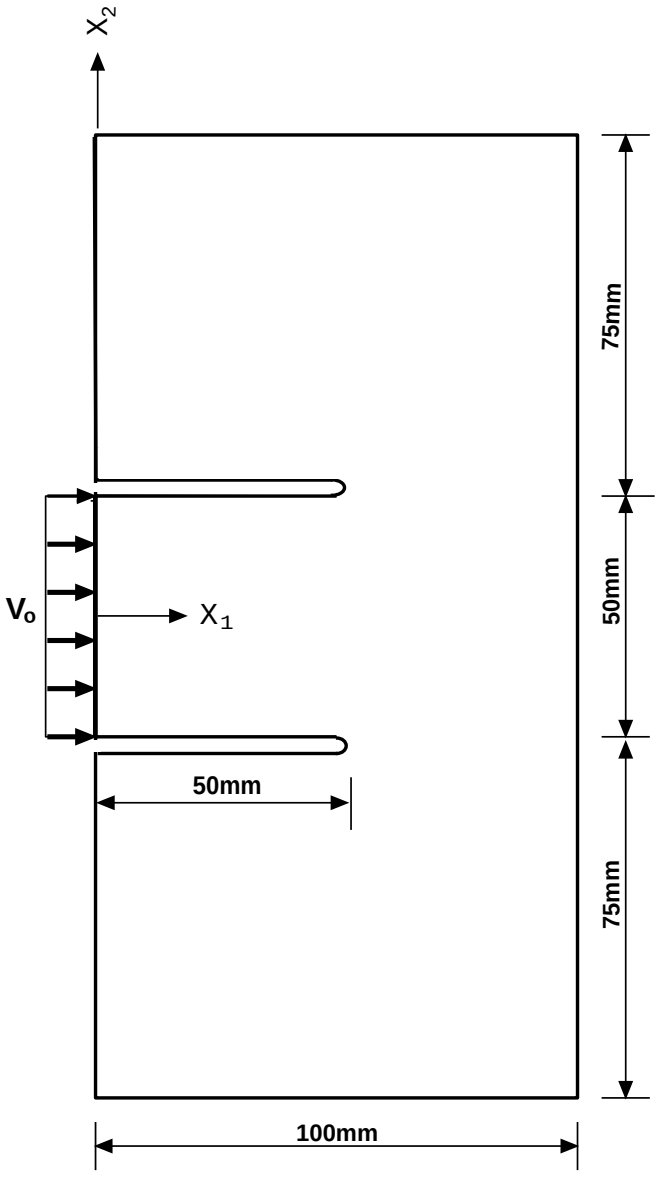

Figure 3.1: A schematic sketch of the problems studied.

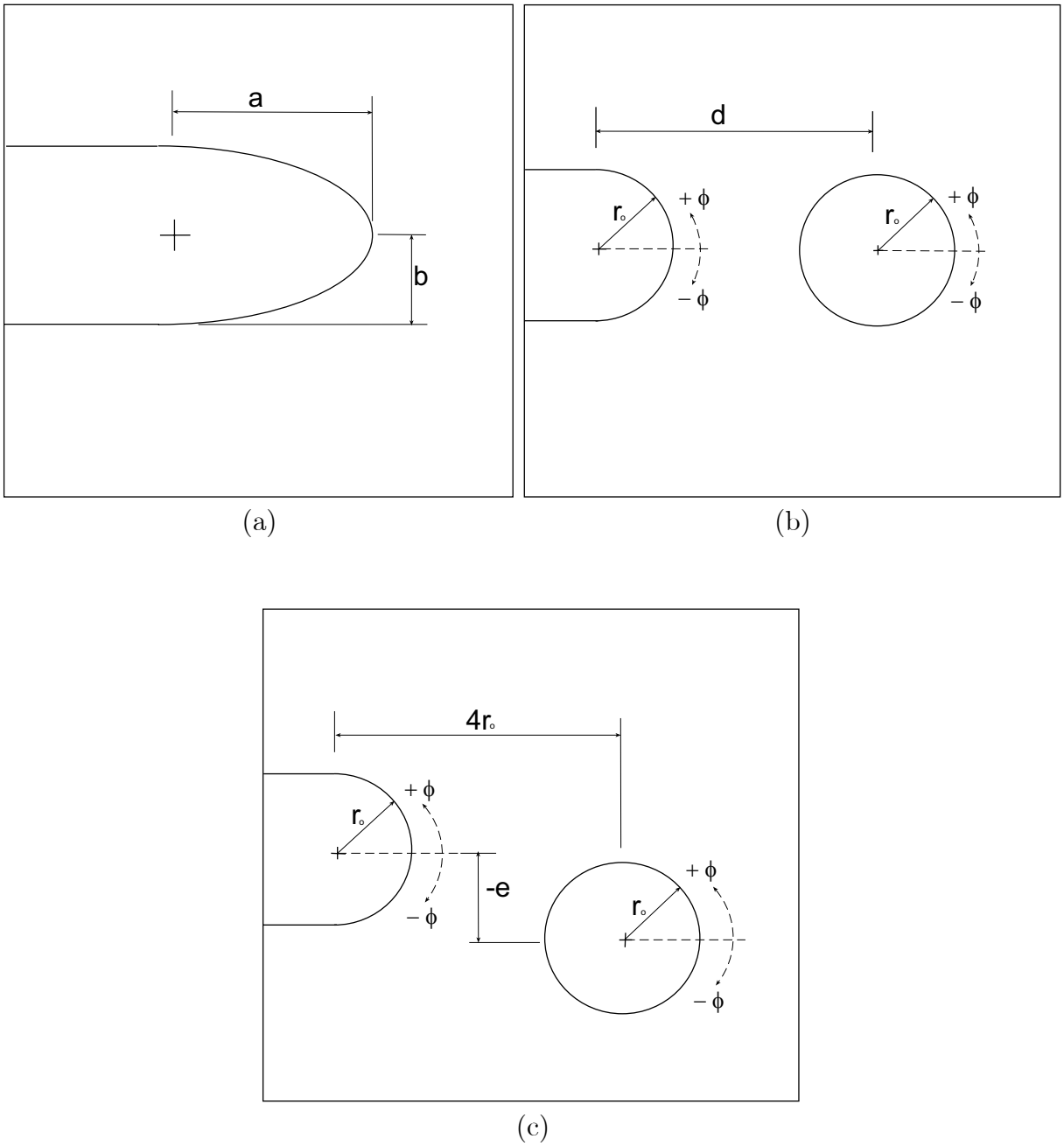

Figure 3.2: A schematic sketch of the problems studied (a) an ellipsoidal notch-tip; (b) a view of a circular notch-tip and a circular hole located directly ahead of the notch; (c) a view of a circular notch-tip and a circular hole located away from the axis of the notch.

mechanical response modeled by the following constitutive relations.

$$\dot{\sigma}_{ij} - \Omega_{ik}\sigma_{kj} + \sigma_{ik}\Omega_{kj} = \frac{E(1-f)}{(1+\nu)}D^e_{ij} + \frac{\nu E(1-f)}{(1+\nu)(1-2\nu)}D^e_{kk}\delta_{ij}, \tag{3.5}$$

$$D_{ij} = D^e_{ij} + D^p_{ij} + \alpha\dot{\theta}\delta_{ij},\ D_{ij} = (v_{i,j} + v_{j,i})/2,\ \Omega_{ij} = (v_{i,j} - v_{j,i})/2, \tag{3.6}$$

$$D^p_{ij} = \frac{(1-f)\sigma_e\dot{\varepsilon}^p}{\sigma_{kl}N_{kl}}N_{ij},\ N_{ij} = \frac{\partial\Phi}{\partial\sigma_{ij}}, \tag{3.7}$$

$$\Phi \equiv \frac{3}{2}\frac{(s_{ij}s_{ij})}{\sigma_e^2} + 2f^*q_1\cosh\left(\frac{q_2\sigma_{kk}}{2\sigma_e}\right) - 1 - q_1^2f^{*^2} = 0, \tag{3.8}$$

$$s_{ij} = \sigma_{ij} - \frac{1}{3}\sigma_{kk}\delta_{ij}, \tag{3.9}$$

$$\dot{\varepsilon}^p = D_0\exp\left[-\frac{1}{2}\left(\frac{K^2}{3\sigma_e^2}\right)^n\right],\ \sigma_e = \left(\frac{3}{2}\sigma_{ij}\sigma_{ij}\right)^{1/2}, \tag{3.10}$$

$$K = K_1 - (K_1 - K_0)\exp(-mW_p),\ n = \frac{A}{\theta} + B,\ W_p = \int_0^t \sigma_{ij}D^p_{ij}dt, \tag{3.11}$$

$$f^* = \begin{cases} f \text{ if } f \le f_c, \\ f_c + \left(\dfrac{f_u - f_c}{f_f - f_c}\right)(f - f_c),\ \text{if } f > f_c, \end{cases} \tag{3.12}$$

$$\dot{f} = (1-f)D^p_{ii} + \frac{f_2\dot{\varepsilon}^p}{s_2\sqrt{2\pi}}\exp\left(-\frac{1}{2}\left(\frac{\varepsilon^p - e_N}{s_2}\right)^2\right), \tag{3.13}$$

$$Q_\alpha = -\kappa\left(1 - \frac{3}{2}f\right)\theta_{,\alpha}, \tag{3.14}$$

$$\dot{e} = c\dot{\theta} + \sigma_{ij}D^e_{ij} + \alpha\dot{\theta}\sigma_{kk}, \tag{3.15}$$

$$T_{i\alpha} = J\sigma_{ij}X_{\alpha,j}. \tag{3.16}$$

Here $\boldsymbol{\sigma}$ is the Cauchy stress tensor related to the first Piola-Kirchhoff stress tensor by (3.16), $\boldsymbol{\Omega}$ the spin tensor, E Young's modulus, ν Poisson's ratio, α the coefficient of thermal expansion, $\mathbf{D}$ the strain-rate tensor, $\dot{\varepsilon}^p$ the effective plastic strain-rate, κ the thermal conductivity, and c the specific heat. Other parameters characterizing the material are $q_1,\ q_2,\ f_2,\ s_2,\ e_N,\ f_c,\ f_u,\ D_0,\ K_1,\ K_0,\ m,\ A$, and B. The left-hand side of equation (3.5) is the Jaumann derivative of the Cauchy stress, Φ is the Gurson's [46] flow potential for

a microporous isotropic material as modified by Tvergaard and Needleman [94], equation $(3.10)_1$ is the Bodner-Partom [29] relation used here to characterize the thermomechanical deformations of the material, and equation (3.14) is the Fourier law of heat conduction in which the thermal conductivity is taken to decrease affinely with an increase in the porosity, e.g., see Budiansky [31]. The affine degradation of the Young's and the bulk moduli with an increase in the porosity has been proposed, amongst others, by Passman and Batra [80] and Kobayashi and Dodd [59]. Equation (3.13) for the evolution of the porosity is taken from Chu and Needleman's [35] work; we have not considered the stress controlled nucleation of voids.

For the initial conditions we take

$$\boldsymbol{\sigma}(\mathbf{x},0)=\mathbf{0},\ f(\mathbf{x},0)=0,\ \rho(\mathbf{x},0)=\rho_0,\ \mathbf{v}(\mathbf{x},0)=\mathbf{0},\ \theta(\mathbf{x},0)=\theta_0.$$

That is, the plate is initially at rest, stress free and at a uniform temperature θ_0. The following boundary conditions are imposed on the surface of the plate impacted by the cylindrical rod.

$$v_1/v_0=\begin{cases}0.3t, & 0\le t\le 2\mu s,\\ 0.525+0.0375t, & 2\le t\le 10\mu s,\\ 0.9, & 10\mu s\le t\le t_s,\\ 0, & t>t_s,\end{cases} \tag{3.17}$$

$$T_{21}=0,\ Q_1=0.$$

Here v_0 is the speed of the projectile, v_1 the velocity of plate particles in the x_1-direction, and t_s equals the time when the projectile separates from the plate. This expression for v_1 is obtained by fitting straight lines to the data of Batra and Ravisankar [26] who studied three-dimensional deformations of the plate and the projectile. Equations $(3.17)_2$ and $(3.17)_3$ imply that the contact surface is smooth and thermally insulated. All remaining bounding surfaces of the plate including those of the notch and the circular hole if there is one are

assumed to be traction free and thermally insulated.

3.3 Computation and Discussion of Results

We assume that the material of the plate is HY100 steel, and assign following values to various material and geometric parameters.

$$\begin{aligned}
&\sigma_0 = 702 \text{ MPa},\ \rho_0 = 7860 \text{ kg/m}^3,\ c = 473 \text{ J/kg}\,^\circ C,\ \kappa = 49.73 \text{ W/m}^2\,^\circ C,\\
&\alpha = 11.5 \times 10^{-6}/^\circ C,\ E = 208 \text{ GPa},\ \nu = 0.3,\ f_2 = 0.04,\ e_N = 0.3,\\
&s_2 = 0.1,\ q_1 = 1.5,\ q_2 = 1.0,\ f_c = 0.15,\ f_f = 0.25,\ f_u = 0.667,\ f_0 = 0,\\
&\theta_o = 25^\circ C,\ A = 1200 \text{ K},\ B = 0,\ K_1 = 2950 \text{ MPa},\ K_0 = 2937 \text{ MPa},\\
&m = 3510/\text{MPa},\ D_0 = 1.732 \times 10^8/s,\ v_0 = 30 \text{ m/s}.
\end{aligned} \tag{3.18}$$

Values of $A,\ B,\ K_1,\ K_0,\ m,\ D_0$ and σ_0 were obtained by finding the numerical solution of the initial-boundary-value problem closely simulating the torsional test conditions of Marchand and Duffy [69] and comparing the computed shear stress-shear strain curve with the experimental one; e.g. see Batra and Kim [16]. Values of all of the thermophysical material parameters are likely to depend upon the temperature; such dependencies have been ignored here for the sake of simplicity.

The three-dimensional analysis of the problem by Batra and Ravisankar [26] revealed that deformations of the central 75% of the thickness of the plate closely correspond to the plane strain state of deformations. Here we presume that a plane strain state of deformation prevails in the plate. Because of the symmetry of the problem about the horizontal centroidal axis, we study deformations of only the upper half of the plate.

The aforestated problem is solved numerically by using an in-house developed finite element code. It employs constant strain triangular (CST) elements, lumped mass matrix derived

by the row sum technique, and the subroutine LSODE (Livermore Solver for Ordinary Differential Equations) for integrating the stiff set of coupled nonlinear ordinary differential equations (ODEs). The Galerkin approximation of equation (3.2) and that obtained by substituting from (3.14)-(3.16) and (3.5)-(3.7) into (3.4) yields the ODEs for the determination of the nodal values of $v_1,\ v_2$ and θ. Equations (3.1), (3.5), (3.10) and (3.13) are integrated at the centroids of the elements. Thus the number of ODEs to be integrated equals 3 (nodes) + 7 (elements). A reasonably fine mesh was employed in the region around the notch-tip and the hole, and a coarse mesh elsewhere; see Fig. 4.2. Results presented herein have been computed with a fixed mesh.

Ritchie et al.[84] have proposed that a brittle failure ensues when $\sigma_p/\sigma_0 = 3.0$ over a certain length that is characteristic of the microstructure of the material and typically equals the grain diameter; σ_p equals the maximum principal tensile stress. The size of the smallest CST element used here equals 23 μm, the stresses are constant over an element, and the grain diameter is usually smaller than 23 μm, thus the condition of the principal tensile stress exceeding a critical value is easily met. Based on the test data of Hendrickson et al. [50] for tensile experiments on prenotched steel (yield strength = 705 MPa) specimens at nominal stress rates of approximately 1 to 10^4 MPa/s, we assume that a brittle failure initiates at the centroid of an element when $\sigma_p/\sigma_0 = 2.34$ there. Based on numerical experiments on the initiation and the development of adiabatic shear bands (ASBs), Batra and Kim [15] proposed that an ASB initiates at a point when the shear stress there has dropped to 90% of its maximum value and the material point is deforming plastically; these and other numerical tests are summarized in Batra [9]. We take the initiation of the ductile failure as synonymous with the ensuing of an ASB and replace the shear stress by the effective stress. We emphasize that the computed failure mode transition speed will depend upon the criteria adopted for the initiation of the two failure modes. Our simulations neither included the opening of a crack nor the erosion of a failed element.

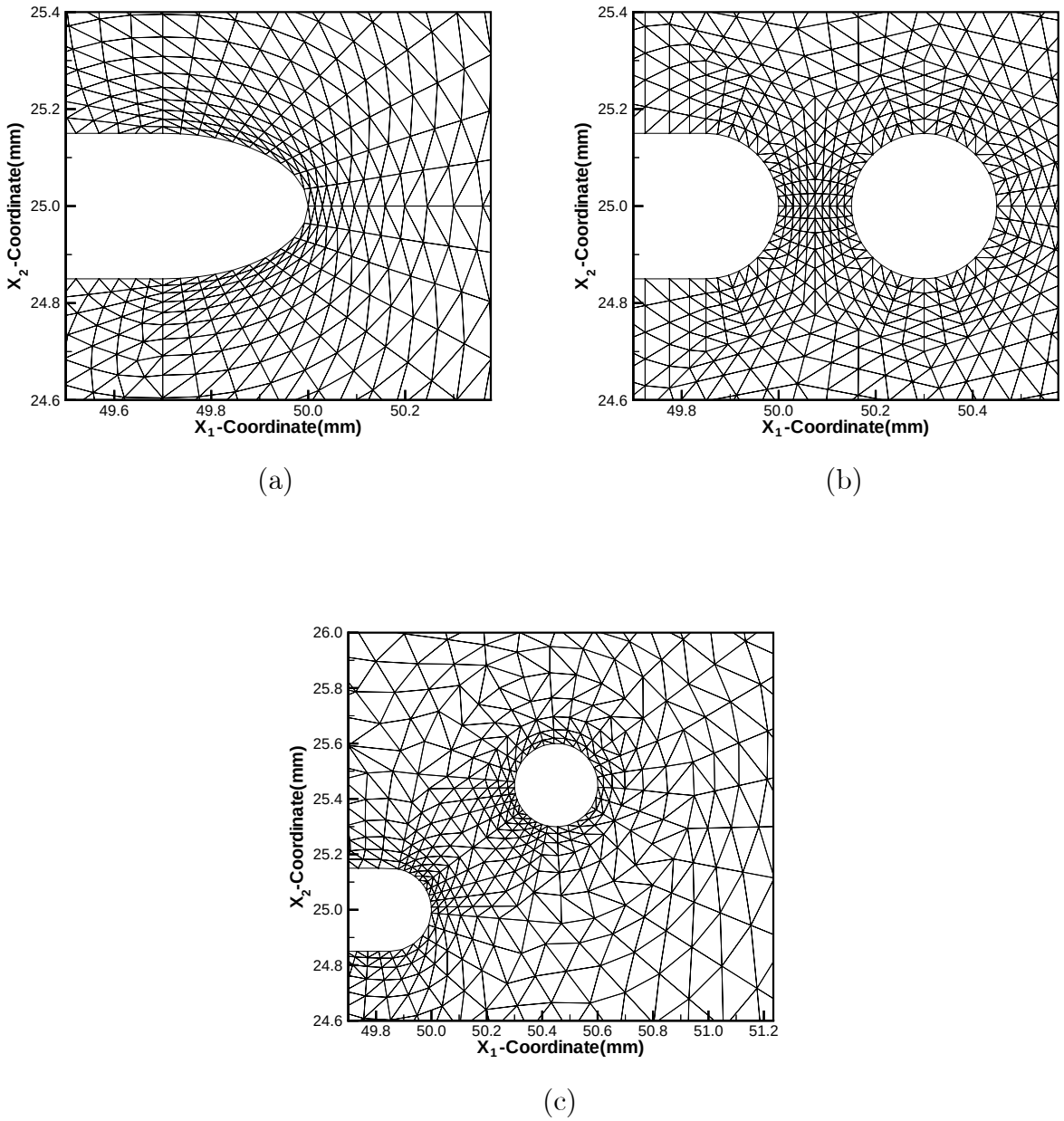

Figure 3.3: A finite element discretization of the small region around the notch-tip and the circular hole for the three types of problems studied.

3.4 Effect of the Shape of the Notch-tip

In linear elastic fracture mechanics a sharp notch with essentially zero radius is considered. However, in experimental fracture mechanics, a sharp notch of zero radius is nearly impossible to achieve. We note that Kalthoff [54, 56] examined deformations of prenotched plates with circular notch-tips of radii exceeding 0.15 mm, and the radius of the circular notch-tip equalled 0.15 mm in the prenotched plates studied by Zhou et al. [108, 109]. Here we consider elliptic notch-tips with principal axes of lengths $2a$ and $2b$ respectively; $b = 0.15$ mm for all problems studied, and the principal axis of length $2a$ is along the axis of the notch. A sharp notch is simulated by setting $a/b = 10.0$ and a blunt one by taking $a/b = 0.4$. Thermomechanical deformations of a prenotched plate with $a/b = 0.2$ could not be studied for $t > 10\mu$s because of the severe concentrations of the deformations near the top and the bottom corners of the notch-tip. Unless otherwise stated, results presented and discussed below are for an impact speed of 30 m/s. For notch-tips with $a/b = 0.4,\ 1.0,\ 2.0$ and 10.0 we have plotted in Figs. 3.4, 3.5 and 3.6 the fringes of the effective plastic strain, the normalized shear stress σ_{12} and the non-dimensional maximum principal stress in a small region surrounding the notch-tip. In each case results are plotted at the instant of the initiation of the ductile failure which is the same as the time when the ASB initiates. The times of initiation of the ASB equal 12.30, 17, 16 and 13.20 μs for $a/b = 0.4,\ 1.0,\ 2.0$ and 10.0 respectively. Note that the time is reckoned from the instant of impact. It is clear that a deviation of the shape of the notch-tip away from the circular one results in an earlier initiation of the ASB in the impact loaded prenotched plate. For each notch-tip shape, the ASB initiates from a point on the surface of the notch-tip that is closer to the impacted edge. In the deformed configuration the angle measured clockwise between the axis of the notch-tip and the line joining its center to the point where the ASB initiates equals 85°, 45°, 12° and 3° respectively for $a/b = 0.4,\ 1.0,\ 2.0$ and 10.0. Thus, with an increase in the value of a/b, the point of initiation of the ductile failure shifts toward the center of the notch-tip. At the instant and the location of the initiation of the ASB, the temperature rise, the effective

plastic strain and the effective plastic strain-rate equal (158°C, 0.365, $1.8 \times 10^5/s$), (157°C, 0.378, $0.42 \times 10^5/s$), (122°C, 0.293, $0.4 \times 10^5/s$) and (82°C, 0.175, $0.5 \times 10^5/s$) respectively for $a/b = 0.4$, 1.0, 2.0 and 10.0. A typical value of the porosity at these four points equals 0.002 at the instant of the initiation of the ASB. The maximum strain induced nucleation rate of voids when the ASB initiates equals (cf. eqn. (3.13)) 8,000/s and is smaller at other times. Since the computations were ceased once an element got severely deformed which occurred soon after the initiation of the ASB, there was not enough time in our computations for the porosity to evolve noticeably. For each value of a/b, the region with relatively large values of the effective plastic strain has two lobes; one essentially parallel to the axis of the notch and the other inclined at approximately 130° clockwise from the axis of the notch. However, for each one of the four values of a/b considered, the narrow region of the maximum value of $|\sigma_{12}|$ is essentially parallel to the axis of the notch. It suggests that a shear band propagating along the axis of the notch is more intense than the other one. Fringe plots of the normalized maximum principal stress indicate that for each value of a/b the maximum principal tensile stress occurs at a point situated a little away from the upper surface of the notch-tip. For each one of the four notch tips, the maximum principal stress is compressive in the region enclosing the point of initiation of the ductile failure. We note that the results are qualitatively similar for the four notch tips.

Figure 4.4 shows the deformed shapes of the four notch-tips and the locations in the deformed configurations of the points from where the brittle and the ductile failures initiate. Because of the Poisson effect, the lower surface of the notch moves upwards. Note that the upper surface is displaced very little. Also points on the lower surface of the notch move to the right, i.e., in the direction of impact thereby inducing tensile circumferential strains in the upper part of the notch surface. The two points where the brittle and the ductile failures initiate move towards the axis of the notch-tip with an increase in the value of a/b.

Figures 4.5a and 4.5b exhibit the angular variation, at the time of initiation of the brittle failure, of the effective plastic strain and the normalized maximum principal stress at the centroids of elements abutting the surface of the notch-tip. Recall that the maximum prin-

cipal tensile stress occurs at a point slightly away from the surface of the notch-tip. For an impact speed of 30 m/s, the ductile failure precedes the brittle failure for the four shapes of the notch tip. The angular positions in Figs. 4.5a and 4.5b are in the reference configuration. Out of the four values of a/b studied, values of the maximum effective plastic strain for $a/b = 0.4$ and 1.0 are considerably higher than those for $a/b = 2.0$ and 10.0; however, the angular width of the intensely deformed region wherein the effective plastic strain equals at least 90% of the maximum value is smaller for $a/b = 0.4$ than that for the other three cases. Because of the elliptic shape of the notch tip, the angular width is not proportional to the arc length for the four shapes of the notch tip. For $a/b = 1.0$ and 2.0, the point-to-point variations in the values of the maximum principal stress are very small except near the notch tip where it changes from compressive at points on the lower surface of the notch tip to tensile at points on the upper surface of the notch tip.

Figure 4.6a illustrates the time history of the evolution of the effective plastic strain at the point where the ductile failure occurs. The rate of increase of the effective plastic strain or equivalently the effective plastic strain-rate has the highest value for $a/b = 0.4$. Approximate values of the effective plastic strain-rate at these four points soon after the loading wave arrives at the notch-tip equal 1.0×10^5, 6×10^4, 1.5×10^4 and $1 \times 10^4/s$ respectively for $a/b = 0.4,\ 1.0,\ 2.0$ and 10.0. Thus typical peak values of the effective plastic strain rate are in the range of 10^4 to $10^5/s$ for the four values of a/b, and the lower value of the effective plastic strain rate occurs for a larger value of a/b. The time history of the evolution of the maximum principal tensile stress at the point where the brittle failure ensues is shown in Fig. 4.6b. The angular locations, in the deformed configuration and measured counter-clockwise, of these points are 80°, 50°, 30° and 15° respectively for $a/b = 0.4,\ 1.0,\ 2.0$ and 10.0.

From the plots given in Fig. 4.7 of the impact speed vs. the times of initiation of the brittle and the ductile failures, the impact speeds at which the failure mode transitions from the brittle to the ductile are found to be 19.0 and 19.3 m/s respectively for $a/b = 0.4$ and 1.0; for $a/b = 2.0$ and 10.0, the ductile failure preceded the brittle failure for all impact speeds considered herein. It suggests that out of the four notch shapes scrutinized, the failure

mode transition occurs only for elliptic notches with $a/b = 0.4$ and 1.0. It may provide an explanation for the differences in the test observations of Kalthoff and Zhou et al. who seem to have tested prenotched plates made of very similar materials. Because of the different techniques used to cut notches, the shapes of the notch-tips may not have been identical in the specimens used in the two laboratories. Whereas the time of initiation of the ductile failure for a circular notch-tip decreases noticeably from 27 μs at $v_0 = 15$ m/s to 15 μs for $v_0 = 35$ m/s, it decreases from 15 μs at $v_0 = 15$ m/s to 13 μs at $v_0 = 35$ m/s for an elliptic notch tip with $a/b = 10$. For a very blunt notch tip with $a/b = 0.4$, the two failure modes initiate almost simultaneously, but that is not the case for $a/b = 1.0,\ 2.0$ and 10.0. For each one of the four values of a/b, the times of initiation of both the brittle and the ductile failures decrease with an increase in the impact speed; the slopes of these curves strongly depend upon the value of a/b.

3.5 Effect of a Circular Hole in Front of a Circular Notch-tip

We now investigate the effect on the thermomechanical deformations of the prenotched plate of a circular hole of radius $r_0 = b$ situated ahead of the circular notch tip of radius $r_0 = 0.15$ mm. We first consider the case when the center of the circular hole is on the axis of the notch with the distance between the centers of the circular hole and the circular notch tip equal to d, and subsequently when the center of the hole is at a distance e from the axis of the notch. The two configurations are depicted in Figs. 1b and 1c respectively.

3.5.1 Circular Hole Located on the Axis of the Notch

Figure 3.11 shows the dependence of the times of initiation of the brittle and the ductile failures upon the impact speed for $d/r_0 = 3,\ 4,\ 5$ and 6. In each case the brittle failure

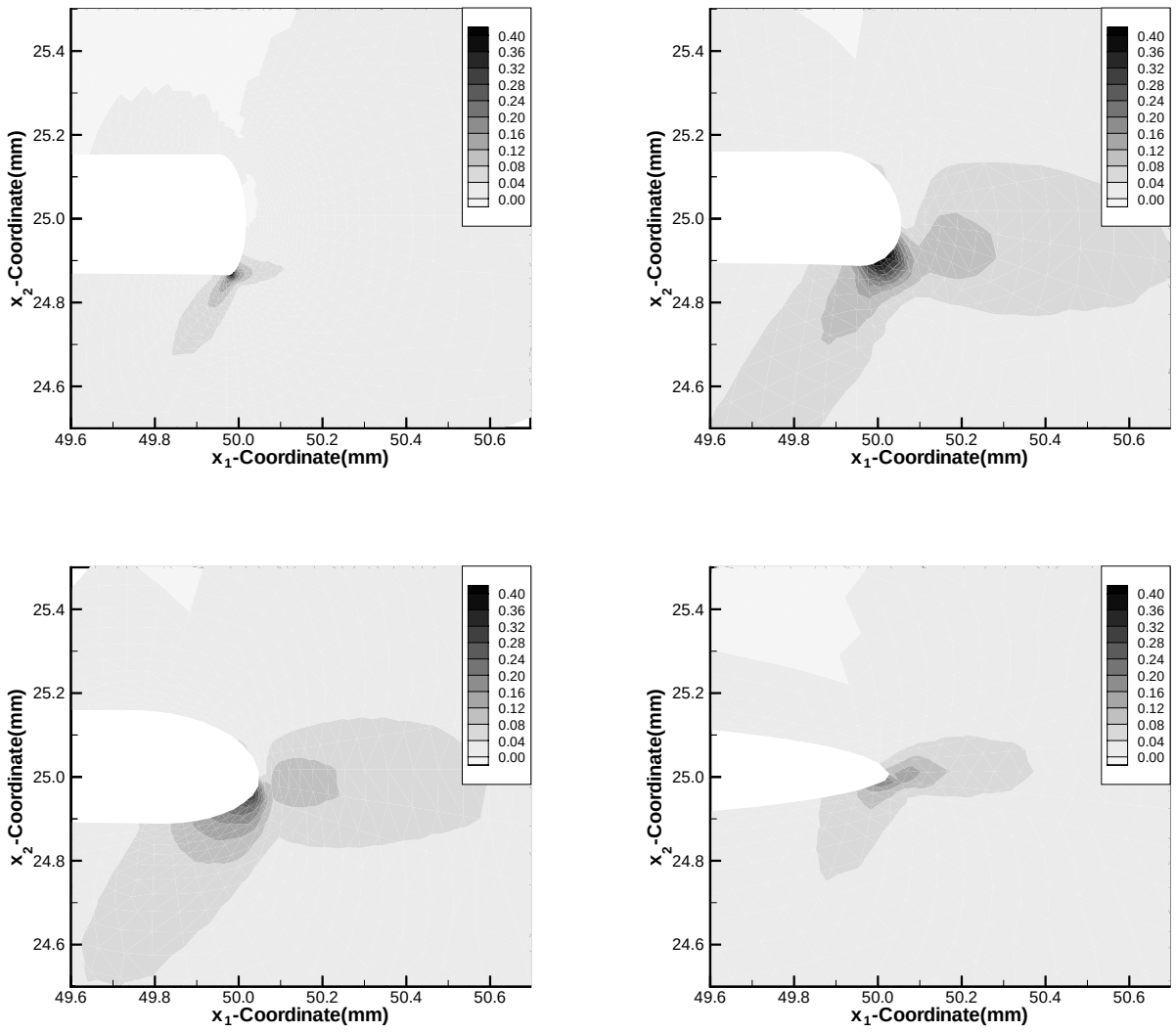

Figure 3.4: For the four elliptic notch-tips and the impact speed of 30m/s, fringe plots of the effective plastic strain in a small region surrounding the surface of the notch-tip. The times at which results are plotted equal respectively 12.3, 17, 16 and 13.3 μs for $a/b = 0.4$, 1.0, 2.0 and 10.0.

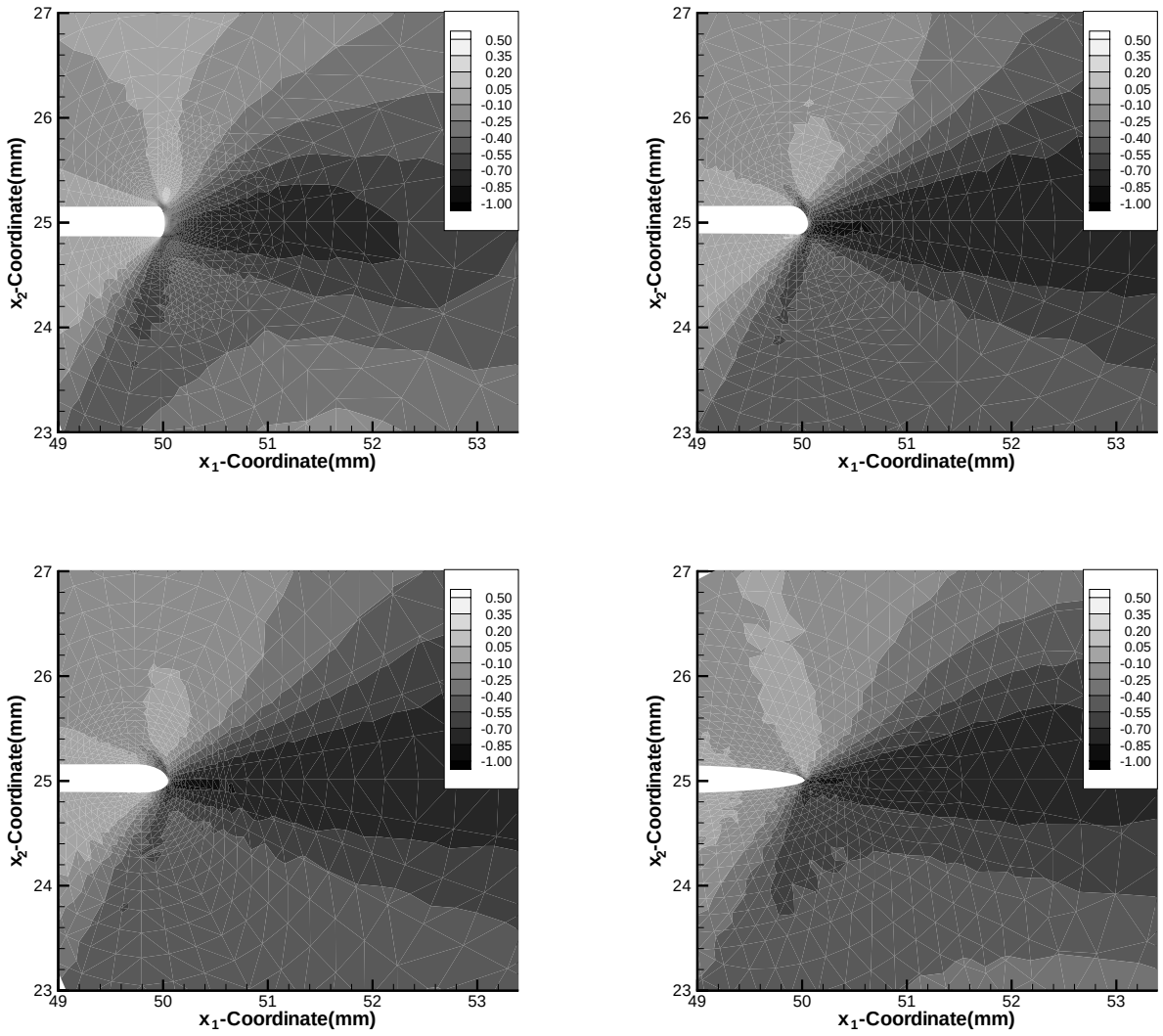

Figure 3.5: For the four elliptic notch-tips and the impact speed of 30m/s, fringe plots of the normalized shear stress σ_{12} in a small region surrounding the surface of the notch-tip. The times at which results are plotted equal respectively 12.3, 17, 16 and 13.3 μs for $a/b = 0.4$, 1.0, 2.0 and 10.0.

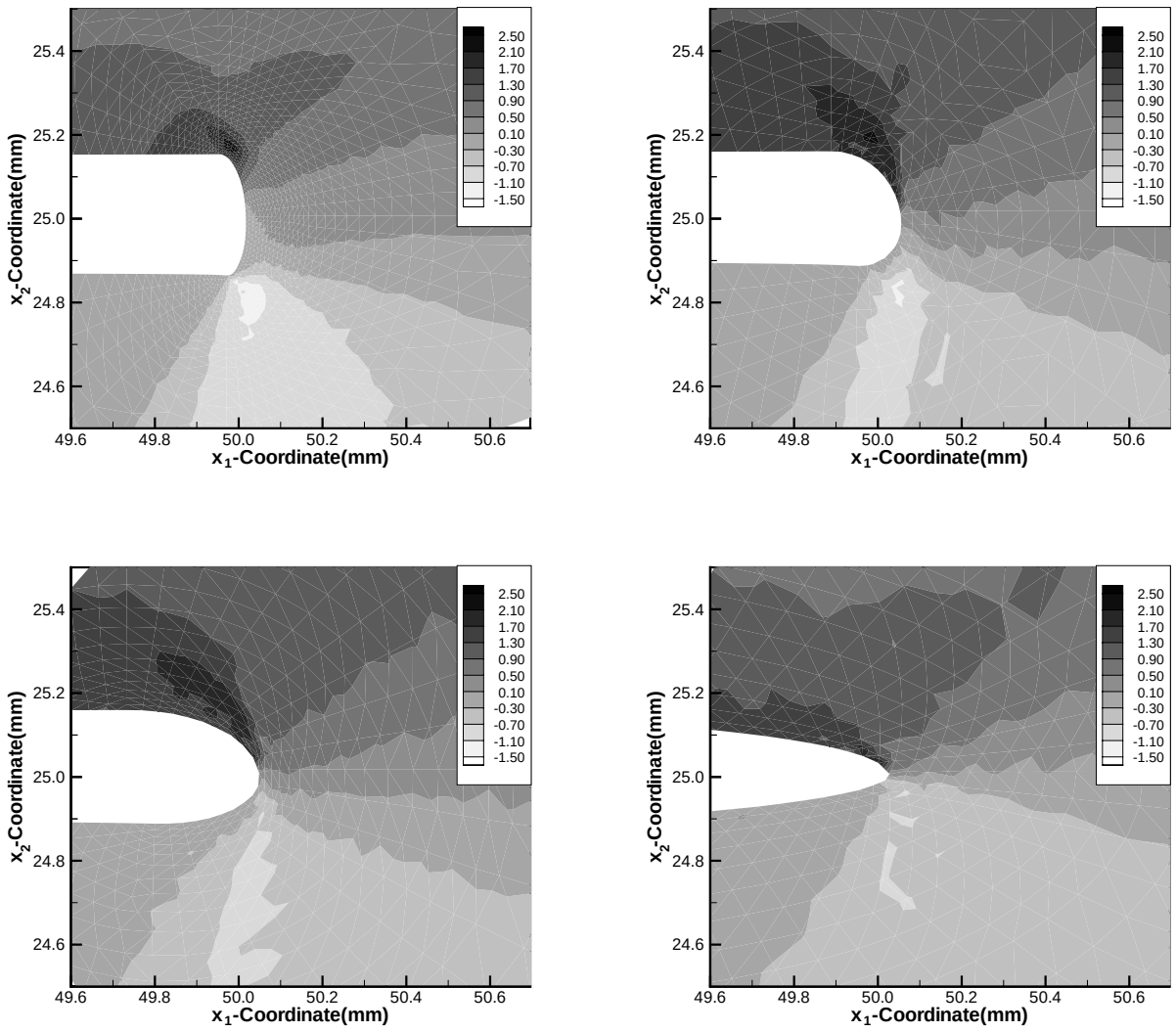

Figure 3.6: For the four elliptic notch-tips and the impact speed of 30m/s, fringe plots of the normalized maximum principal stress in a small region surrounding the surface of the notch-tip. The times at which results are plotted equal respectively 12.3, 17, 16 and 13.3 μs for $a/b = 0.4$, 1.0, 2.0 and 10.0.

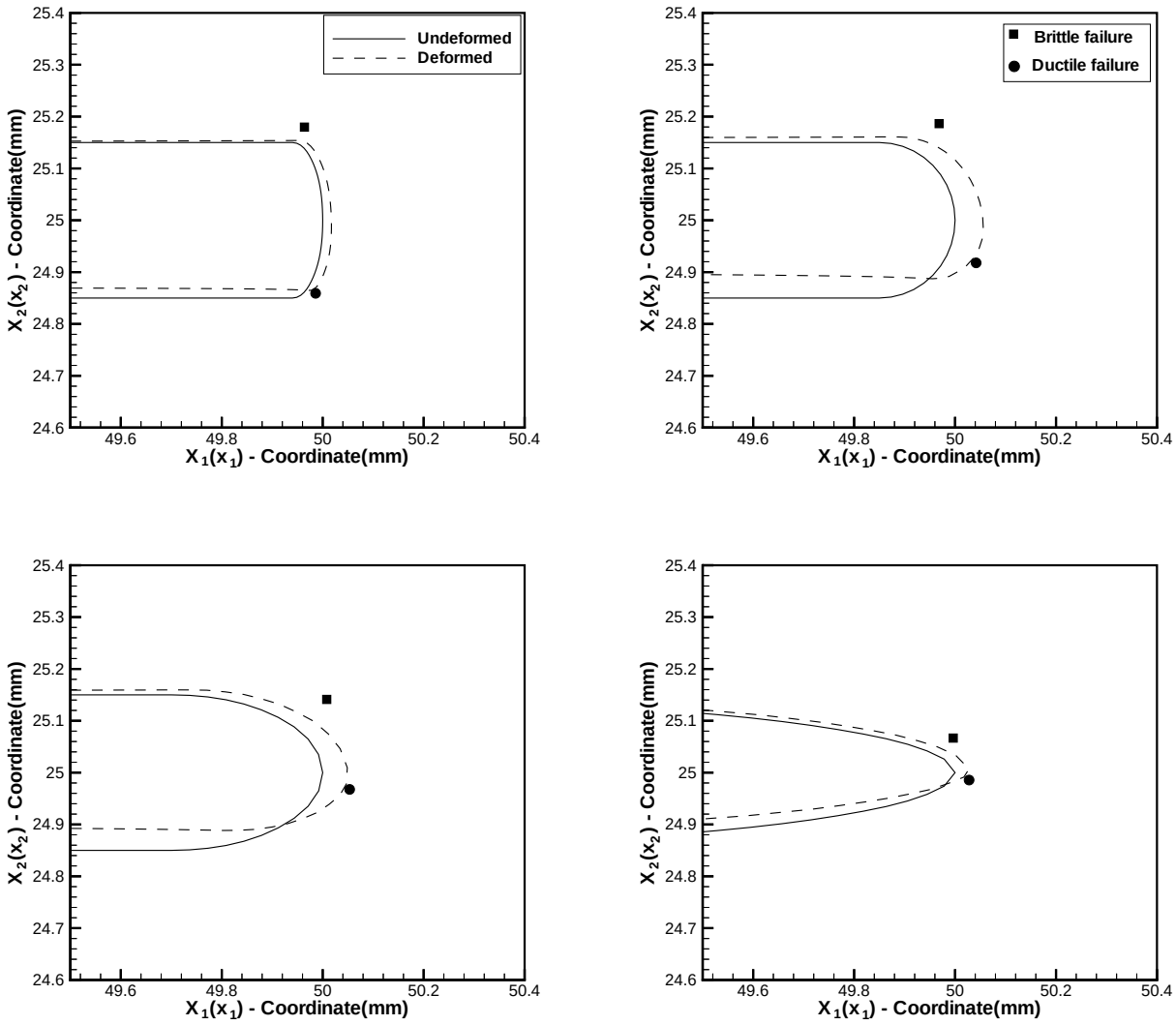

Figure 3.7: Deformed shapes of the four notch-tips, and the locations in the deformed configuration of points from where the brittle and the ductile failures initiate.

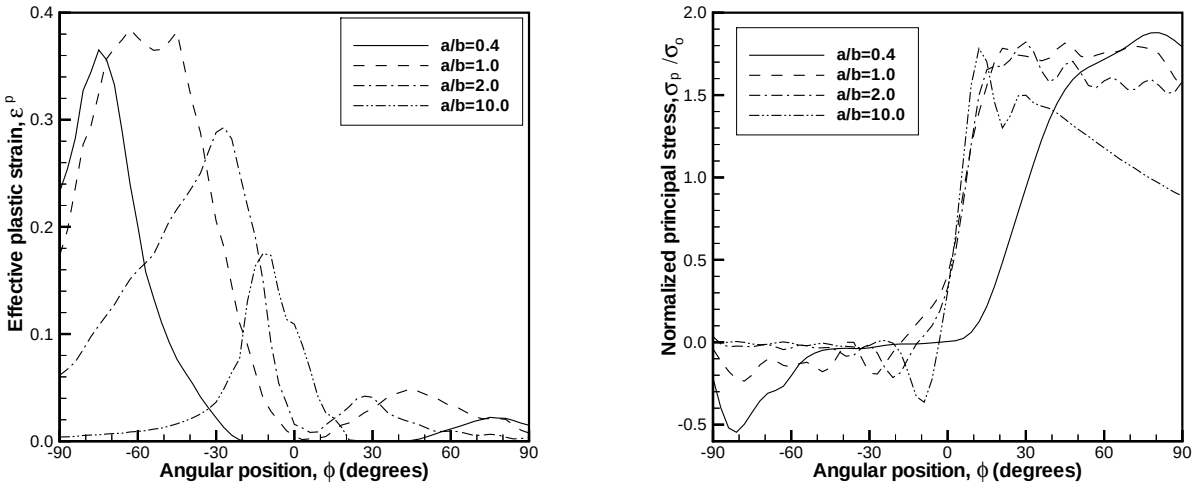

Figure 3.8: For the impact speed of 30 m/s, the angular variation of (a) the effective plastic strain, and (b) the normalized maximum principal stress at the centroids of elements abutting the notch-tip. Results are plotted at the instant of the initiation of the brittle failure, and the angular locations are in the reference configuration.

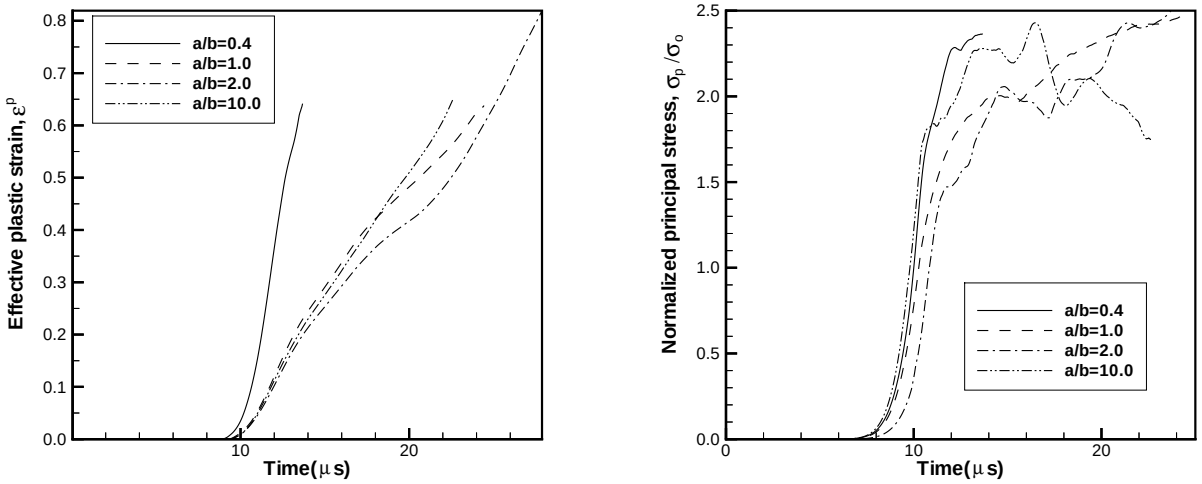

(a) (b)

Figure 3.9: For the four elliptic notch-tips, time histories of (a) the effective plastic strain, and (b) the normalized maximum principal stress at the points where at the instant of the initiation of the brittle failure maximum values of the effective plastic strain and the maximum principal stress occur respectively.

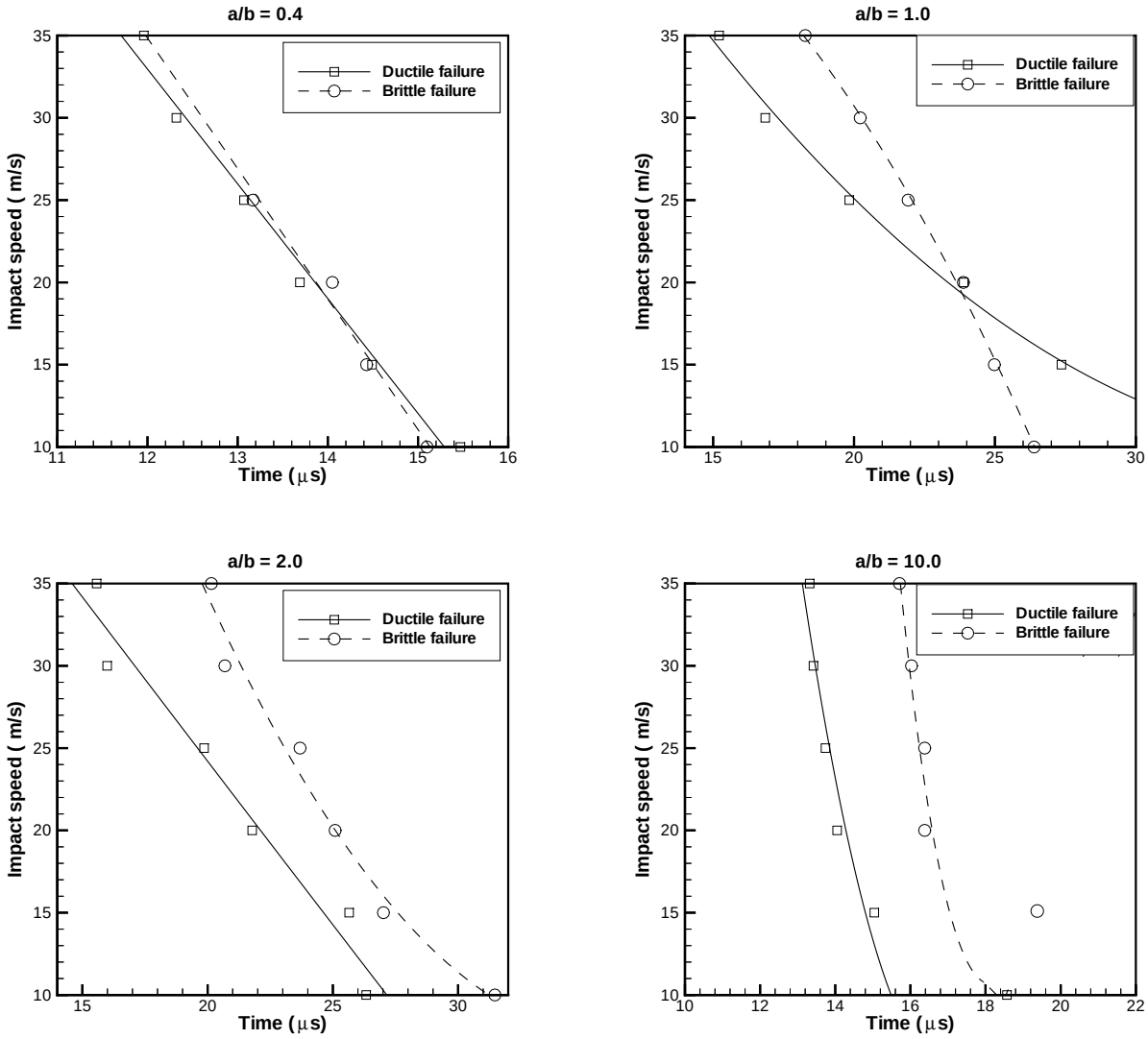

Figure 3.10: For the four elliptic notch-tips, the dependence upon the impact speed v_0 of the times of initiation of the brittle and the ductile failures.

precedes the ductile failure for impact speeds of 10, 15, 20, 25, 30 and 35 m/s. For an impact speed of 35 m/s, the brittle failure ensues at a point, P, on the lower surface of the circular hole that is closer to the circular notch tip. The line joining P to the center of the hole makes an angle in the deformed configuration of 9° counterclockwise from the axis of the notch for $d = 3r_0$ and 18° for the other three values of d. For $d/r_0 = 3$ the time of initiation of the brittle failure decreased from 12.75 μs to 10.92 μs as the impact speed was increased from 10 m/s to 35 m/s; however, the corresponding change in the time of initiation of the brittle failure is from 20.46 μs to 13.08 μs for $d = 6r_0$. In the absence of the circular hole, the time of initiation of the brittle failure equalled 26.4 and 18 μs for $v_0 = 10$ and 35 m/s respectively. Thus the presence of a hole even relatively far away from the notch tip influences both the time of initiation of the brittle failure and the point where it initiates. At the impact speed of 35 m/s, the time of initiation of the ductile failure is relatively unaffected by the presence and the location of the circular hole. For $d = 6r_0$, the ductile failure initiates from a point Q on the surface of the notch tip; the line joining Q to the center of the notch tip makes an angle in the current configuration of 27° clockwise with the axis of the notch for $v_0 = 10,\ 15$ and 20 m/s but 45° for $v_0 = 25,\ 30$ and $35m/s$. For $d/r_0 = 3,\ 4$ and 5, the location of the point of initiation of the ductile failure varied with the impact speed. For $v_0 = 35$ m/s, the ductile failure initiated at $t = 13.41$ and 15 μs respectively in the presence of the circular hole with $d = 6r_0$ and in the absence of the hole.

We have plotted in Fig. 3.12 the deformed shapes of the notch tip and the circular hole for $v_0 = 30$ m/s and at the instant of the initiation of the ductile faiure. The locations in the deformed configurations of the points of initiation of the two failure modes are also depicted. An interesting observation is that the circular hole is also severely distorted and the brittle failure initiates from a point near the surface of the circular hole rather than from a point close to the surface of the notch tip. Except for $d/r_0 = 3$, the ductile failure ensues from a point adjacent to the surface of the notch tip.

For an impact speed of 25 m/s, Figs. 3.13, 3.14 and 3.15 evince the fringe plots of the effective plastic strain, the normalized maximum principal stress and the nondimensional shear stress

σ_{12} in a small region including the notch-tip and the circular hole. In each case results are plotted at the instant the ductile failure ensues since it occurs later; the times when these Figs. are plotted equal 14.0, 15.0, 17.3 and 18.7 μs for $d/r_0 = 3,\ 4,\ 5$ and 6 respectively. Except for the values of the time of initiation of the failure, qualitatively similar results were obtained for impact speeds of 10, 15, 20, 30 and 35 m/s. In the absence of the circular hole, the brittle and the ductile failures initiate respectively at 22 and 20 μs after impact. Thus the presence of the circular hole at $d/r_0 = 3, 4, 5$ or 6 makes the brittle failure occur sooner. The fringes of the effective plastic strain plotted in Fig. 3.13 indicate four severely deformed regions - two emanating from a point on the lower surface of the notch-tip and the other two from a point on the lower surface of the circular hole. Note that the lower surface of the notch-tip is closer to the impacted edge. The qualitative nature of results is the same for each one of the four values of d. The most intensely deformed narrow region is around the line joining a point on the lower surface of the notch-tip to a point on the upper surface of the hole. The locations, in the reference configuration, of these points can be discerned from the plots, given in Fig. 3.16a of the distribution of the effective plastic strain in elements adjoining the circular notch-tip and the hole. With an increase in the value of d/r_0 from 3 to 6, the angular position in the deformed configuration of the point on the surface of the notch-tip where the effective plastic strain is maximum shifts from -16° to -27°, and that on the hole from 154° to 162°; in each case the positive angles are measured clockwise from the axis of the notch. Without the hole, the angular position in the deformed configuration of the point on the surface of the circular notch-tip where the effective plastic strain is maximum equals -50°. Thus the presence of the hole shifts the location of the nucleus of the shear band on the notch-tip surface towards the axis of the notch. Within the intensely deformed narrow region joining a point on the circular notch-tip to a point on the circular hole, the maximum value of the effective plastic strain at a point near the circular hole is more than that at a point adjacent to the circular notch-tip. A small region around the point located, in the reference configuration, at -70° on the surface of the notch-tip is also intensely deformed. With an increase in the value of d/r_0 from 3 to

6, the maximum value of the effective plastic strain in this region increases from 0.07 to 0.2 and that in the material around the point P decreases from 0.27 to about 0.25; the point P is located, in the reference configuration, on the surface of the notch tip at an angular position of about $-30°$. As is evident from the results plotted in Fig. 3.16a, a small region surrounding point T, located in the reference configuration at about $-60°$, on the surface of the circular hole is also severely deformed; the maximum effective plastic strain at a point in this region equals approximately 0.20 for $d/r_0 = 3$ and 6. The corresponding values of the effective plastic strain in the intensely deformed region around the point R, located in the reference configuration at about 150°, on the circular hole are 0.37 and 0.28. Thus there are four regions wherein the effective plastic strain is large; two of these regions are around the points on the surface of the notch-tip and the other two are around the points R and T on the surface of the circular hole. Fringe plots of the maximum principal stress and the shear stress σ_{12} given respectively in Figs. 3.14 and 3.15 reveal that the maximum principal stress is compressive and the magnitude of the shear stress is large in intensely deformed regions.

For an impact speed of 25 m/s, Fig. 3.17a shows the time histories of the evolution of the effective plastic strain and the maximum principal stress at points close to the surface of the notch tip where their maximum values occur at the instant of the initiation of the ductile failure; the corresponding results for points around the circular hole are depicted in Fig. 3.17b. A comparison of the evolution of the effective plastic strain at the points near the notch tip and the circular hole suggests that for $d/r_0 = 0.3$, the initial effective plastic strain rates at the former and the latter locations are about $6.8 \times 10^4/s$ and $8 \times 10^4/s$ respectively. At points around the notch tip and the circular hole, the initial effective plastic strain rate decreases with an increase in the value of d/r_0. In each one of the four plots of Figs. 3.17a and 3.17b, the effect of the circular hole is more noticeable for $d/r_0 = 3$ than for its other three locations.

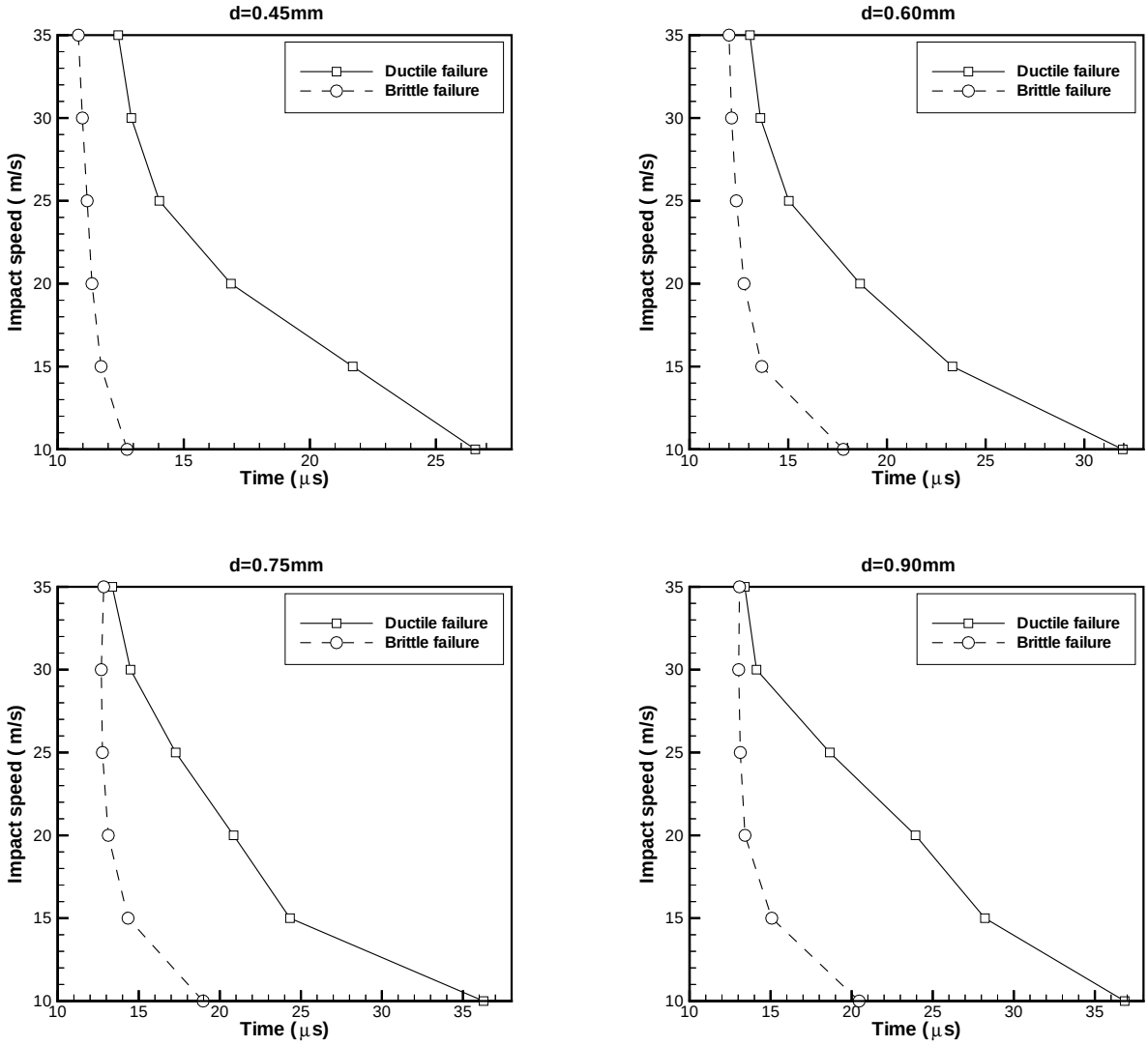

Figure 3.11: For the four locations of the circular hole ahead of the notch-tip, the dependence upon the impact speed of the times of initiation of the brittle and the ductile failures.

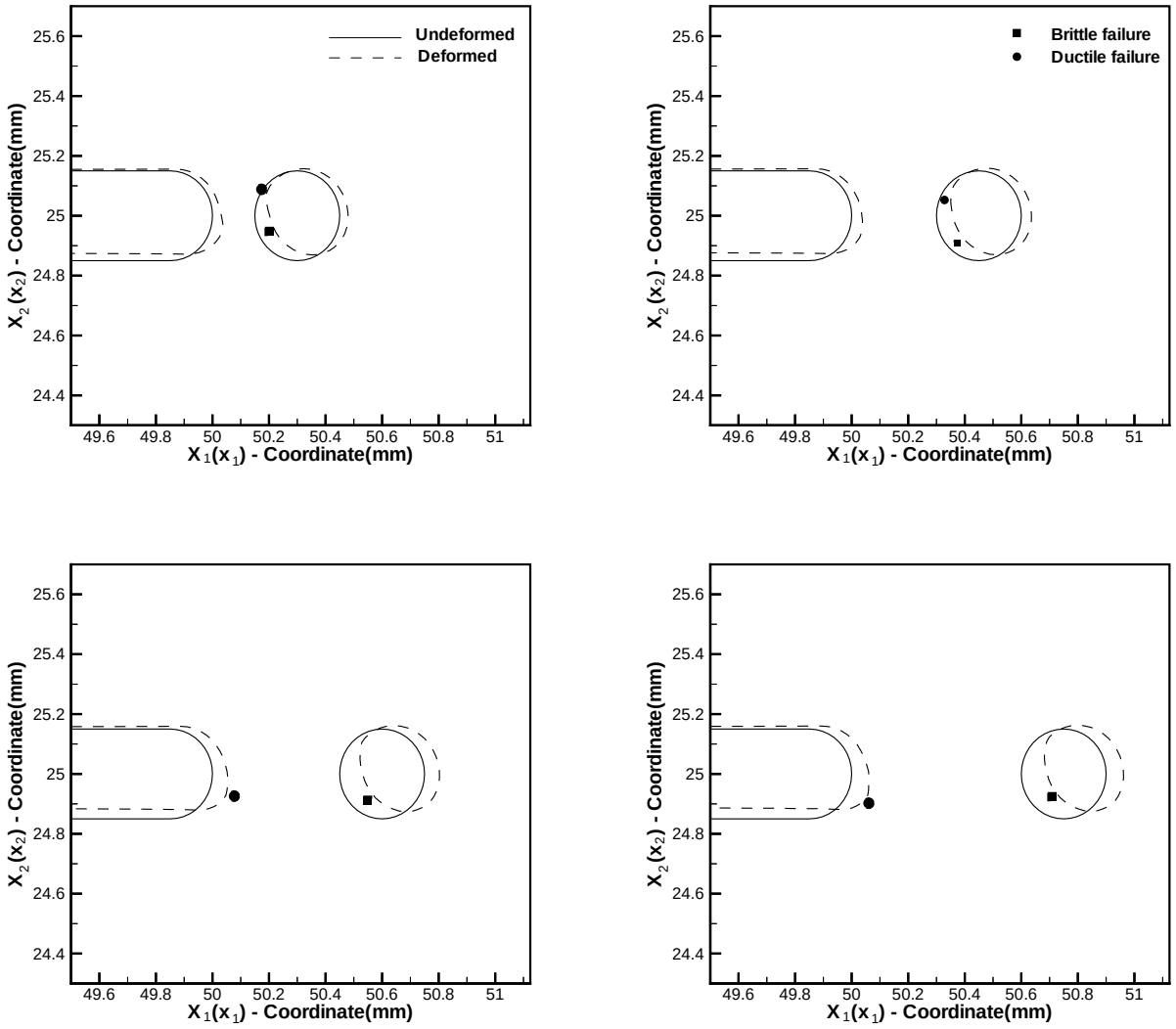

Figure 3.12: Deformed shapes of the notch tip and the circular hole, and the locations of the points of initiation of the brittle and the ductile failures.

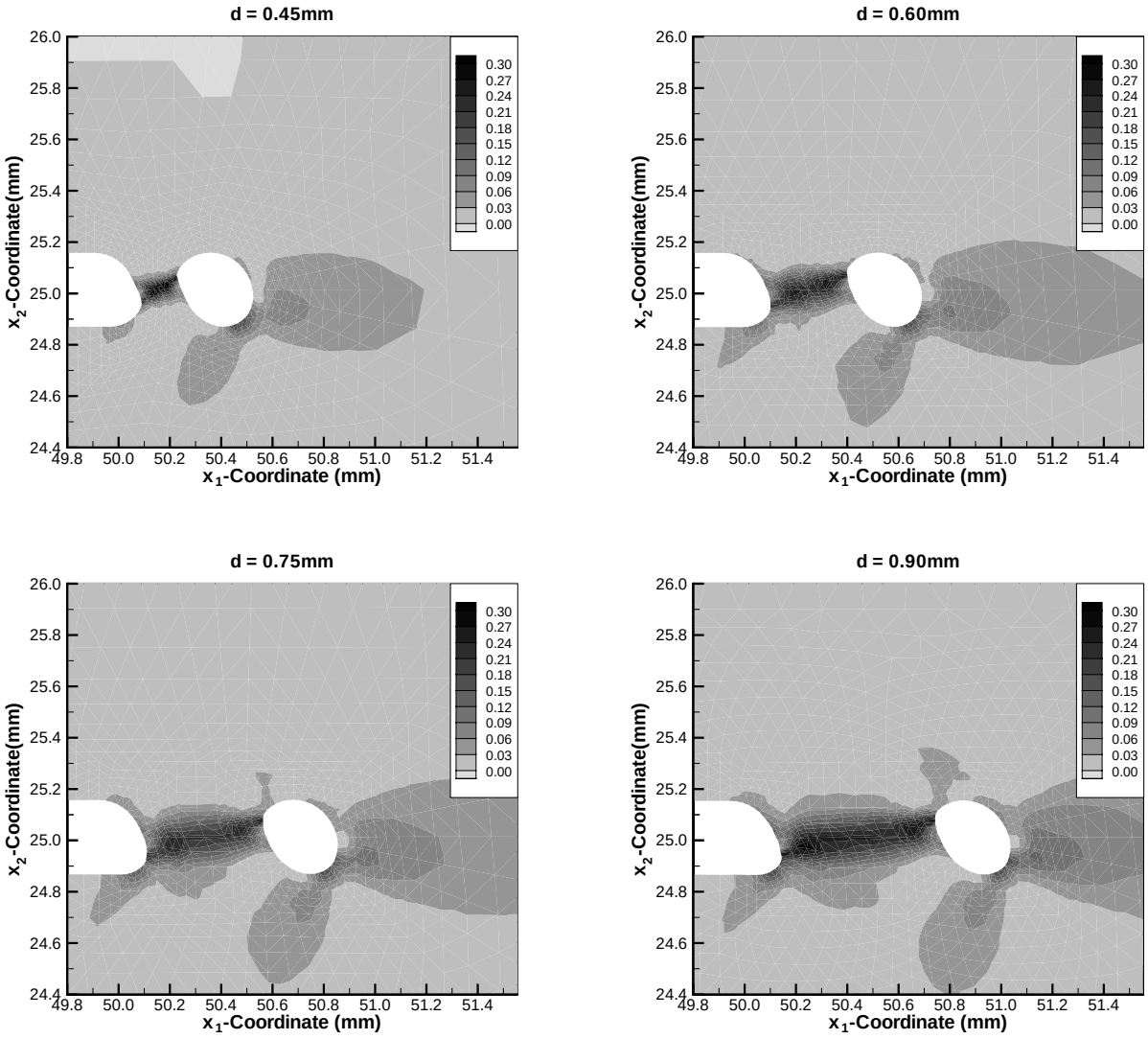

Figure 3.13: For the four locations of the circular hole ahead of the notch-tip and the impact speed of 25 m/s, fringe plots in a small region around the notch-tip and the circular hole of the effective plastic strain. The times at which these results are plotted equal 17.2, 21.6, 23.6 and 22.1 μs respectively for $d/r_0 = 3,\ 4,\ 5$ and 6.

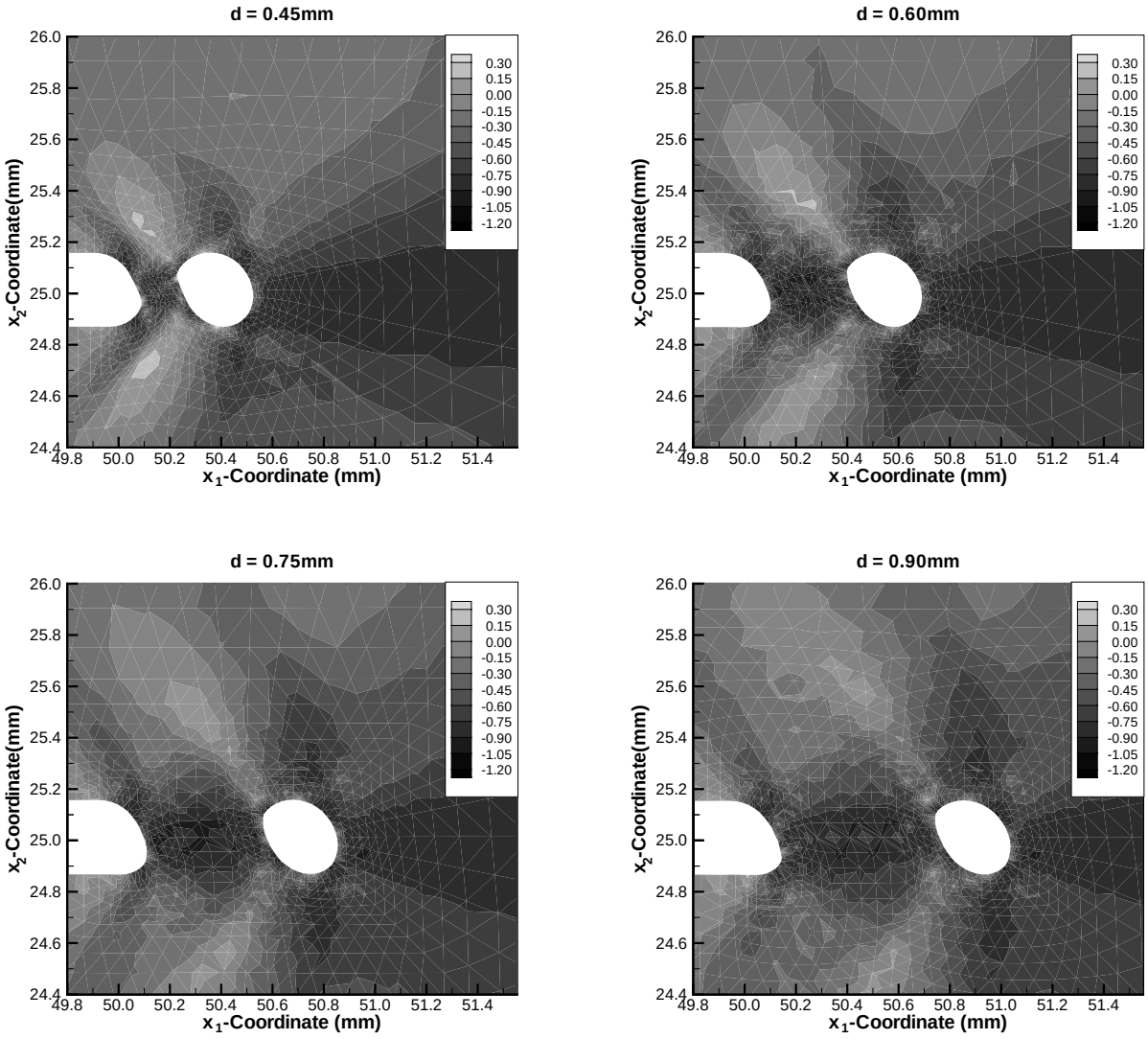

Figure 3.14: For the four locations of the circular hole ahead of the notch-tip and the impact speed of 25 m/s, fringe plots in a small region around the notch-tip and the circular hole of the shear stress σ_{12}. The times at which these results are plotted equal 17.2, 21.6, 23.6 and 22.1 μs respectively for $d/r_0 = 3,\ 4,\ 5$ and 6.

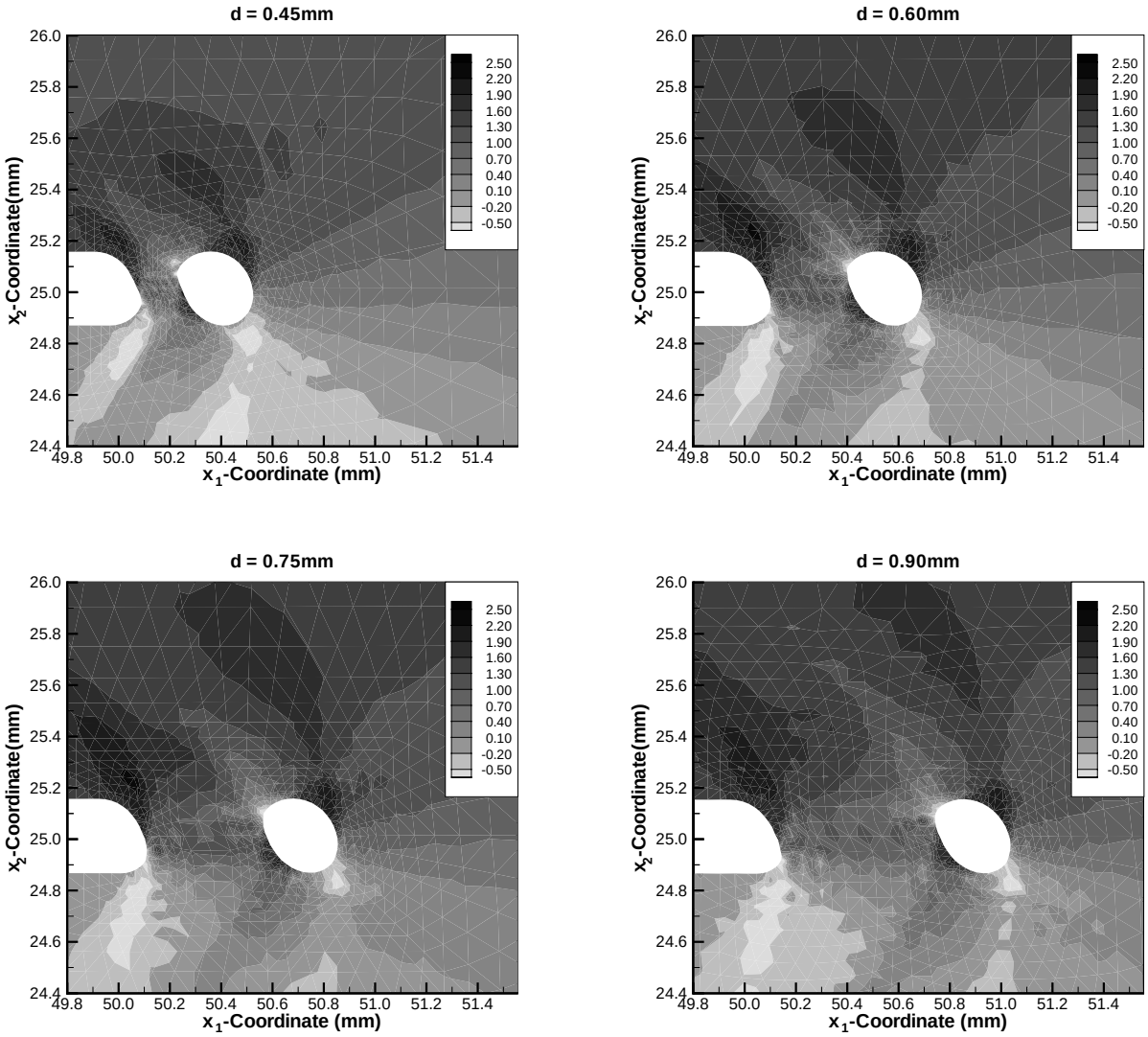

Figure 3.15: For the four locations of the circular hole ahead of the notch-tip and the impact speed of 25 m/s, fringe plots in a small region around the notch-tip and the circular hole of the maximum principal stress. The times at which these results are plotted equal 17.2, 21.6, 23.6 and 22.1 μs respectively for $d/r_0 = 3,\ 4,\ 5$ and 6.

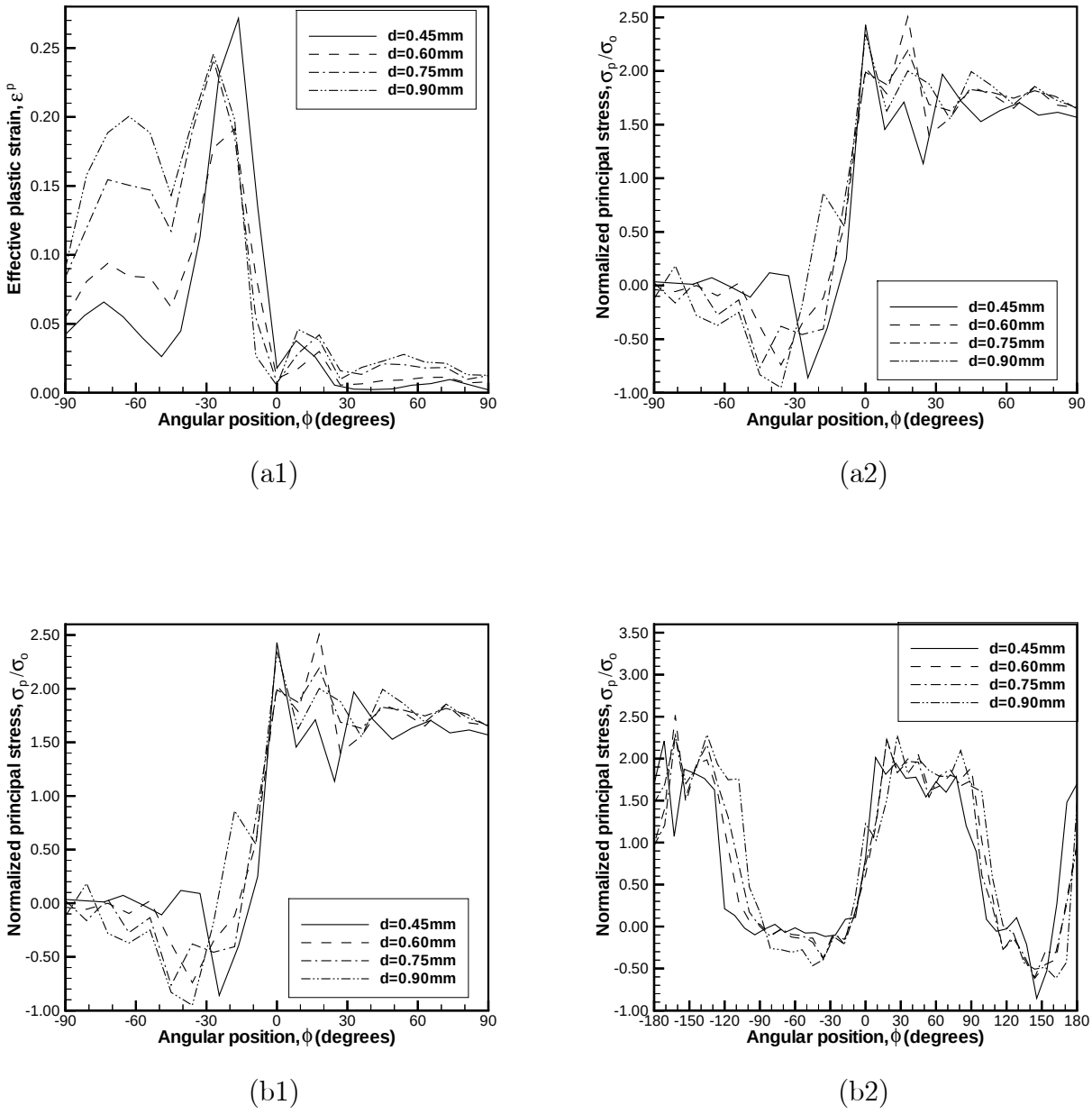

Figure 3.16: For the impact speed of 25 m/s, the angular variation of (a) the effective plastic strain, and (b) the normalized maximum principal stress at the centroids of elements abutting the notch-tip and the circular hole. Results are plotted at the instant of the initiation of the ductile failure, and angular positions are in the reference configuraiton.

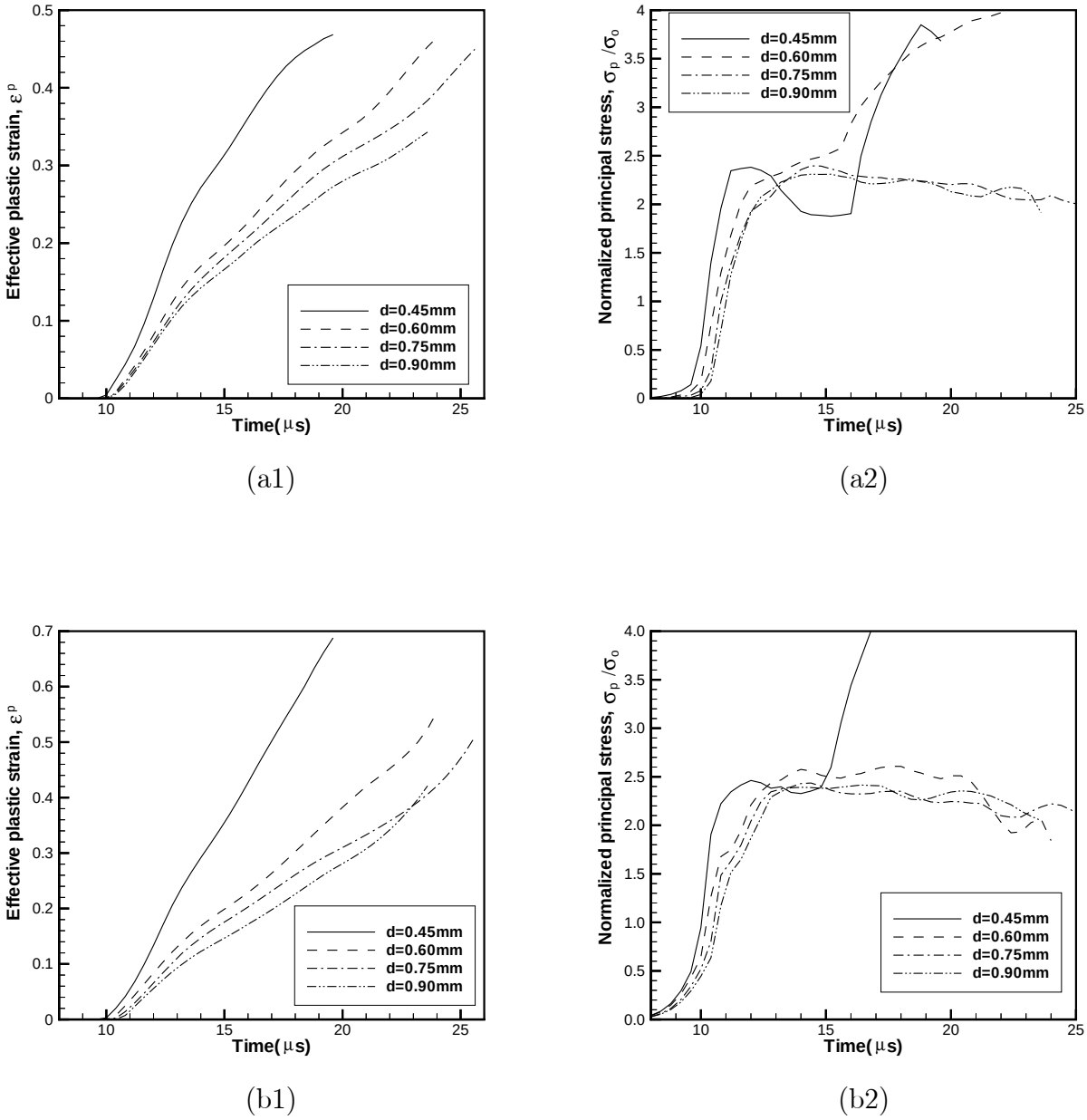

Figure 3.17: For the impact speed of 25 m/s, the time history of the effective plastic strain and the normalized maximum prinipal stress at the points (a) near the notch tip and (b) near the hole where their maximum values occur at the instant of the initiation of the ductile failure.

3.5.2 Circular Hole Located Away from the Axis of the Notch

For an impact speed of 35 m/s and $e/r_0 = \pm 1$ and ± 3, we have plotted in Figs. 3.18, 3.19 and 3.20 fringes of the effective plastic strain, the normalized shear stress σ_{12} and the normalized maximum principal stress. These results are plotted at $t = 15.3,\ 15.6,\ 13.1$ and 17.0 μs respectively for $e/r_0 = 1,\ 3,\ -1$ and -3; these times correspond to the times of initiation of the brittle failure for $e/r_0 = -1$ and -3, and to the time of onset of the ductile failure for $e/r_0 = 1$ and 3. Positive values of e/r_0 indicate that the hole is located above the axis of the notch; cf. Fig. 4.2c. The angular distributions of the effective plastic strain and the normalized maximum principal stress at points abutting the circular notch tip and the circular hole are exhibited in Fig. 3.21 wherein the angular positions of points are in the reference configuration. For $e/r_0 = 3$, the presence of the hole has a modest effect on the location of the point on the notch surface where the maximum effective plastic strain occurs, and on the location and shape of the severely deformed region. The angular distribution of the effective plastic strain around the surface of the notch tip and its maximum value are quite similar to those computed for the circular notch tip in the absence of the circular hole and depicted in Fig. 3.21a. Note that the impact speeds and the times when these results are plotted are different in the two cases. Whereas the circular hole with its center located at $e/r_0 = 3$ does not influence much the deformations of the material around the notch-tip, the hole located at the other three locations significantly affects deformations of the material around the notch-tip and the hole. For $e/r_0 = 1$, a large portion of the lower surface of the notch-tip ($-90^\circ \leq \phi \leq 0^\circ$) is severely deformed, and there is also a small region of the upper surface where the effective plastic strain is noticeable. In the absence of the hole, the effective plastic strain at points on the upper surface of the notch-tip is quite small. There appear to be four regions of intense plastic deformations; two emanating from a point on the right side of the lower surface of the hole, one within the small region joining a point on the upper surface of the notch-tip to a point on the upper surface of the circular hole, and the fourth one originating from a point on the lower surface of the notch-tip and propagating at an angle of approximately -135° to the notch-axis. For $e/r_0 = -1$ and -3, the intense

plastic deformations originating from a point on the bottom right side of the circular hole propagate essentially horizontally. A narrow region joining a point on the lower surface of the notch-tip to a point on the upper surface of the circular hole is very intensely deformed. For the case of the $e/r_0 = -3$, the effective plastic strain in the material above this narrow region is noticeably more than that in the region below it. For $e/r_0 = -1$ and -3, there is a small leaflet like region pointing in the -135° direction wherein the effective plastic strain is also large; this region surrounds points on the lower surface of the notch tip.

Fringe plots of the shear stress σ_{12} depicted in Fig. 3.19 suggest that for $e/r_0 = -1$ and -3, the magnitude of the shear stress is the largest in narrow essentially horizontal regions originating from a point on the lower right surface of the circular hole. The magnitude of the shear stress is also quite large in the other narrow regions joining a point on the lower surface of the notch-tip to a point on the upper surface of the circular hole. For all four locations of the circular hole, the magnitude of the shear stress is large in regions which have significant plastic strains.

Fringe plots of the maximum principal stress and its distribution around the surfaces of the notch tip and the circular hole reveal that the presence of the hole at the four locations does not appreciably influence the distribution, exhibited in Fig. 3.21, of the maximum principal stress around the surface of the notch-tip. However, for $e/r_0 = 1$ and 3, the maximum principal stress at points on the lower left side of the circular hole is significantly larger than that at points similarly situated for $e/r_0 = -1$ and -3. For all four locations of the circular hole, the distribution of the maximum principal stress at points on the upper surface of the circular hole is qualitatively similar except that for $e/r_0 = -3$, the region around the circular hole with large values of the maximum tensile principal stress is quite small.

We have plotted in Fig. 3.22 the deformed shapes of the notch tip and the circular voids for the four locations of the hole, and have also marked the locations of the points from where the brittle and the ductile failures initiate. In each case, the circular hole is displaced in the direction of impact, and the horizontal movement is largest for $e/r_0 = -3$ because it is then

directly ahead of the impacted edge. The brittle failure initiates from a point on the surface of the circular hole for all four locations of the hole. For $e/r_0 = \pm 1$, the point of initiation of the ducitle failure is also adjacent to the surface of the hole, but for $e/r_0 = \pm 3$, the ductile failue ensues from a point near the lower surface of the notch tip which is the case when there is no hole. Thus the presence of the holes with $e/r_0 = \pm 3$ influences more the location of the brittle failure.

Figure 3.23 depicts the time histories of the effective plastic strain and the maximum principal stress at points adjacent to the surfaces of the notch tip and the circular hole where their maximum values occur at the time of initiation of the ductile failure. For $e/r_0 = -1$ and -3, the initial effective plastic strain at the points near the notch tip surface and the circular hole is $1 \times 10^5/s$ which is a little higher than that when there is no hole or when the hole is located above the axis of the notch. The dependence upon the impact speed of the times of initiation of the brittle and the ductile failures is exhibited in Fig. 3.24. Comparing these with the results plotted in Fig. 4.7 we see that the presence of the hole at $e/r_0 = \pm 1$ and 3 accelerates the initiation of the brittle failure while that at $e/r_0 = -3$ retards it. However, the holes located at $e/r_0 = -1$ and -3 enhance the onset of the ductile failure.

3.6 Effect of Specimen Height

Figure 3.25 shows a schematic sketch of the problem studied. The notch tip is elliptic with the major principal axis aligned along the axis of the notch and of length equal to twice the length of its minor principal axis. Figure 3.26 exhibits the effect of the height h of the specimen above the notch surface on the deformed shape of the notch tip at time $t = 27.2\mu s$ after the plate is impacted; deformed notch shapes for $h = 50mm$ and $75mm$ are essentially identical. It is clear that the value of h has virtually no effect on the deformations of the lower surface of the notch. Points on this surface move upwards because of the Poisson effect and they also move axially in the impact direction. Once a compressive loading wave arrives

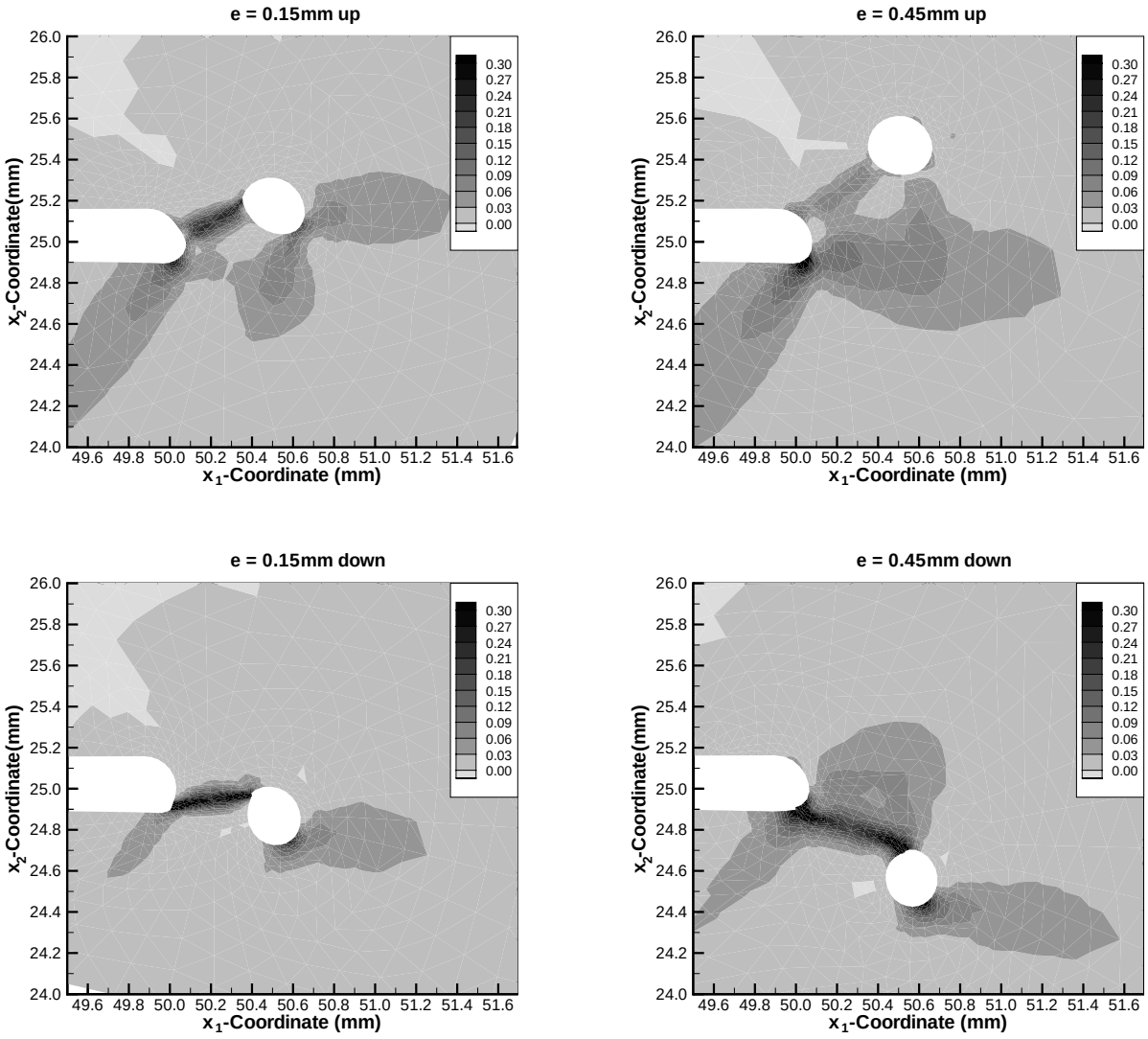

Figure 3.18: For the impact speed of 35 m/s, fringe plots of the effective plastic strain in a small region enclosing the notch-tip and the circular hole. Times at which results are plotted equal respectively 15.3, 15.6, 13.1 and 17.0 μs for $e/r_0 = 1,\ 3,\ -1$ and -3.

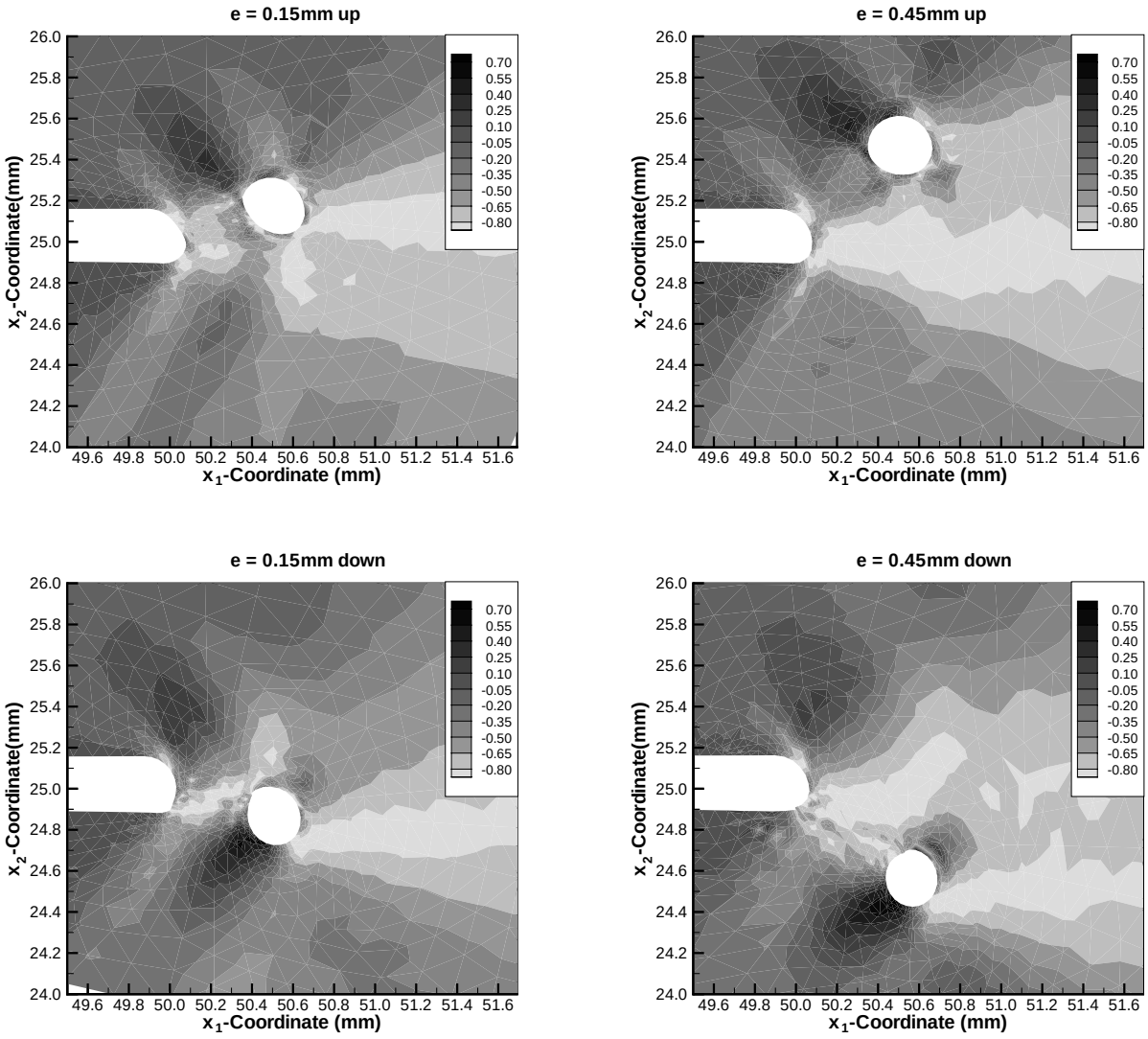

Figure 3.19: For the impact speed of 35 m/s, fringe plots of the normalized shear stress σ_{12} in a small region enclosing the notch-tip and the circular hole. Times at which results are plotted equal respectively 15.3, 15.6, 13.1 and 17.0 μs for $e/r_0 = 1,\ 3,\ -1$ and -3.

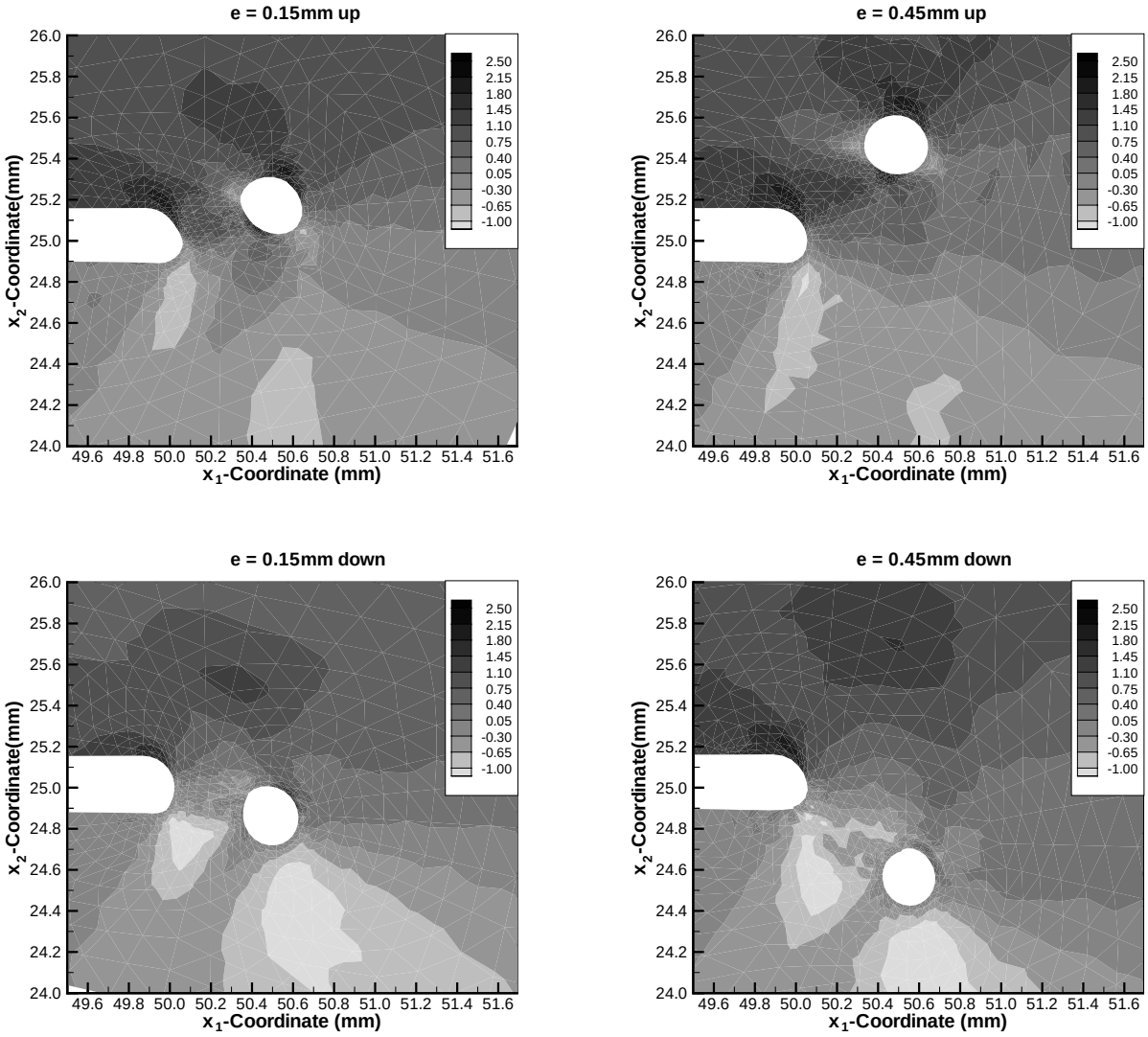

Figure 3.20: For the impact speed of 35 m/s, fringe plots of the normalized maximum principal stress in a small region enclosing the notch-tip and the circular hole. Times at which results are plotted equal respectively 15.3, 15.6, 13.1 and 17.0 μs for $e/r_0 = 1,\ 3,\ -1$ and -3.

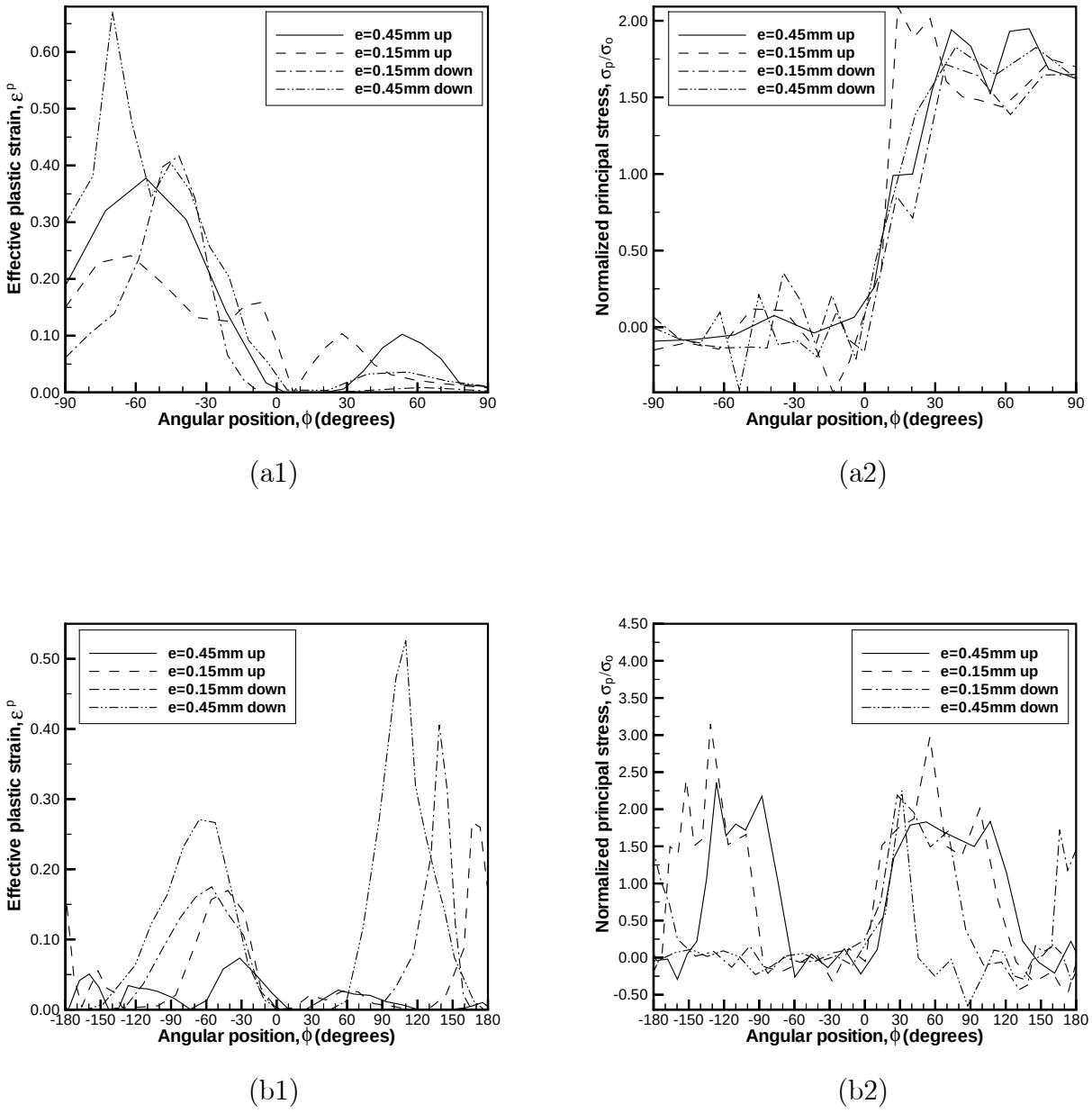

Figure 3.21: For the impact speed of 35 m/s, the angular variations of the effective plastic strain, and the normalized maximum principal stress at the centroids of elements adjoining the surface of (a) the notch-tip and (b) the circular holes; the angular locations are in the reference configuration.

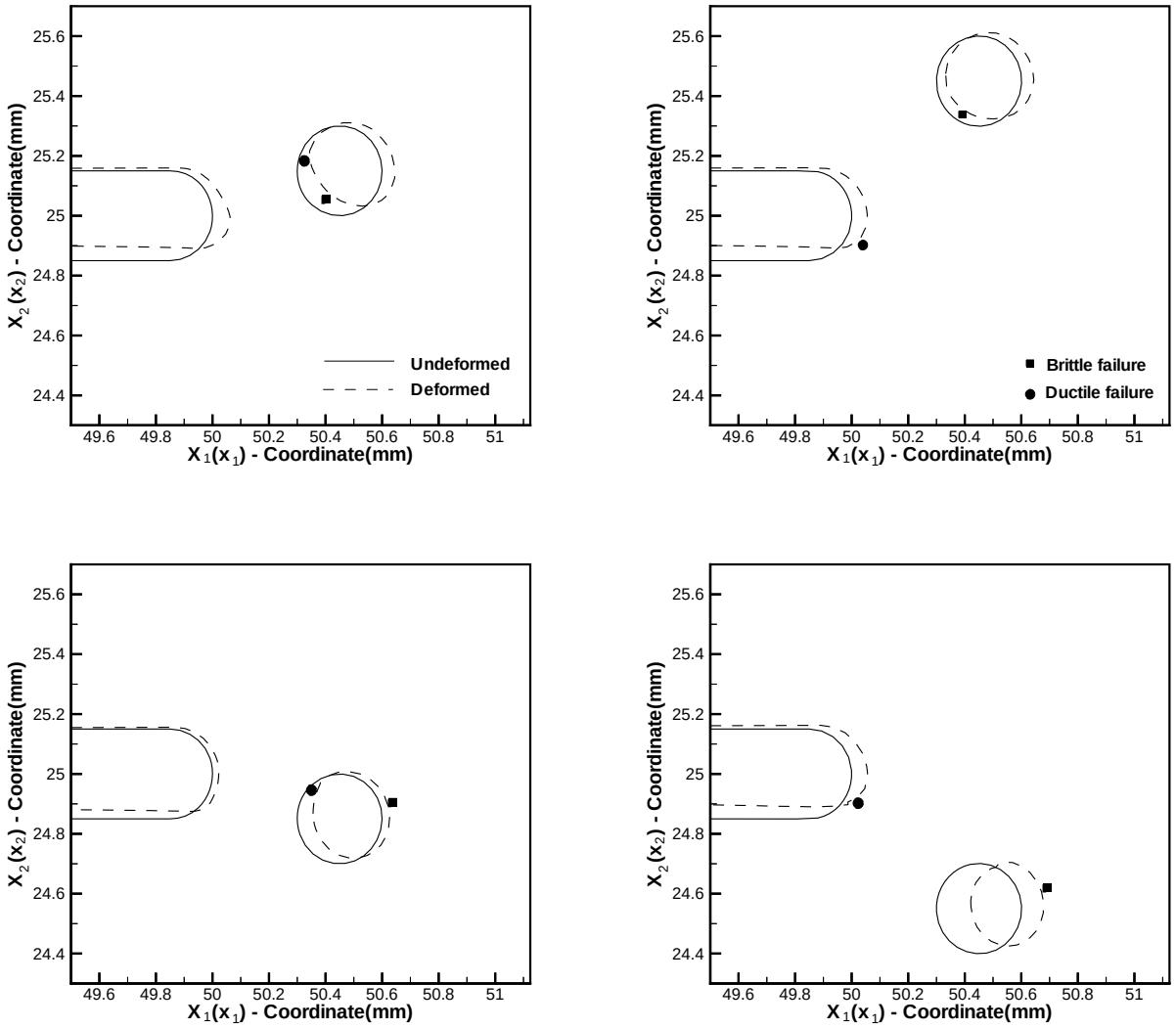

Figure 3.22: Deformed shapes of the notch tip and the circular hole, and the locations of the points of initiation of the brittle and the ductile failures.

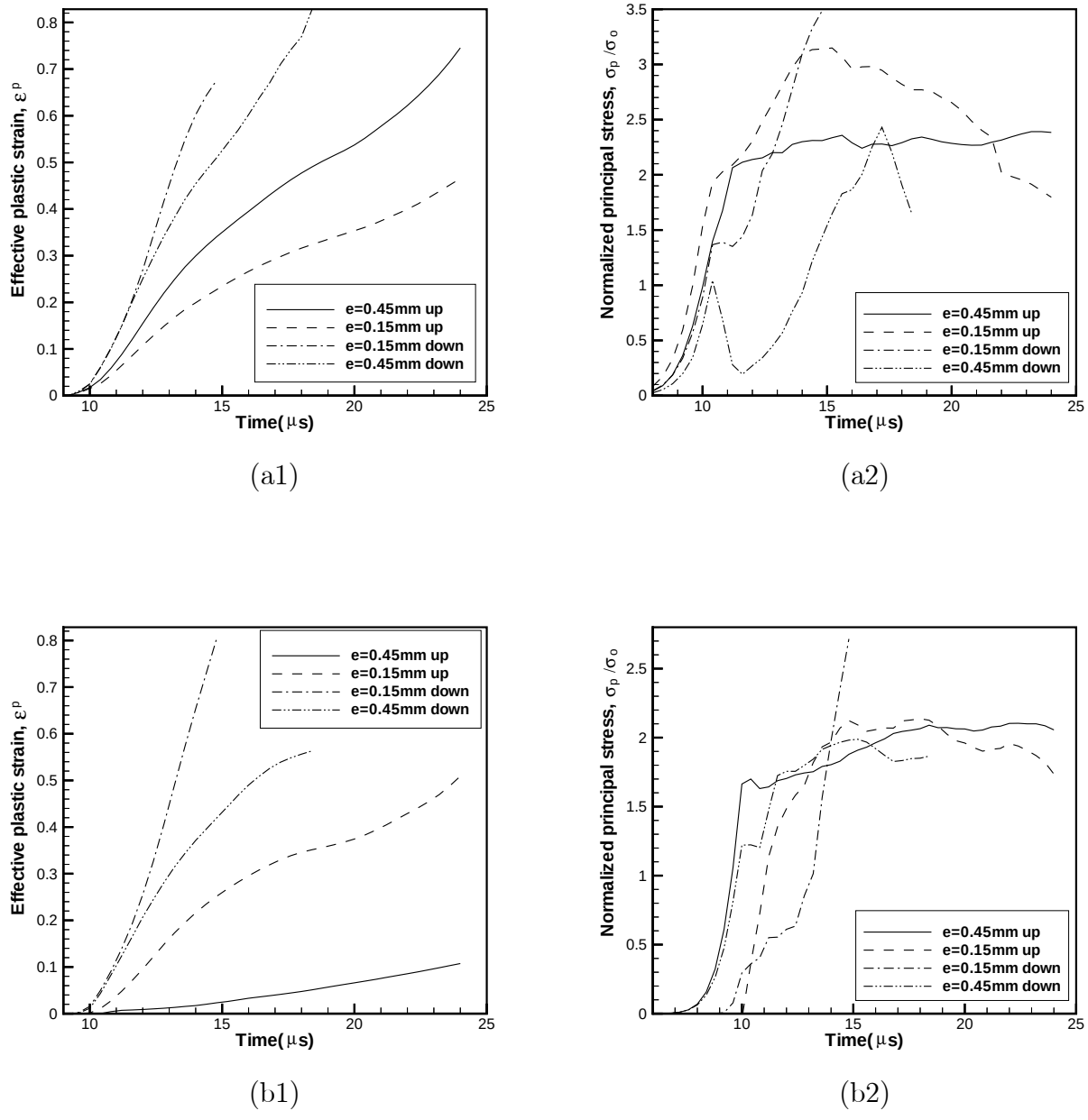

Figure 3.23: For the impact speed of 35 m/s, time histories of the effective plastic strain and the maximum principal stress at points near the surface of (a) the notch tip and (b) the circular hole where their maximum values occur at the time of initiation of the ductile failure.

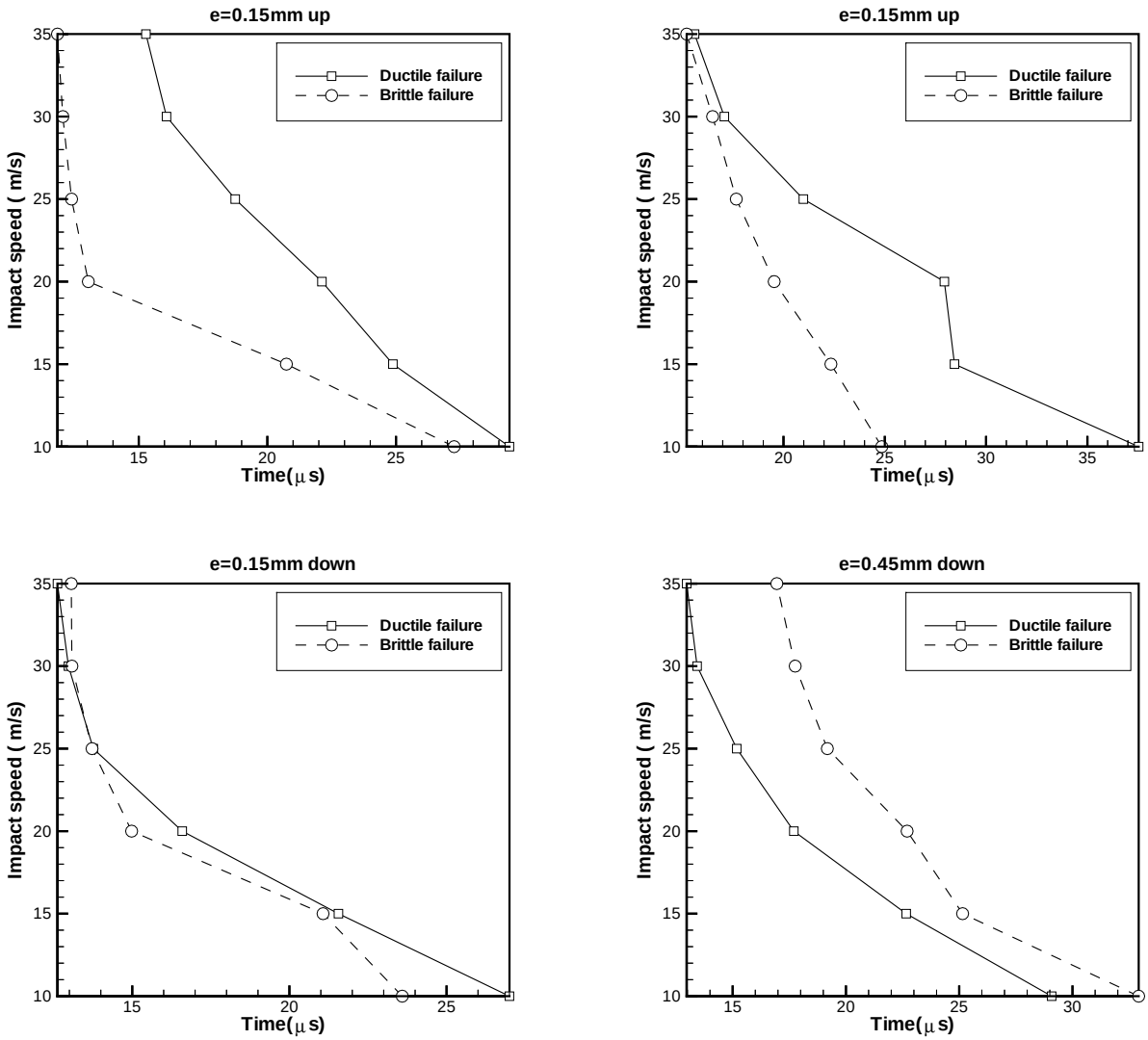

Figure 3.24: For the four locations of the circular hole with its center either above or below the axis of the notch, the dependence upon the impact speed of the times of initiation of the brittle and the dcutile failures.

at the notch-tip at about $10\mu s$, it is scattered. For $h = 10$ and $25mm$, stress waves after being reflected from the top traction free edge arrive at the notch tip at $t < 27.2\mu s$ and influence its deformations. However, for $h = 50\mu s$, such is not the case

Figure 3.27 depicts the dependence of the times of initiation of the two failure modes upon the specimen height. For each one of the four values of h, the ductile failure precedes the brittle one. Whereas an increase in the value of h delays the onset of the ductile failure, it enhances the initiation of the brittle failure. The time of initiation of the brittle failure decreases rapidly from $27.2\mu s$ to $21\mu s$ as the specimen height above the notch surface is increased from 10 to $25mm$, and remains unchanged when h is increased from 50 to $75mm$. For each value of h, the brittle failure originated from a point located a little away from the surface of the notch tip, and on the line passing through the center of the notch tip and making an angle ϕ, in the reference configuration, of 30° counter-clockwise with the notch axis. The point of initiation of the ductile failure is essentially on the surface of the notch tip and the line joining it with the center of the notch tip makes an angle, in the reference configuration, of 18° clockwise with the notch axis.

The angular variations of the effective plastic strain at points abutting the surface of the notch tip exhibited in Fig. 3.28 reveal that for each value of h the severely deformed region is concentrated around the line $\phi = -18°$. For $h = 50$ and $75mm$, the maximum effective plastic strain induced is very high as compared to that for $h = 10mm$. It drops off rapidly as one moves towards the axis of the notch but slowly in the other direction. The fringe plots of the effective plastic strain in a small region around the notch tip indicate that for each value of h two regions of intense plastic deformation or ASBs emanate from points on the surface of the notch tip; one ASB propagates along the axis of the notch and the other one at nearly 135° clockwise to the notch axis.

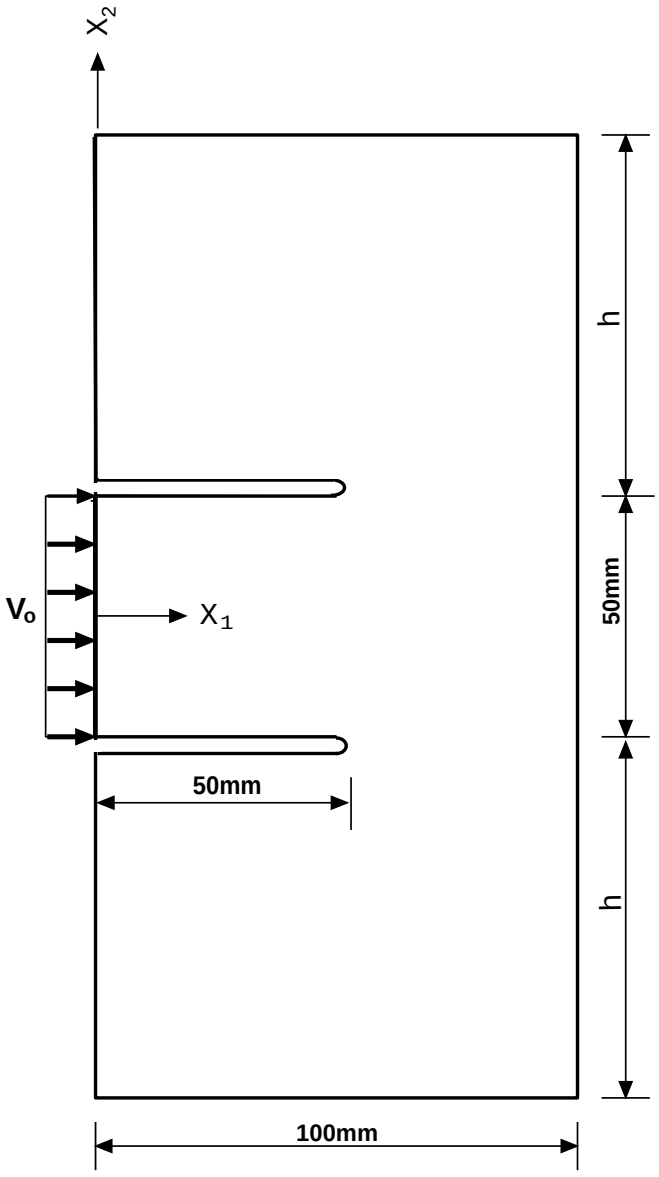

Figure 3.25: A schematic sketch of the problem studied.

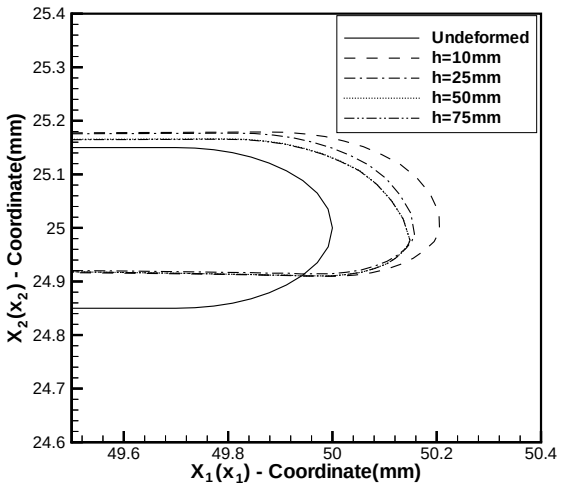

Figure 3.26: For different values of h, deformed shapes of the elliptical notch tips at $t = 27.2\mu s$.

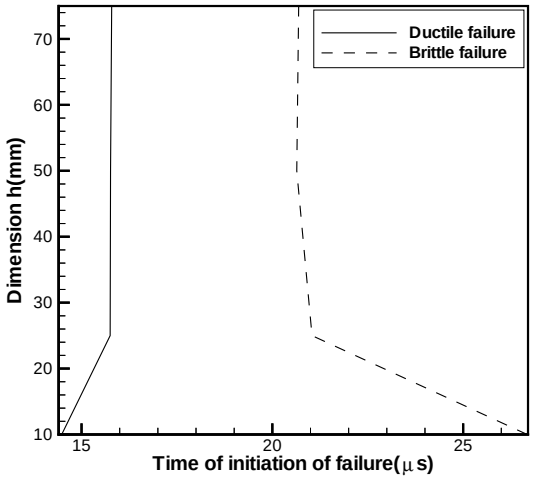

Figure 3.27: Dependence of the times of initiation of the two failure modes upon the height h of the specimen.

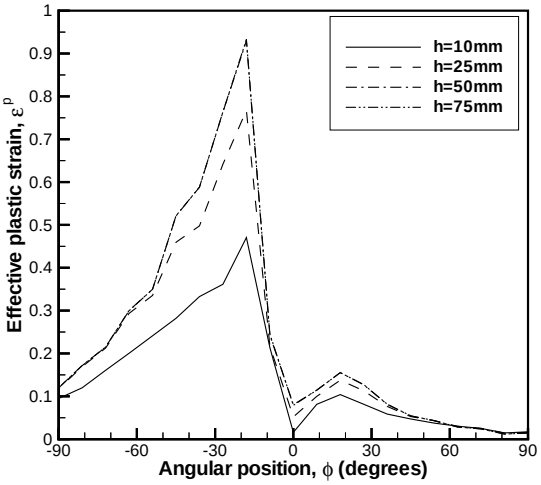

Figure 3.28: Angular variation of the effective plastic strain for four values of the height, h, of the specimen above the upper notch.

Chapter 4

Crack Simulation

4.1 Introduction

Dynamic crack propagation has been studied by utilizing one of the following three methods: the moving mesh method, the node split or release technique and the element extinction method. In the moving mesh method, a mesh that moves with the crack tip is used. Examples utilizing this method include the works of Atluri and Nishioka [3], Koh et al. [61] and Thesken and Gudmundson [90]. In the node split technique, the location of the crack tip is moved from one node to another node along the crack path. The sudden release of a node induces oscillations in the stress field around the crack tip, and hence may lead to numerical difficulties in the finite element solution. In order to overcome these difficulties, a gradual release of the constraint force over a specified time interval is used. Crack simulation using the node split technique with the gradual release of the constraint force is found in the works of Aoki et al. [2], Yagawa et al. [106] and Kobayashi et al. [60]. Lastly, the element extinction technique or the element vanish technique is utilized by neglecting the failed element's contribution to the finite element solution. This is done by deleting the element's history data, such as stresses and plastic strains, and by setting the Young's modulus and the Poisson ratio of the element equal to zero. Examples of the element extinction technique

are found in the works of Tvergaard [97] and Beissel et al. [28].

In order to simulate the crack initiation and propagation, we developed an algorithm based on the node split technique. The initiation and the subsequent propagation of the crack depend on the two failure criteria used in the previous chapter. The brittle failure is assumed to occur at a material point when the maximum principal stress there equals 2.34 σ_0, while the ductile failure occurs at a material point when the effective stress there drops to 90% of its maximum value and the material point is deforming plastically. During the crack propagation, the two crack surfaces may come into contact. The penalty method is used to ensure that there is no interpenetration at the contacting surfaces. A contact algorithm based on the work of Hallquist et al. [47] has been implemented in the code.

4.2 Contact Algorithm

As stated above, the slideline algorithm developed by Hallquist et al. [47] has been implemented in the code to ensure noninterpenetration of the nodes on the contact surface. In this method, one of the contacting surfaces is defined as the master surface and the other is called the slave surface. After each time increment, nodes on these surfaces are checked for interpenetration into the other surface. Normal forces proportional to the depth of penetration are applied to the nodes on the slave surface that have penetrated into the master surface, and equal and opposite forces are applied at the corresponding points on the master surface. Calculations are repeated by exchanging the roles of the master and slave surfaces. The entire process is iterated till the depth of penetration on the contact surfaces is within the prescribed tolerance. The solution is then marched forward in time.

4.3 Simulation of Crack Initiation and Propagation in an Axially Loaded Pre-Notched Plate

A schematic sketch of the problem studied is shown in Fig. 4.1. The thermomechanical deformations of the body are governed by equations (2.1)-(2.18) of the previous chapter. The body is taken to be initially stress free, at a uniform temperature of 25 ^{0}C and the initial porosity is zero. The upper and lower surfaces of the rectangular specimen are pulled axially in opposite directions at a speed of v_0; the tangential tractions and the normal component of the heat flux on the these surfaces are taken to be zero. All remaining boundary surfaces including the faces of the notch are taken to be traction free and thermally insulated. The radius of the circular notch-tip equals 0.15mm. A plane strain state of deformations is assumed to prevail in the plate. Because of geometric symmetry of the specimen and the boundary and the initial conditions about the vertical centroidal axis, deformations of the left half of the specimen are analyzed. The finite element discretization of the prenotched plate is shown in Fig. 4.2.

A crack is assumed to initiate at a point when either the maximum principal tensile stress there equals 2.34 σ_0 or the effective stress there has dropped to 90% of its maximum and the material point is deforming plastically. The former criterion corresponds to the initiation of the brittle failure and the later one to the initiation of the ductile failure. The node where the failure criterion has been satisfied is split into two overlapping but disconnected nodes.

Figure 4.3 shows, at four instants of time, the deformed meshes in a small region around the crack-tip for the case of $v_0 = 10m/s$, and the thermoviscoplastic response of the material modeled by the Litonski-Batra law with values of material parameters given in equation (2.24). The crack-tip is located at the node that failed last. The maximum principal tensile stress exceeded the critical value of 2.34 σ_0 at all failed nodes. The effective plastic strain at the crack tip was minuscule and was always less than 1%. At t= 10.4, 11.6, 12.8 and 14.0μs, fringe plots of the normal stress σ_{22}, the shear stress σ_{12}, and the effective stress σ_e

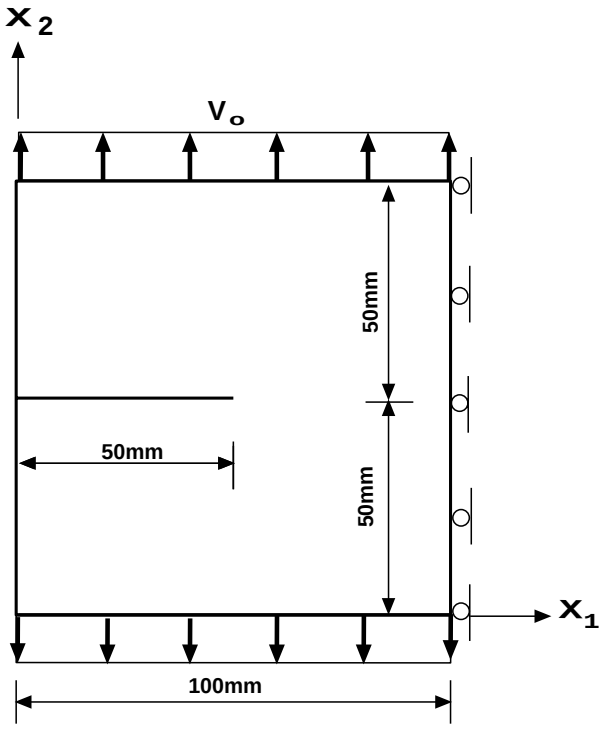

Figure 4.1: A schematic sketch of an axially loaded prenotched plate.

are exhibited in Figs. 4.4, 4.5 and 4.6 respectively. It is clear from the results plotted in Figs. 4.4 and 4.5 that the boundary condition of null tractions on the newly created crack surfaces is reasonably well satisfied. Because of the small plastic deformations at the points close to the crack tip, the temperature rise is minuscule. Figure 4.7 depicts the distance through which the crack has propagated vs. time for $v_0 = 10, 20$ and 30 m/s, and also for v_0=20m/s, σ_0 = 2100MPa. The crack speed found from these curves varies from 1005 to 2550m/s.

Needleman and Tvergaard studied a similar problem and modeled the thermoviscoplastic response of the material by a power law. They assumed that the particles with low values of yield stress were located at regular intervals on the axis of the crack. Their goal was to simulate the initiation and propagation of the ductile failure in an axially loaded prenotched plate.

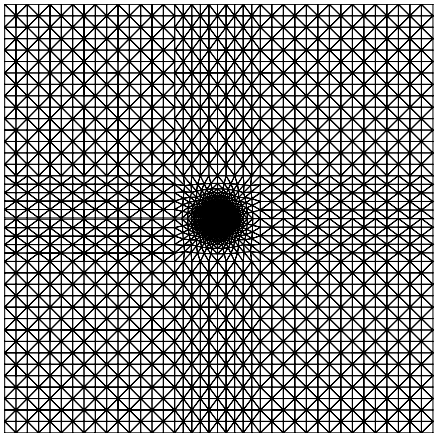

Figure 4.2: Finite element discretization of the prenotched plate.

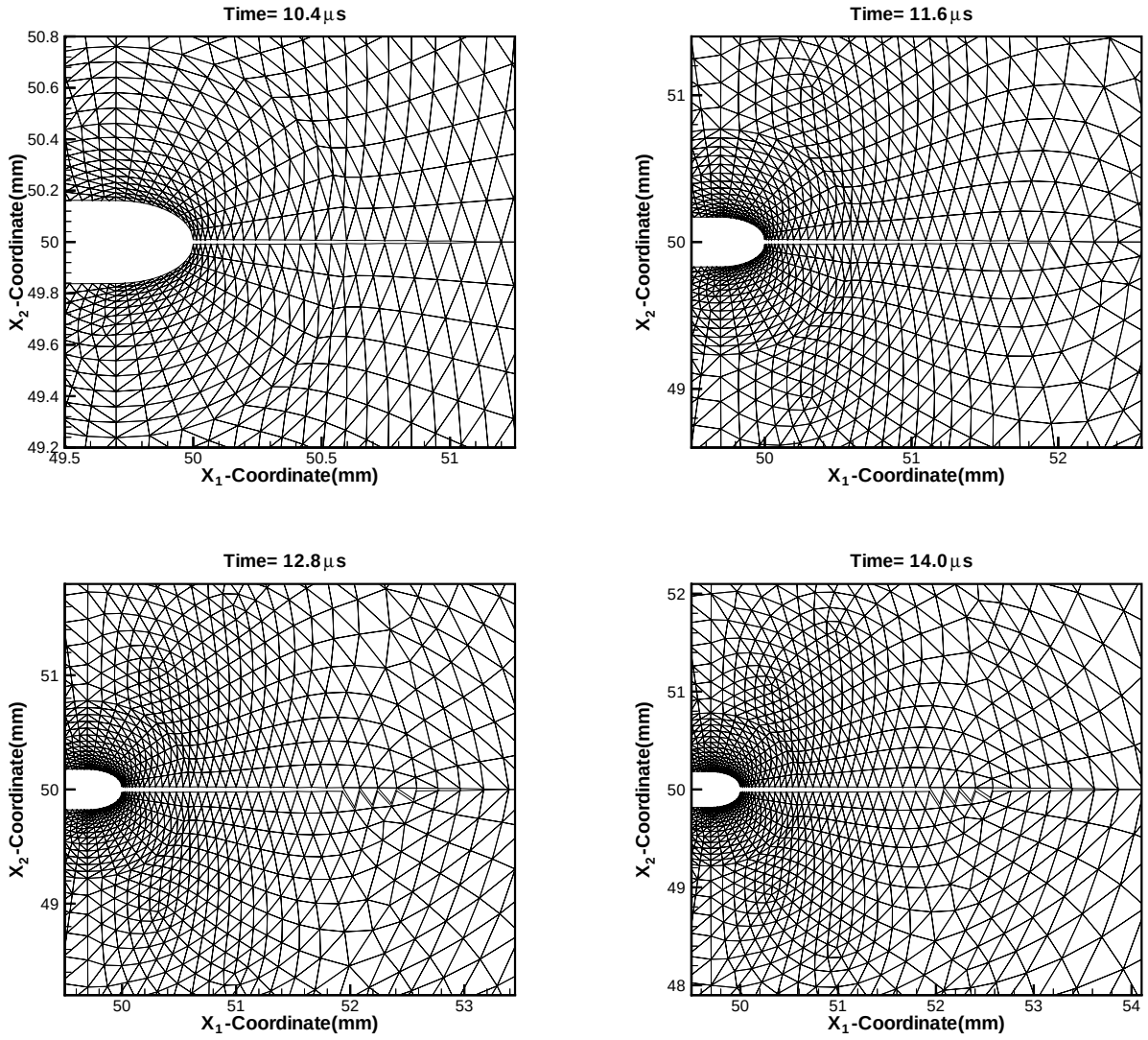

Figure 4.3: Deformed meshes at different times in a small region around the crack.

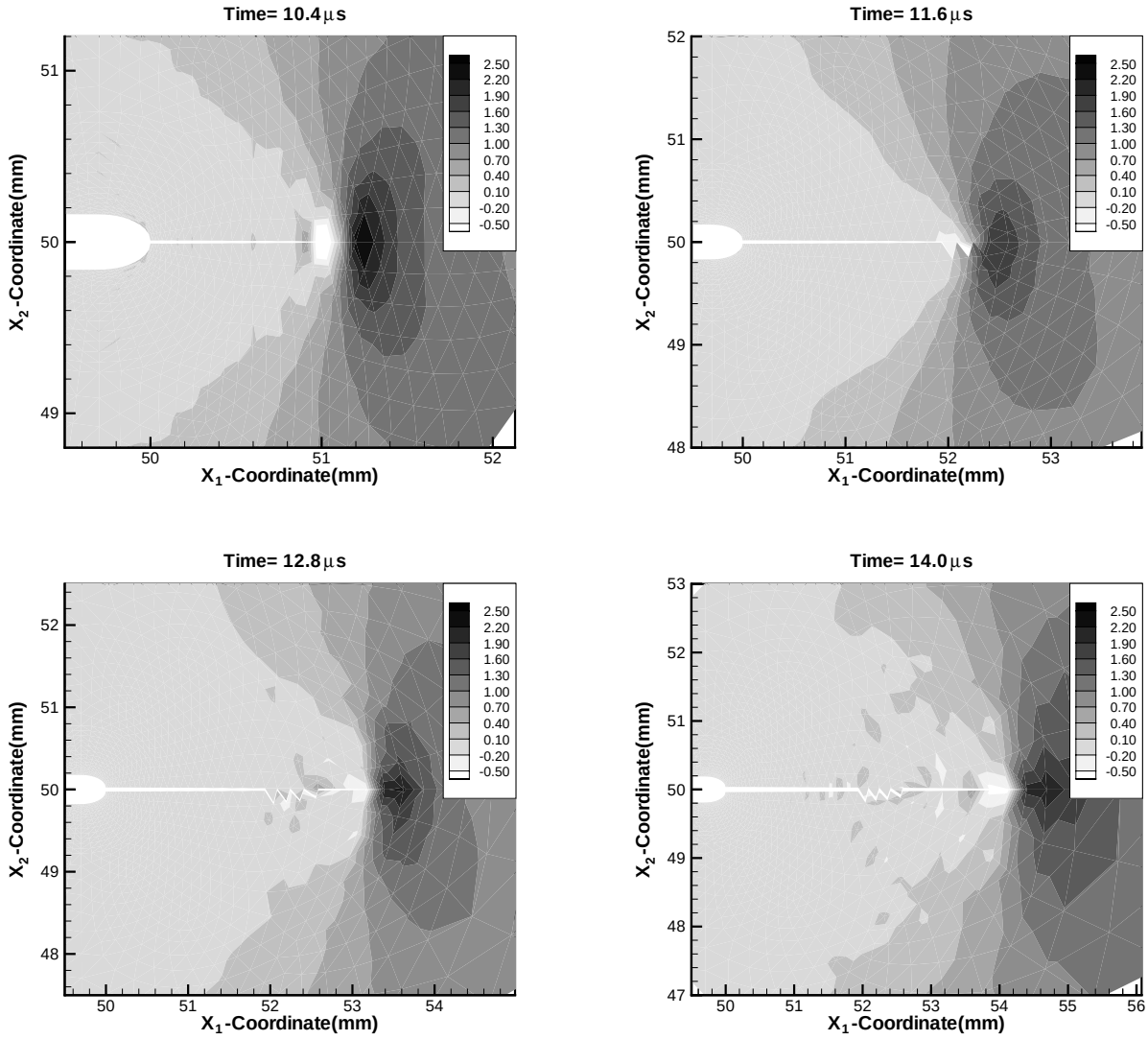

Figure 4.4: Fringe plots of σ_{22} in a small region surrounding the crack.

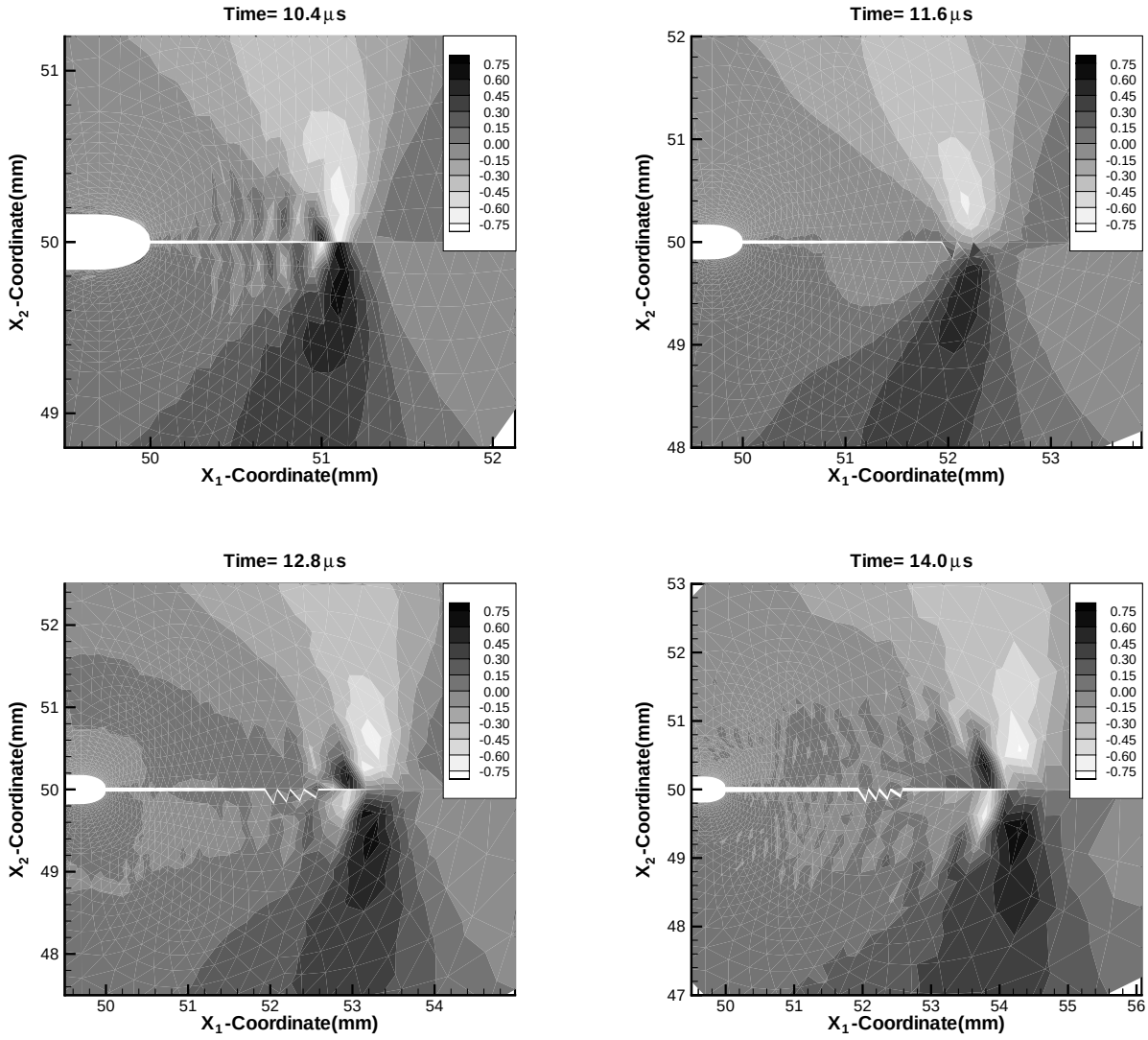

Figure 4.5: Fringe plots of σ_{12} in a small region surrounding the crack.

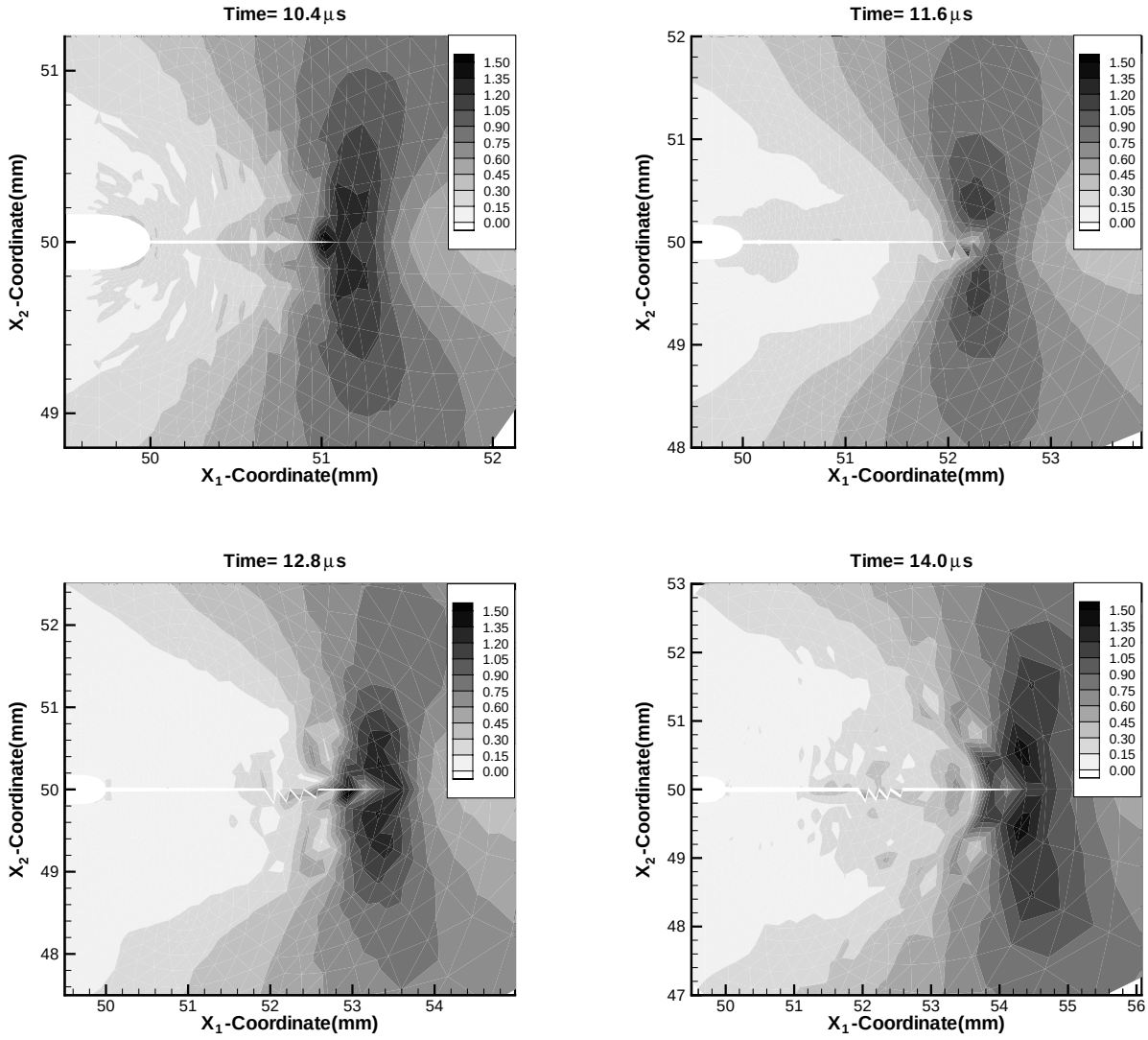

Figure 4.6: Fringe plots of the effective stress in a small region surrounding the crack.

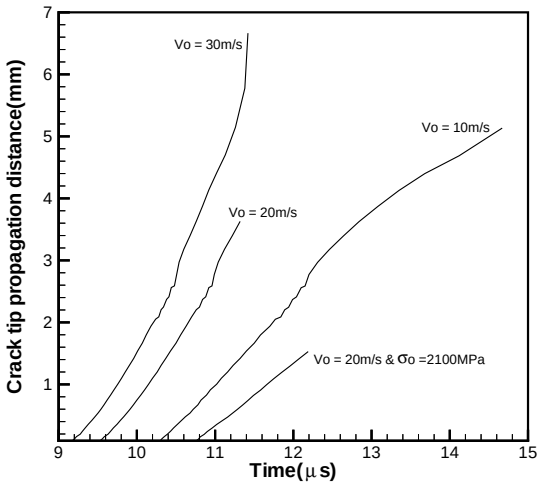

Figure 4.7: Crack propagation distance vs. time.

Chapter 5

Contributions

The contributions of this study can be summarized as follows:

1. We modified the computer code developed by Batra and Jin [20] which is used to analyze plane strain thermomechanical deformations of a viscoplastic body with the Litonski-Batra relation. The modifications include the incorporation of the Bodner-Partom relation, the Johnson-Cook relation and the power law.

2. Batra and Jin [20] multiplied equations (2.1), (2.5), (2.10) and (2.12) by a test function, integrated the resulting equations over the domain of study and obtained ODEs for nodal values of the mass density, porosity and four components of the stress tensor. Instead, here, we integrated the aforementioned equations directly at the centroids of the elements, thereby reducing the total number of unknowns.

3. Earlier numerical studies of Kalthoff's problem by various researches typically used a single constitutive relation. In our study, four constitutive relations were investigated after they had been calibrated with the same test data. Moreover, none of the earlier studies computed the impact speed at which failure mode transition occurs; in this study, the impact speed at which failure mode transition occurs was calculated for all four flow rules.

4. Unlike earlier studies of Kalthoff's problem, we also investigated the effect of the notch-tip shape, the effect of a hole in front of the notch-tip, and the effect of the specimen height on the failure mode behavior.

5. We developed an algorithm based on the node split technique to simulate the crack initiation and propagation in Mode I simulations. The initiation and subsequent propagation of the crack depend on the brittle and ductile failure criteria.

Chapter 6

Conclusions

We have used four thermoviscoplastic relations to analyze the thermomechanical deformations of a pre-notched plate impacted on the side by a cylindrical projectile. The action of the projectile on the plate is simulated by prescribing on the contact surface null tangential tractions and the time history of the normal component of the velocity. The thermoviscoplastic relations are calibrated to give the same stress-strain curve during homogeneous simple shearing deformations of a block deformed at a nominal strain-rate of 3300/s. The deformations of the pre-notched plate are nonhomogeneous and the time-dependent effective plastic strain rates at points near the notch tip attain values in the range of $10^4/s$. Results computed near the notch tip with the four thermoviscoplastic relations agree qualitatively but the magnitudes of the maximum effective plastic strain, the maximum principal tensile stress, the times when the effective stress at a point has dropped to 90% of its peak value there, and the time of initiation of the brittle failure as signified by the maximum principal tensile stress attaining a prespecified critical value are different. In a pre-notched plate made of a mild steel with a notch tip radius of 0.15mm, the impact speed at which the failure mode transitions from brittle to ductile is found to be 13.5, 18.5, 19.3 and 22.9 m/s, respectively, for the Litonski-Batra, the power law, the Bodner-Partom and the Johnson-Cook relations. We should add that these values depend upon the criteria assumed for the initiation of the

brittle and the ductile failure modes. For the Bodner-Partom relations, the transition speed is given by 1179 $r_0^{0.465}$ m/s when r_0 is in meters. From his test data on plates made of a high strength steel, Kalthoff found the transition speed to be $1350\sqrt{r_0}\ m/s$ which equals 16.53 m/s for $r_0 = 0.15$mm. For a fixed value of the impact speed, the time of initiation of a shear band decreases with an increase in the value of the quasistatic yield stress of the material, and a decrease in the radius of the notch tip.

We have numerically studied transient plane strain thermomechanical deformations of a prenotched plate with the edge surface between the two notches subjected to an impact load. The impact load is simulated by prescribing null tangential tractions and a time dependent normal velocity at the impacted plate points. The material response of the plate is modeled by the Bodner-Partom relation. The effects of the shape of the notch tip and of the presence of a circular hole located ahead of the circular notch tip on the initiation of a failure mode are also scrutinized.

It is found that for very blunt and circular notch tips the failure mode transitions from the brittle to the ductile with an increase in the impact speed. However, for two very sharp elliptic notch tips, the ductile failure precedes the brittle failure for each one of the six impact speeds studied. Points on the surface of the notch tip where the ductile failure initiates move towards the axis of the notch tip with an increase in the ratio of the length of the principal axis of the elliptic notch tip that is along the axis of the notch to the one perpendicular to it. Typical values of the effective plastic strain rate are $5 \times 10^4/s$ and the temperature rise at the instant of the initiation of the shear band is 120°C.

When a circular hole of radius r_0 is located directly ahead of the circular notch tip of radius r_0, the brittle failure always preceded the ductile failure and the former initiated from a point on the lower surface of the circular hole. Except when the distance between the centers of the circular hole and the circular notch tip equals $3r_0$, the ductile failure initiated from a point on the lower surface of the circular notch tip. The circular hole is noticeably displaced in the direction of impact and is also severely deformed. The largest plastic deformations

occur in the region surrounding the line joining a point on the lower surface of the notch tip to a point on the upper surface of the circular hole.

We have also scrutinized the thermomechanical deformations of the prenotched plate when the circular hole is located either above or below the axis of the notch. The presence of the hole below the axis of the notch enhances the initial effective plastic strain rate at a point on the lower surface of the notch tip and acceleartes the initiation of the brittle failure; the brittle failure ensues from a point on the surface of the circular hole. When the center of the hole is located at a vertical distance equal to the radius of the hole either above or below the axis of the notch, both the brittle and the ductile failures originate from points adjacent to the surface of the circular hole. However, when this vertical distance equals three times the radius of the hole, the points of initiation of the brittle failures are near the surface of the hole but those of the ductile failure close to the lower surface of the notch tip.

Bibliography

[1] Affourad JL, Dormeval R, Stelly M, Ansart JP. Adiabatic shear bands in metals and alloys under dynamic compressive conditions. In : J .Harding(Ed.), Mechanical properties at high rates of strain. Conference series number 70, The institute of physics, Bristol and London 533 (1984).

[2] Aoki S, Kishimoto K, Sakata M. Finite element computation of dynamic stress intensity factor for a rapidly propagating crack using J-integral. Comput. Meth, 2, 54-62 (1987).

[3] Atluri SN and Tishionka. Numerical studies in dynamic fracture mechanics. Int. J . Fracture. 27 , 245-261 (1985).

[4] Backman ME, Finnegan SA. The propagation of adiabatic shear, Metallurgical effects at high strain rates, Plenum press, New York, 1973,pp. 531-543 (1973).

[5] Bai Y, Dodd B. Adiabatic shear localization. Pregman press (1992).

[6] Bai YL. Thermo-Plastic instability in simple shear. J. Mech. Phys. Solids Vol. 30, N0.4, pp 195-207 (1982).

[7] Batra RC. Effect of material parameters on the initiation and growth of adiabatic shear bands. Int. J. Solids and Structures. Vol 23 No. 10, pp 1435-1446 (1987).

[8] Batra RC. Steady state penetration of thermoviscoplastc targets. Comp. Mech. Vol. 3, 1-12 (1988).

[9] Batra RC. Numerical solutions of initial-boundary-value problems with shear strain localization, in Localization and Fracture Phenomenon in Inelastic solids (P. Perzyna, Ed.), pp. 301-389, Springer-Verlag, Wien, New York (1998).

[10] Batra RC, Adam A. Effect of viscoplastic flow rules on steady state penetration of thermoviscoplastic targets. Int. J. Engrg. Sci, Vol. 29, No. 11, pp. 1391-1408 (1991).

[11] Batra RC and Chen L. Effect of viscoplastic relations on the instability strain, shear band initiation strain, the strain corresponding to the minimum shear band spacing, and the band width in a thermoviscoplastic material. International Journal of Plasticity (to appear) (2000).

[12] Batra RC and Gummalla RR. Effect of material and geometric parameters on deformations near the notch tip of a dynamically loaded prenotched plate. International Journal of Fracture 101, 99-140 (2000).

[13] Batra RC and Hwang J. An adaptive nmesh refinement technique for two-dimensional shear band problems. Comp. Mech., Vol. 12, pp. 255-268 (1993).

[14] Batra RC and Kim CH. Adiabatic shear banding in elastic-viscoplastic nonpolar and dipolar materials. *Int J Plasticity* **6**, 127-141 (1990).

[15] Batra RC and Kim CH. Analysis of shear bands in twelve materials. Int. J. Plasticity. 8, 425-452 (1992).

[16] Batra RC and Kim KH. Effect of viscoplastic flow rules onthe initiation and growth of shear bands at high strain rates. Journal of the mechanics and physics of solids. *38, 859-874* (1990).

[17] Batra RC and Ko KI. An adaptive mesh refinement technique for the analysis of shear bands in plane strain compression of a thermoviscoplastic solid. Comp. Mech. 10, 369-379 (1992).

[18] Batra RC and Ko K I. Analysis of shear bands in dynamic axisymmetric compression of a thermoviscoplastic cylinder. Int. J. Engng. Sci, Vol. 31, No. 4, pp. 529-547 (1993).

[19] Batra RC and Kim KH. Effect of viscoplastic flow rules on the initiation and growth of shear bands at high strain rates. Journal of the Mechanics and Physics of Solids 38, 859-874 (1990).

[20] Batra RC and Jin XS. Analysis of dynamic shear bands in porous thermally softning viscoplastic materials. Arch. Mech. 46, 13-36 (1994).

[21] Batra RC and Jayachandran R. Effect of constitutive models on steady state axisymmetric deformations of thermoelastic-viscoplastic targets. Int. J. of Impact Engineering, Vol. 12, No. 2, pp. 209-226 (1992).

[22] Batra RC and Jaber NA. Failure mode transition speeds in an impact loaded prenotched plate with four thermoviscoplastic relations. Int. J. of fracture(to appear).

[23] Batra RC and Nechitalio NV. Analysis of failure modes in impulsively loaded prenotched steel plates. Int. J. Plasticity. 13, 291-308 (1997).

[24] Batra RC and Peng Z. Development of shear bands in dynamic plane strain compression of depleted uranium and tungsten blocks, Int. J. of Impact Eng., Vol. 16, No. 3, pp. 375-395 (1995).

[25] Batra RC and Rattazzi D. Adiabatic shear banding in a thick-walled steel tube. Comp. Mechs. 20, 412-426 (1997).

[26] Batra RC and Ravisankar MVS. Three-dimensional numerical simulation of the Kalthoff experiment. International Journal of Fracture 105, pp. 161-186 (2000).

[27] Batra RC. and Zhang X. On the propagating of a shear band in steel tube. J. Engrg. Matr, and Tech., Vol. 116, pp. 155-161 (1994).

[28] Beissel SR, Johnson GR, Popelar CH. An element-failure algorithm for dynamic crack propagation in general direction. Engeering fracture mechanics, 61, 407-425(1998).

[29] Bodner SR and Partom Y. Constitutive equations for elastic-viscoplastic strain-hardening materials. J. Appl. Mechanics. Vol. 56, pp. 527 (1975).

[30] Bourne B, Jones PN, Markham JA. Microstructural features of sock-loaded metals. In 3rd Conf.. Machanical Properties at High Rates of Strain. Institue of Physics Conference Ser. No. 70 (1984).

[31] Budiansky B. Thermal and thermoplastic properties of isotropic composites. J. Composite Materials, Vol. 4, pp. 286-295 (1970).

[32] Chaboche JL. Constitutive equations for cyclic plasticity and cyclic viscoplasticity. International Jounal of Plasticity. Vol. 5, pp 247-302 (1989).

[33] Chen L and Batra RC. Material instability criterion near a notch tip under locally adiabatic deformations of thermoviscoplastic materials. Theoretical and Applied Fracture Mechanics. Vol. 30, pp. 153-158 (1998).

[34] Chen L and Batra RC. The asymptotic structure of a shear band in mode-II deformations. International Journal of Engineering Science 37, 895-919 (1999).

[35] Chu CC and Needleman N. Void nucleation effects in biaxially streched sheets. J . Eng. Mater. Tech. 102, 249-256 (1980).

[36] Clifton RJ. Adiabatic shear. In Material response to ultrahigh loading rates (Eds. Hermann W et al.). U.S. NRC. Material Advisory Board Report NMAB-356 (1980).

[37] Culver RS. Thermal instability strain in Dynamic plastic deformation. In Metallurgical effects at High Strain Rates(Ed. R. W. Rhode, B. M. Butcher, J. R. Holland, C. H. Karnes). Plenum Press, New York (1973).

[38] Dormeval R. The adiabatic shear phenomenon. In Materails at high strain Rates(ed. Blazynski, T. Z.), Elsevier Applied Science, Barking, Essex. 47-70 (1987).

[39] Drucker DC. Proc. 1st U. S. Natl. Congress Appl. Mech., pp. 487-491, A. S. M. E., New York (1951).

[40] Duffy J and Chi YC. On the measurement of local strain and temperature during the formation of adiabatic shear bands. Material Science and Engineering. Vol. A157. PP. 195-210 (1992).

[41] Eleiche MA and Campbell JD. Oxfrod Univ. Engrg. Lab Report No. 1106/74 (1974).

[42] Fischer JR. Void nucleation in spheroidized steels during tensile deformation. Ph.D. Thesis, Brown University (1980).

[43] Grebe HA, Pak H, Meyers MA. Adiabatic shear localization in Titanium An Ti-6 Pct Al-4 Pct V Alloy. M.A. Metal Trans., 16A, 761-775 (1985).

[44] Giovanola JH. Adiabatic shear banding under pure shear loading. Part1: Direct observation of strain localization and energy dissipation measurement. Mechanics of Materials. Vol. 7, pp. 59-71 (1988).

[45] Giovanola JH. Adiabatic shear banding under pure shear loading. Part II: Fragtographic and metallorgraphic observations. Mechanics of Materials. Vol. 7, pp. 73-87 (1988).

[46] Gurson AL. Continuum theory of ductile rupture by void nucleation and growth. Part 1 Yield criteria and flow rules for porous ductile media. J. Eng. Mater. technol., 99, 2-15 (1977).

[47] Hallquist GL, Goudreau GL and Benson DJ. Sliding interfaces with contact-impact in large-scale lagrangian computations. Computer methods in applied mechanics and engineering 51, pp. 107-137 (1985).

[48] Hartley KA, Duffy J and Hawley RH. Measurement of the temperature profile during shear band formation in steels deforming at high strain rates. J. Mech. Phys. ssolids, Vol. 35, pp. 283-301 (1987).

[49] Harding J. J. Arch. Mech. Vol. 27, PP. 715 (1975).

[50] Hendrickson JA, Wood DS and Clark DC. The initiation of brittle fracture in mild steel. Transactions of the American Society for Metals, 50, 656-681 (1958).

[51] Hockett JE. Trans. AIME, Metall. Soc. 239, pp. 969-976 (1967).

[52] Johnson GR and Cook WH. A constitutive model and data for metals subjected to large strains, high strain rates and high temperatures. Proc. 7th Int. Symp. Ballistics, The Hague, The Netherlands, 541-548 (1983).

[53] Johnson W. Henri Tresca as the originator of adiabatic heat lines. Int. J Mech. Csi, Vol. 29 (5). pp. 301 (1987).

[54] Kalthoff JF. Shadow optical analysis of dynamic shear fracture. SPIE, Vol. 1814, Photomechanics and Speckle Meteorology, 531-548 (1987).

[55] Kalthoff JF and Winkler S. Failure mode transition at high rates of shear loading. Proc. Int. Conf on Impact Loading and Dynamic Behavior of Materials, eds. C.Y. Cheim et al., 185-195, Informationsgesellaschaft Verlag Bremen (1987).

[56] Kalthoff JF. Modes of dynamic shear failure in solids. International Journal of Fracture 101, 1-31 (2000).

[57] Kalthoff JF. On the measurement of dynamic fracture toughness- a review of recent work. International Journal of Fracture 27, 277-298 (1985).

[58] Klopp RW, Clifton RJ and Shawki TG. Pressure-shear impact and the dynamic viscoplastic response of metals. Mecahincs of Materials, Vol/ 4, pp. 375-385 (1985).

[59] Kobayashi H and Dodd B. A numerical analysis if the formation of adiabatic shear bands including void nucleation and growth, Int. J. Impact Engng. Vol. 8, pp. 1-13 (1989).

[60] Kobayashi AS, Emery AF and Mall S. Dynamic finite element and dynamic photoelastic analysis of two fracturing Homilite-100 plates. Experimental Mech., **16**, 321-328 (1976).

[61] Koh HM, Lee HS and Harber RB. Dynamic crack propagation analysis using Eulerian-Langrangian kinematic descriptions.Comput. Meth 3, 141-155 (1988).

[62] Knott JF and Cortell AH. Notch brittleness in mild steel. Journal of the Iron and Steel Institute. V. 201, pp. 249-260 (1963).

[63] Lee YJ and Freund LB. Fracture initiation due to asymmetric impact loading of an edge cracked plate. J. appl. Mech. 57, 104-111 (1990).

[64] Leech PW. Met. Trans., 16A, 1900-1903 (1985).

[65] LeRoy GH. Large scale plastic deformation and fracture for multiaxial stress states. Ph.D. thesis, McMaster University (1978).

[66] Liao S and Duffy J. Adiabatic shear bands in a TI-6Al-4V titanium alloy. J. Mech. Phys. Solids, Vol. 46, No. 11, pp. 2201-2231 (1998).

[67] Lindholm US and Johnson GR. Strain-rate effects in metal at large shear strains. In Mechanical behavior at high strain rates. Proceedings of the Conference on Mechanical Properties of Materials at High Strain Rates. Institute of Physics. London (1982).

[68] Litonski J. Plastic flow of a tube under adiabatic torsion. Bulletin de L'Academie Polonaise Des Sciences, serie des Sciences Techniques XXv,(1), 7 (1977).

[69] Marchand A and Duffy J. An experimental study of the formation process of adiabatic shear bands in structural steel. J . Mechs. Phys. Solids. 36. 251-283 (1988).

[70] Mason JJ, Rosakis AJ and Ravicahndren G. Full field measurements of the dynamic deformation field around a growing adiabatic shea band tip of a dynamically loaded crack or notch. *J. Mech. phys. Solids.* **42**, 1679-1607 (1994).

[71] Mason JJ, Zimmerman JA, Roessig KM. The effect of ageing condition on shear localization from th e tip of a notch in maraging steel, J. of Materials Sceince, Vol. 33, pp. 1451-1460 (1998).

[72] Merzner AM. Modelling of adiabatic shear band development from small imperfections. J. Mech. Phys. Solids, Vol. 30, No. 5, pp. 323-338 (1982).

[73] Meyers MA, Wittman CL, Pak H and Kuriyama S. Observation and modelling of High-Strain-Rate shear localization. In Proceedings of the International Conference on impact Loading and Dynamic Behavior of Materials (Ed. by C. Y. Chem, H.D. Kunze and L.W. Meyers). PP. 719-728 (1988).

[74] Meyers MA. Dynamic Behavior of Materials. John Wiley (1994).

[75] Molinari A and Clifton RJ. Analytical characterization of shear localization in thermo-viscoplastic materials, J. Appl. Mech. Vol. 54, pp. 806-812 (1987).

[76] Needleman A. Dynamic shear bands in plane strain. J. App. Mech. 56, 1-8 (1989).

[77] Needleman A and Tvergaard V. Analysis of brittle-ductile transition under dynamic shear loading. Int. J. Solids Structures. 44, 2571-2590 (1995).

[78] Needleman A and Tvergaard V. An analysis of dynamic ductile crack growth in a double edge cracked specimen, Int. J. Fracture, Vol. 49, pp. 41-67 (1991).

[79] Needleman A and Tvergaard V. A numerical study of void distribution effects on ductile crack growth., Engr. Fracture Mech. Vol. 38, pp. 157-173 (1991).

[80] Passman SL and Batra RC. A thermomechanical theory for a porous anisotropic elastic solid with inclusions, Arch. Rat. Mech. ANal., Vol. 87, pp. 11-33 (1984).

[81] Peraire J, Vahdati M, Morgan K and Zienkiewics OC. Adaptive remeshing for compressible flow computations. J. Comp. Physics. 72 , 449-466 (1987).

[82] Perzyna P. Constitutive modeling for brittle dynamic fracture in dissipative solids. Archives of Mechanics 38, 725-738 (1986).

[83] Recht RF. Catastrophic thermoplastic shear, J. App. Mech., Vol. 31, pp. 189-193 (1964).

[84] Ritchie RO, Knott JF and Rice JR. On the relationship between critical tensile stress and fracture toughness in mild steel. Journal of the Mechanics and Physics of Solids 21, 395-410 (1973).

[85] Rogers HC and Shastry CV. Material factors in adiabatic shearing in steels. In Shock Wave and High Strain Rate Phenomena in Metals (Ed. M. A. Meyers, L. Murr). Plenum press, New York (1980).

[86] Shackelford JF. Introduction to materials science for engineers, 2nd Ed, Macmillan Publishing Co., New York (1988).

[87] Shockey DA, Seaman L and Curran DR. The influence of microstructural features on dynamic fracture. In Metallurgical Effects at High Strain Rates (Ed. R. W. Rhode, B.M. Butcher, J. R. Holland, C. H. Karnes). Plenum Press, New York (1973).

[88] Shockey DA. Materials aspects of adiabatic shear phenomenon. In Metallurgical Applications of Shock-Wave and High-strain-Rate Phenomena (Ed. L. E. Murr, K. P. Staudhammer, M. A. Meyers). Marcel Dekker Press, New York (1988).

[89] Staker MR. The relation between adiabatic shear instability strain and material properties. Acta Metllurgica , Vol. 29. pp. 683-689 (1981).

[90] Thesken JC and Gudmundson P. Applications of a moving variable singular element to dynamic fracture mechanics. 52, 47-65 (1991).

[91] Timothy SP and Hutchings IM. The structure of adiabatic shear bands in a Titanium alloy. Acte Metallurgica, Vol. 33, No. 4, pp. 667-676 (1985).

[92] Tsao MC and Campbell JD. Oxford Univ. Engrg. Lab. Report No. 1055/73 (1973).

[93] Tvergaard V. Influence of the voids on shear band instabilities under plane strain conditions. Int. J. Fracture, 17, 389-407 (1981).

[94] Tvergaard V and Needleman A. Analysis of the cup-cone fracture in a round tensile bar. Acta Metall. 32, 157-196 (1984).

[95] Tvergaard V and Needleman A. Effect of material rate sensitivity on failure modes in the Charpy V-notch test. Journal of the Mechanics and Physics of Solids 34, 213-241 (1986).

[96] Tvergaard V and Needleman A. An analysis of the brittle-ductile transition in dynamic crack growth. International Journal of Fracture 59, 53-67 (1993).

[97] Tvergaard V. Journal of the mech. phys. solids. 30 , 399-425(1982).

[98] Taylor GI and Quinney H. The latent energy remaining in a metal after cold working. Proceedings of the Royal Society of London. Series A, Vol. A134, pp. 307-326 (1934).

[99] Winter RW. Adiabatic shear of titanium and polymethylmethacrylate. Philos. mag. 31, 765-773 (1975).

[100] Winter RE. Measurement of fracture strain at high stain rates. In Mechanical Properties at High Rates of Strain, (Ed. J. Harding). Conference Series Number 47, The Institute of Physics, Bristol and London (1979).

[101] Wright TW and Batra RC. The initiation and growth of the adiabatic shear bands. Int. J. Plasticity, Vol. 1, pp. 205 (1985).

[102] Wright TW and Batra RC. Further results on the initiation and growth of the adiabatic shear bands. J. Physique, Vol. 46(C5), PP. 323 (1985).

[103] Wright TW and Batra RC. Adiabatic shear bands in simple and dipolar materials. Proc. IUTAM Symposium on Macro- and Micro-Mechanics of High Velocity Deformations and Fracture, Springer-Verlag, Berlin-Heidelberg-New York (1986).

[104] Wright TW and Walter JW. On stress collapse in adiabatic shear bands. J. Mech. Phys. Solids. 35, 701-720 (1987).

[105] Woodward RL, Baxter BJ and Scarlett NVY. Mechanics of the adiabatic shear plugging failure in high strength Aluminium and Titanium alloys. In Mechanical Properties at High Rates of Strain, (Ed. J. Harding). Conference Series Number 70, The Institute of Physics, Bristol and London (1984).

[106] Yagawa G, Sakai Y and Ando Y. Fast fracture and crack arrest. ASTM STP 627, Hahn GT and Kanninen MF(eds.). 109-122(1977)

[107] Zerilli FJ and Armstrong RW. J. Appl. Physics, 61, No. 5, 1816 (1987).

[108] Zhou M, Rosakis AJ and Ravichandran G. Dynamically propagating shear bands in prenotched plates: I-Experimental investigations of temperature signature and propagating speeds. J. Mech. Phys. Solids. 44, 981-1006 (1996).

[109] Zhou M Rosakis AJ and Ravichandran G. Dynamically propagating shear bands in prenotched plates: II- Finite element simulations. J. Mech. Phys. Solids. 44, 1007-1032 (1996).

[110] Zhou M, Rosakis AJ and Ravichandran G. On the growth of shear bands and failure mode transition in prenotched plates: a comparison of singly and doubly notched specimens. Int. J . Plasticity. 14, 435-451 (1998).

[111] Zener C and Hollomon JH. Effect of strain rate on plastic flow of steel. *J appl Phys* **14**.22-32 (1944).

[112] Zukas JA. Materials at high strain rates. (Ed. Blazynski TZ). Elsevier Applied Science, pp 219-242 (1987).

Appendix

Code Verification

The basic code used herein was developed by Batra and Jin [20]. They used it to analyze the plane strain thermomechanical deformations of a thermally softening viscoplastic square block and employed the Litonski-Batra flow rule. The code was modified to include the other three flow rules, namely a power law, the Bodner-Partom and the Johnson-Cook relations. The modifications also include changing the time integration of the evolution equations of the effective plastic strain, the porosity, the density and stresses from the node points to the centroid of the elements. In order to verify the changes made, two test problems are solved. The first is a comparison with the results obtained by Batra and Kim [17] for a one-dimensional problem, and the second is a comparison with results obtained from DYNA2D for a two-dimensional problem. Figure 6.1 shows the stress-strain curves for the four flow rules for a body deformed in simple shearing at strain rates ranging from 10^3 to 10^6 s^{-1}. The solid curves represent results from the Batra and Kim code and the dash curves from the current code. There is a good agreement between the results obtained from the two codes.

The comparison with DYNA2D code is done for simple shearing and simple compression deformations of a square block, and also for the Kalthoff problem. In DYNA2D only the Johnson-Cook model without the Gurson yield function is available. Thus the void portion of the current code was deactivated for comparing the results from the present code with those obtained from DYNA2D. The simple shearing and compression block consists of four

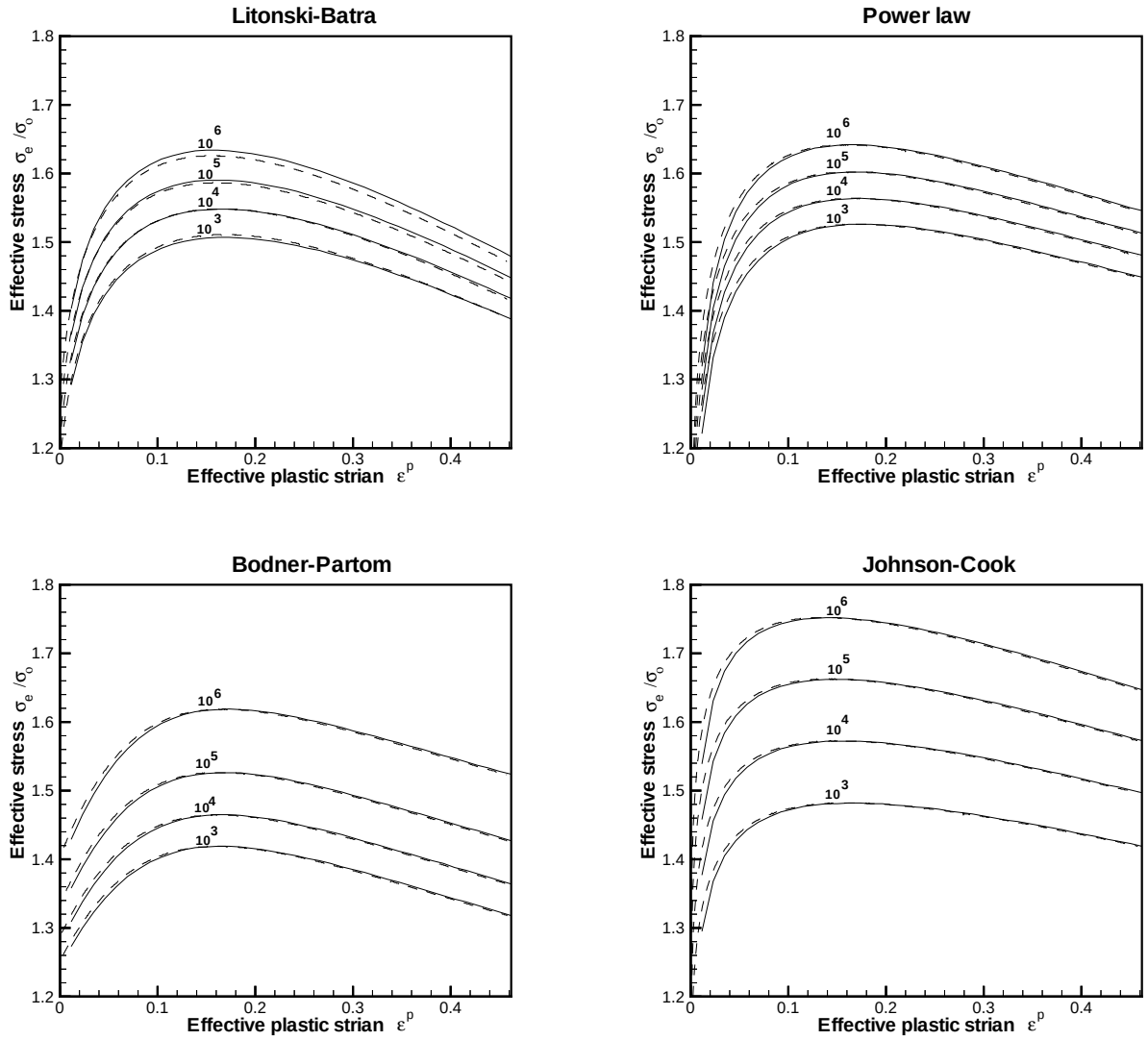

Figure 6.1: Comparison between results from the Batra-Kim code (– – –) and the present code(—).

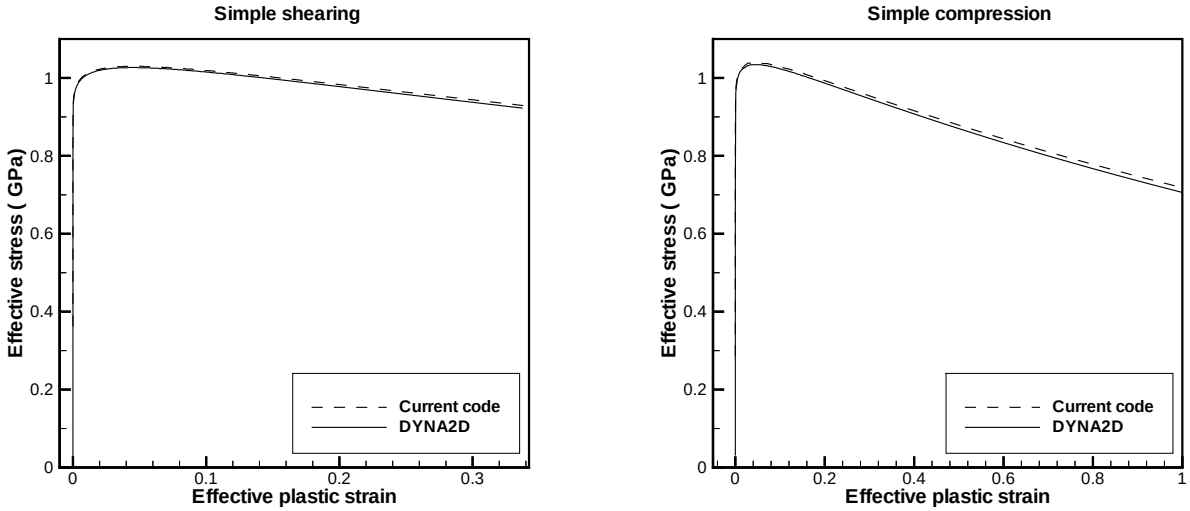

Figure 6.2: Comparison between the results from the current code and those obtained from DYNA2D in simple shearing and simple compression.

triangular elements and five nodes. The applied velocity is 33 m/s on the top two nodes and 16.5 m/s on the middle node. Fig. 6.2 shows the effective stress vs. the effective plastic strain from the current code and DYNA2D. The results from the two codes are in good agreement with each other. Fig. 6.3 shows the effective stress vs. the effective plastic strain for at a point P on the notch surface for Kalthoff problem. The line joining the centroid of the notch tip and point P makes an angle equals 45 degrees clockwise from the notch axis, a reasonable agreement is obtained between the current code and DYAN2D as can be seen from the two curves, they almost coincide with each other until a plastic strain of 0.38.

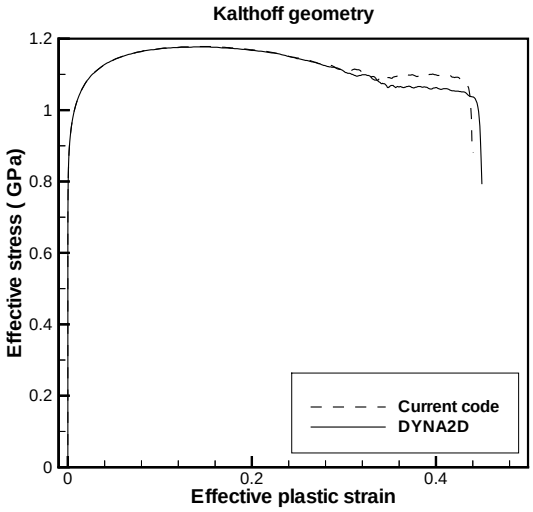

Figure 6.3: Comparison between the results from current code and those obtained from DYNA2D using Kalthoff specimen.

Vita

Naim Jaber was born on January 14, 1962 in Jenin, Palestine. He joined the Civil Engineering Department at Yarmouk University, Irbid, Jordan in August 1980 and received his Bachelor of Science degree in June 1984. Form December 1985 till August 1990 he worked in the construction industry in Saudi Arabia. In September 1990, he joined the Engineering Mechanics Department at Ohio State University and earned a Master of Science degree in March 1992. In January 1993, he enrolled in the doctoral program in the Engineering Mechanics Department at Virginia Tech and successfully defended his dissertation on December 13, 2000, to earn a Doctor of Philosophy degree in Engineering Mechanics.